DEGRADATION OF TEXTILE WASTEWATER USING ULTRA-SMALL β-FeOOH/TiO_2 HETEROJUNCTION STRUCTURE AS A VISIBLE LIGHT PHOTOCATALYST

By

MARY SOLANGE NTIRIBINYANGE

Thesis submitted in fulfilment of the requirements for the degree

Master of Engineering: Chemical Engineering

In the Faculty of Engineering
at the
CAPE PENINSULA UNIVERSITY OF TECHNOLOGY

Supervisors:
Dr Mahabubur Chowdhury &
Prof Veruscha Fester

Cape Town Campus
June 2016

DECLARATION

I, Mary Solange Ntiribinyange, declare that the contents of this thesis represent my own work, and that the thesis has not previously been submitted for academic examination towards any qualification. Furthermore, it represents my own opinions and not necessarily those of the Cape Peninsula University of Technology.

_____

(Signature)

Signed in Cape Town this Tuesday, the 1st day of June, 2016

ABSTRACT

The worldwide high demand for drinking water has led to the development of numerous advanced wastewater treatment processes. Photocatalysis has recently become an alternative and attractive technique for green energy production and environmental remediation. It is also a wastewater treatment technique which is considered reliable and is expected to provide a sustainable solution to the scarcity of clean water. In particular, heterogeneous photocatalysts based on TiO_2 nanoparticles and sunlight have been proposed as a powerful technique for degradation and mineralisation of persistent organic pollutants (POP`s). Although this method seems promising, some critical challenges are still to be addressed: namely, low photo-efficiencies, faster electron and hole (e^-/h^+) pair recombination, utilisation of UV light and catalyst removal after treatment of pollutants.

The development of this method into its application requires the combination of TiO_2 with narrower band gap semiconductors to extend the spectral response range of TiO_2. From the available theory, Akaganeite (β-FeOOH) has a lower band gap energy of 2.12 eV, with strong photo absorption of visible light and it has a tunnel structure, despite its poor photocatalytic activity. Moreover, β-FeOOH and TiO_2 have unique matching energy band potentials positions which enables the separation of e^-/h^+ pairs. The conduction band energy (E_{CB}) for β-FeOOH and TiO_2 was found to be 0.81 eV and -0.29 eV respectively and the corresponding valence band energy (E_{VB}) for β-FeOOH and TiO_2 was found to be 2.95 eV and 2.91 eV respectively. Therefore, the aforementioned photocatalysis issues were eradicated by matching energy band potentials positions of β-FeOOH and TiO_2 to form β-FeOOH/TiO_2 heterojunction structure as a visible light photocatalyst. Under simulated solar irradiation, electrons are excited from valence band of both β-FeOOH and TiO_2 to their conduction bands. The positive holes created in valence band of β-FeOOH are transferred via inter-semiconductor holes transfer mechanism to the valence band of TiO_2.The photo-generated valence band holes at TiO_2 surface react with water to produce non-selective hydroxyl radicals ($^{\bullet}OH$) which highly oxidize organic pollutants to form carbon dioxide (CO_2) and water (H_2O) as final products.

The optical and morphological characterisation of the prepared β-FeOOH/TiO_2 was performed using ultraviolet and visible (UV-Vis) spectra, X-ray diffraction (XRD), transmission electron microscope (TEM) and Fourier transform infrared (FTIR) analysis. The photocatalytic performance of β-FeOOH/TiO_2 heterojunction structure has been evaluated by decolourisation of different dyes (methyl orange, commercial dyes and real textile wastewater effluent) under simulated solar light.

The results showed that there was an interaction between β-FeOOH and TiO_2. The produced β-FeOOH/TiO_2 heterojunction structure has an overall spherical structure and showed higher photoefficiency than other photocatalysts available in the literature due to an effective separation of photo-generated e^-/h^+ pairs. A 5% β-FeOOH/TiO_2 has higher photoefficiency than 2% and 10% β-FeOOH/TiO_2 heterojunction and addition of H_2O_2 enhanced significantly the photoefficiency. The produced material showed to be effective for decolourisation of methyl orange (MO). The degradation of 99% for 80 mg/L MO was achieved within 60 minutes of irradiation using a 300 W halogen tungsten lamp and 0.01 g catalyst loading at 4.5 solution pH. The photocatalyst showed to be effective for the treatment of commercial metal-complex dye and real textile wastewater effluent. It took less than 30 minutes of irradiation time to achieve colourless from dark colours solutions. In addition, the photoefficiency of the produced β-FeOOH/TiO_2 materials is repeatable and its reusability showed no significant loss in photoactivity over four recycling stages.

ACKNOWLEDGEMENTS

- To God, the Loving and Almighty Father, the only one who knows the ins and outs of my soul. I can do all things through Christ who strengtheneth me (Phil 3:14).
- I would like to express the deepest appreciation to my supervisors:
  Prof Veruscha Fester for her education, guidance, encouragement and caring.
  Dr Mahabubur Chowdhury: he is a genius and his hard work inspired me to aim high.
- Thank you to Professor Corrine Greyling for her guidance and care. Thank you for the assistance with sampling wastewater from Falke textile industry.
- My gratitude to the South African Water Research Commission (WRC) for their financial support. Without their help, this research thesis would not have been possible.
- In addition, I would like to thank all the staff and students in flow process and rheology centre (FPRC) at Cape Peninsula University of Technology (CPUT).
- Many thanks to my close family members in person of Gideon, David, Gloriose, Grace and Clarisse for their love, support, encouragement and more especially for their smiles and tears.

DEDICATION

To my dearest and loving parents:

Ugirashebuja Faustin and Nyirangirabatware Virginie.

They selflessly love and support me.

To my dearest sister

Abubu Janviere

For being a parent, sister and friend.

To my pastor, brothers and sisters

For support, care and loving me.

Finally, in loving memory of my brother-in-law

Louis Halindintwari

For his advice and support. Because of his encouragement, I am still running the race.

.....

TABLE OF CONTENTS

Page

LIST OF FIGURES

Page

Body

LIST OF TABLES

Page

Body

Appendices

GLOSSARY: TERMS AND CONCEPTS

Advanced oxidation processes: A set of nano-technological procedures designed to minimise organic pollutants in water and wastewater by oxidation through reactions with hydroxyl radical ($^{\bullet}OH$).

Band gap energy: Refers to the difference in energy between the top valence and bottom conduction bands in insulators and semiconductors (Gupta & Triphati, 2011).

Catalyst: It is a substance that causes or accelerates a chemical reaction without itself being affected by the reaction

Conventional water treatment methods: Classical, physicochemical strategies such as filtration, flotation and activated sludge that have been used to remove pollutant materials from water and wastewater.

Heterojunction: It is an interface that occurs between two layers of different band gaps in semiconductors.

Heterogeneous photocatalysis: The acceleration of photoreaction in the presence of a semiconductor (catalyst) whilst in a different phase from the reactants (Gaya & Abdullah, 2008).

Nanotechnology for water treatment: Recent, high performance and sustainable water and wastewater treatment methods (Qu et al., 2013).

Photoreaction: It is a chemical reaction that involves or requires light.

Photocatalysis: It is the acceleration of a photoreaction in the presence of a catalyst usually a semiconductor (Fujishima et al., 2008).

Photocatalytic activity: It is used to explain the absolute photocatalytic reaction rate which shows the photocatalyst performance.

Photonic efficiency: The of formation of reaction products divided by the incident photon flow

LIST OF ABBREVIATIONS

AAS	Atomic absorption spectroscopy
AOP`s	Advanced oxidation processes
AO7	Acid orange 7
AR 27	Acid red 27
BZ	Benzamide
CB	Conduction band
CHSP	Continuous hydrothermal synthesis Plant
COU	Coumarin
CR	Congo red
E_{CB}	The energy of the conduction band
EE2	Ethynylestradiol
ER	Eosin red
E_{VB}	The energy of the valance band
FB	Forbidden band
FTIR	Fourier Transform Infrared
h^+	Photogenerated valence band hole
LSPR	Localised surface plasmon resonance
MO	Methyl orange
PL	Photoluminescence
PMMA	Methyl Methacrylate
POP`s	Persistent organic pollutants
PPFD	The photosynthetic photon flux density
RB 49	Reactive Blue 49
RhB	Rhodamine B
RR 24	Reactive Red 24
RY 160	Reactive Yellow 160
SAED	Selected area electron diffraction
SY2G	Synoset grey
SY2R	Synoset red
SY2Y	Synoset yellow
TEM	Transmission electron microscope
TOC	The total oxygen demand
VB	Valance band
UV	Ultra violet
UV-Vis	Ultraviolet and Visible Spectroscopy
XRD	X-ray diffraction

LIST OF SYMBOLS

Symbol	Description	Unit
$[A]_0$	Initial dye concentration	mg/L
$[A]_t$	Residual dye concentration	mg/L
C	Concentration	Mg/L
e^-/h^+	Electron and hole pair	eV
E^e	Energy of free electron	eV
E_g	The band gape energy	eV
E_{VB}	Energy of the valence band	eV
i	Intensity of light	Wm^{-2}
K	First order reaction rate constant	min^{-1}
X	Electronegativity of the semiconductor	-
PPFD	The photosynthetic photon flux density	$\mu mol\ S^{-1}\ m^{-2}$
λ	wavelength	nm
μ	Photoefficiency	%

CHAPTER 1. INTRODUCTION

1.1 Introduction

Heterogeneous photocatalysis has been used extensively in energy production and environmental remediation since the discovery of enhanced photo-induced decomposition of water on TiO_2 electrodes by Honda and Fujishima in 1972 (Singh *et al.*, 2013). Fresno and co-workers reported that more than 190 different semiconductors have been investigated already as suitable photocatalysts (Fresno *et al.*, 2014). However, heterojunction materials formed from combinations and morphological modifications of different photocatalysts have not yet been widely considered.

Among semiconductor materials, TiO_2 has been used extensively as an ideal photocatalyst due to its availability, chemical stability, inertness and higher photoefficiency (Y. Zhang *et al.*, 2014). However, TiO_2 has a high energy band gap of 3.2 eV for the anatase phase and 3.0 eV for the rutile phase. This makes it photoactive only under UV irradiation, limiting its practical applications under available solar light (Wang *et al.*, 2014). It has been found that the charge separation of electron and holes is a driving force of photocatalysis (Schneider *et al.*, 2014). However, faster electron and hole pair recombination decreases the photonic efficiency (ζ) to a relatively low ζ-value of less than 10% (Schneider *et al.*, 2014). This low efficiency also affects photocatalytic efficiency.

Over the past few decades, much research has been conducted to shift and increase TiO_2 photo response under visible light irradiation (Lee & Park, 2013). Various approaches such as dye anchoring, anion and cation doping and formation of heterojunction structures are being used to optimise the photonic efficiency in order to synthesise a visible light photocatalyst with the most enhanced photocatalytic performance.

It has been reported by Rawal and co-authors that formation of heterojunction structure with a narrow band gap semiconductor is a viable method among different approaches (Rawal *et al*., 2013). This technique is used to extend the spectral response range of TiO_2 and also to decrease electron and hole pairs recombination rate (Rawal *et al*., 2013). Within lower band gap semiconductors, iron oxides have garnered greater interest than other semiconductors due to their availability, low cost and adsorption capacities (Faria *et al.*, 2014).
In addition, iron oxides have higher chemical stability and lower band gap energy which allows them sufficient visible light utilisation (X. Zhang *et al.*, 2014; Rawal *et al.*, 2009).

Among iron oxides studied, FeOOH/TiO_2 heterojunction with FeOOH (energy band gap = 2,6 eV) was found to have enhanced photocatalytic performance in the degradation of 2-propanol in the gas phase under visible light irradiation (Rawal *et al.*, 2009). In addition, according to available research, Akaganeite (β-FeOOH) has a lower band gap energy of 2.12 eV, which makes it a promising photocatalyst to be combined with TiO_2 to form a heterojunction. Moreover, β-FeOOH has a tunnel structure which allows the electrons to move freely from the valence to conduction bands (Chowdhury *et al.*, 2015; Zhang *et al.*, 2015). However, there are few reports available on the photocatalytic performance of β-FeOOH/TiO_2 heterojunction in heterogeneous systems. With these special properties of β-FeOOH, the heterojunction structure of β-FeOOH/TiO_2 has a unique relative band gap energy position, which promotes efficient separation of electron and hole, leading to enhanced photocatalytic activity under simulated solar light.

Thus, this study focuses on the evaluation of photocatalytic activity of β-FeOOH/TiO_2 in the degradation of methyl orange dye from its solution under visible light irradiation. The photocatalytic performance of β-FeOOH/TiO_2 is further evaluated in decolouring wastewater effluent from Falke textile industry to highlight its potential application in a typical industry setup. Moreover, the photoactivity of a recycled photocatalyst was evaluated and presented in this study in order to assess its reusability.

1.2 Research problem

Heterogeneous photocatalysis is a recently-developed and promising technique for wastewater treatment. However, available photocatalyst materials exhibited low photonic efficiency due to faster electron and hole pairs recombination rate. The low photocatalytic performance limits the industrial applications of photocatalysis in heterogeneous systems.

1.3 Research questions

The present study seeks to answer the following questions:

(i) What is the effect of having β-FeOOH in a heterojunction structure with TiO_2 on photocatalytic activity?
(ii) What is the effect of different process parameters such as β-FeOOH toTiO_2 ratio, amount of H_2O_2 added, solution pH, and absorbed light intensity on the photocatalyst's performance?

1.4 Objectives

The objectives of this study are:

(i) To prepare a visible light photocatalyst material from β-FeOOH/TiO_2 nanoparticles and conduct the powder tests required.

(ii) To evaluate the photocatalytic performance of prepared photocatalyst in the degradation of methyl orange (as a model dye) and real textile wastewater dyes.

(iii) To optimise the experimental conditions such as initial dye concentration, catalyst loading, solution pH, H_2O_2 concentration and light intensity for maximum photoefficiency.

(iv) To assess the reusability of used photocatalyst material by recycling it over minimal recycling stages.

1.5 Significance

The study provides an effective visible light photocatalyst and set out optimum operating parameters to achieve a rapid and total degradation of organic pollutants.

1.6 Delineation

The study does not include the following aspects:

- Determination of reaction intermediates during photocatalytic degradation of organic dyes
- Immobilisation of catalyst on support
- Scale up of the photocatalytic reactor to a larger volume.

1.7 Organisation of dissertation

The work in this study was subdivided into five different chapters:

Chapter 1: Introduction: This chapter presents an introduction of this study, the research problem and various research questions, aims and objectives, the significance of the research and its delineation. Finally, the structure of dissertation is presented.

Chapter 2: Literature review: This chapter focuses on the relevant detailed theoretical background of photocatalysts. Heterojunction structures, different types of photocatalysts and different types of photocatalysts as reported in the literature.

Chapter 3: Experimental methodology: This chapter presents all details of the laboratory work on the experimental setup, experimental conditions, and the materials, including chemicals and equipment used. It also gives the experimental method used, data collection and data analysis method used throughout the study.

Chapter 4: Data analysis and experimental results: This chapter covers all structure characterisation and photoactivity evaluation results of the β-FeOOH/TiO_2 photocatalyst. It describes the analysis of relevant data, and then provides detailed discussion of the results from data interpretation.

Chapter 5: Conclusion and recommendation: This is the last chapter of the thesis. It gives a summary and draws conclusions from the results of the entire research project. Thereafter, it provides recommendations for further studies in the field of photocatalysis.

References: It is a part of this thesis which presents in details all the resources used in this dissertation.

Appendices: It is part of this thesis which presents raw experimental data, formulas and calculations used to analyse and discuss the results obtained in order to take conclusion.

CHAPTER 2. LITERATURE REVIEW AND THEORY

2.1 Introduction

An overview is presented on the literature concerning the degradation of organic pollutants under visible light irradiation. A brief description is presented on the pollutants found in textile wastewater and their conventional treatment processes. Based on the available actual publications and studies, photocatalysis is discussed in depth and the TiO_2 semiconductor is explored particularly. A review is presented in this chapter on the modification of TiO_2 to develop a visible light photocatalyst. Furthermore, this chapter discusses the application of β-FeOOH and the development of the β-FeOOH/TiO_2 heterojunction structure. Moreover, this chapter presents the photocatalysis mechanism and the fundamental operating parameters which require optimisation to achieve enhanced photocatalytic performance.

2.2 Background on textile wastewater treatment techniques

2.2.1 Textile wastewater and conventional treatment processes

Dyes and pigments are commonly used in the textile, printing, tanning, leather, food, pharmaceutical and paper industries to add desired colour to their products. It was reported by Ellouze and co-authors that the textile industry is the number one polluter of clean water and one of the most chemically intensive industries in the world (Ellouze *et al.*, 2012). It is well known that the textile industry uses large quantities of various dyes and generates the most organic colourants in water pollution.

However, it was reported by Chatzisymeon *et al.* (2013) and Asghar *et al.* (2014) that approx. 15% of 7×10^7 tons of dyestuff produced annually are lost in wastewater effluent during the dyeing process. Consequently, textile wastewater effluents are discharged with organic dyestuffs (azo and synthetic dyes), hydrophobic finishing agents (fluorocarbons and silicones) and flame retardants (halogenated or phosphonated compounds), which are a major source of environmental pollution.

Furthermore, these compounds are highly toxic, carcinogenic and recalcitrant. The presence of dyes in water also prevents sunlight to reach water bodies causing damage to aquatic life. Moreover, it is well known that colour is an obvious indicator of polluted water (Asghar *et al.*, 2014; Ghoreishian *et al.*, 2014).

Conventional wastewater treatment techniques such as physicochemical and biological processes are used during wastewater treatment, despite their ineffectiveness in the removal of persistent organic pollutants (POP`s) from wastewater using these processes. These wastewater treatment technologies include among others activated sludge, coagulation, filtration, degasification, equalisation, ion exchange, flocculation, aeration, distillation and desalination, activated carbon, flotation and skimming (Prieto *et al.*, 2005). However, POP`s such as dyes are resistant to these applied methods because of their complex aromatic structure and stability (Mahadik *et al.*, 2014). Daneshvar *et al.* (2005) and Saien *et al.* (2009) reported that the use of these methods results in low performance.

They have also reported that conventional wastewater treatment techniques are ineffective because of their high operating costs. They transfer the pollutant from one phase to another without achieving complete mineralisation (Daneshvar *et al.*, 2005; Lee & Park, 2013 and Saien *et al.*,2009). In addition, post treatment of slurry is an indispensable phase, which involves a lot of work in terms of labour and the addition of toxic chemicals. These additional works requires extra-costs which make the process inappropriate for purposes of producing clean water. Moreover, the application of higher temperature for thermal destruction of chemicals is possible, but not feasible from both a practical and economic point of view. Therefore, alternative wastewater treatment techniques (i.e. advanced oxidation processes) are required (Miljana *et al.*, 2014; Saien *et al.*, 2009).

2.2.2 Wastewater treatment using advanced oxidation processes

Since the discovery of photocatalytic splitting of water molecules using TiO_2, by Honda and Fujishima in 1872, the degradation of organic compounds by advanced oxidation processes (AOP's) has become an attractive approach to water treatment to minimise organic pollutants in wastewater (Mahadik *et al.*, 2014).

There are many types of AOP's, such as ozonation, O_3/H_2O_2 and UV/O_3, UV/H_2O_2, Fenton, UV/Fenton, photocatalysis, electrochemical oxidation, wet air and wet H_2O_2 oxidation, electron beam and catalytic ozonation processes (Elena Adina *et al.*, 2013; Li, 2013). These methods have a common and central property in that they generate hydroxyl ($^{\bullet}OH$) radicals. These $^{\bullet}OH$ radicals are highly reactive and powerful oxidising species of organic pollutants. They oxidise organic compounds into CO_2, H_2O as final products (Ribeiro *et al.*, 2015; Asghar *et al.*, 2014; Sharma *et al.*, 2011).

According to a recent review written by Lazar and co-authors on photocatalytic water treatment, homogeneous photo-Fenton is an efficient AOP technique for the destruction of organic pollutants. However, the process requires the use of large amount of ferrous sulphate ($FeSO_4$) and hydrogen peroxide (H_2O_2), which makes the technique costly (Lazar *et al.* 2012).

Therefore, heterogeneous photocatalysis with a TiO_2 semiconductor as a catalyst is gaining interest among other AOP`s techniques. According to the literature, photocatalysis is an alternative and a promising technique. This technique uses light to induce chemical transformations leading in turn to complete mineralisation of wastewater with high efficiency and cheap operational costs (Wang & Zhou, 2011; Chatzisymeon *et al.*, 2013). Therefore, this technique can be used for environmental remediation purposes.

However, the efficiency of this technique is highly dependent on the ability of the catalyst to generate $^{\bullet}OH$ radicals. These $^{\bullet}OH$ radicals are generated from a catalyst with an effective separation of photo-generated charge carriers. Therefore, the development of highly efficient visible light photocatalysts for the degradation of organic pollutants is an inevitable trend in this photocatalysis field.

Already, a lot of research has been undertaken in this field and many investigations have been carried out on different semiconductor materials. To date, the study on photocatalyst materials is still a promising research topic.

Various researchers, such as Zhang *et al.* (2014); Chong *et al.* (2010); Zaleska (2008) and Shi *et al.* (2013) report that TiO_2 nanoparticles are the most appropriate semiconductors which can be used as photocatalysts. They report that TiO_2 has been used extensively in photocatalysts due to its highly desirable properties such as availability, low cost, non-toxicity (to the environment and humans), higher surface area, higher photocatalytic performance, stability in the presence of aqueous electrolyte solutions, super hydrophilic nature, chemical inertness, self-cleaning properties and anti-bacterial properties. In addition, TiO_2 NPs can be supported on various substrates, have an ability to achieve complete mineralisation of organic pollutants and have a strong oxidising power and high photochemical stability (Nyamukamba, 2011).

2.2.3 Drawbacks of TiO_2 heterogeneous photocatalysts

The major drawback of TiO_2 as a semiconductor is its wide band gap energy of 3.2 eV for the anatase phase. According to Wang and co-authors, the wide band gap energy of TiO_2 limits its applications under available solar light, because TiO_2 absorbs only UV light, which is only about 5% of the solar spectrum (Wang *et al.*, 2014).

Moreover, Dolat *et al.* (2015) and other researchers such as M. Zhang *et al.*, (2014) reported that the separation of photo-induced charge carriers is also a major problem which restricts the photoefficiency of the TiO_2 photocatalyst. This problem is due to rapid electron and hole (e^-/h^+) pair recombination and results in low hydroxyl radical formation. In consequence TiO_2 photocatalysts yield lower photoefficiency upon light absorption.

A number of studies have emerged in the last decade and have covered largely the optimisation of TiO_2 photocatalysts under UV light. The workers presumed that the photocatalytic performance of TiO_2 under UV or visible light depends on the physicochemical properties of TiO_2 particles. According to Fujishima *et al.* (2000) and Lazar *et al.* (2012), the photoefficiency highly depends on the TiO_2 phase, method of preparation, the particle structure, crystallinity, particle size, reactive surface area and anatase to rutile ratio (Fujishima *et al.*, 2000 and Lazar *et al.*, 2012) .

2.3 Photocatalysis

Photocatalysis is one of the advanced oxidation processes (AOPs) which are based on the degradation of organic pollutants by the generation of hydroxyl radicals ($^{\bullet}OH$). It has become a powerful alternative technique to conventional wastewater treatment methods and is gaining interest, among other advanced oxidation processes, due to its high efficiency and low operational cost (Damodar *et al.*, 2010, Chatzisymeon *et al.*, 2013).

Photocatalysis is the acceleration of a photoreaction in the presence of a catalyst. All catalysts have one general main purpose, i.e. accelerating the reaction rate. Akpan & Hameed (2009) defined photocatalysis as a photo-induced chemical reaction activated by a catalyst. Photocatalysis can be divided into two main types; homogeneous reactions, in which the photocatalyst is in the same phase as the reactants, and heterogeneous reactions, in which the acceleration of photoreaction occurs in the presence of a semiconductor (catalyst) which is in a different phase from the reactants (Gaya and Abdullah, 2008).

2.3.1 Photocatalytic semiconductors

Photocatalysts are semiconductors which can be activated by light to produce e^-/h^+ pairs. Photocatalyst materials are characterised by a special electronic structure with three electronic bands: a fully completed electronic valence band (VB), empty conduction band (CB), which is always ready to accommodate electrons and band gap energy in their forbidden band (FB) (Ahmed, *et al.*, 2011; Li, 2013). There exists a long list of semiconductors that are used as photocatalysts.

Gupta & Triphati (2011) have reported that the redox potential of the e^-/h^+ charge couple should be within the band gap domain of the catalyst. It is reported that the energy level at the bottom of the conduction band determines the reducing ability of photoelectrons and the energy level at the top of the valence band determines the oxidising ability of photo-generated holes (Carp et al., 2004).

The locations of the band edges of certain materials are illustrated in Figure 2.1. Most of the reported photocatalysts available are unsuitable because of the location of their energy band edges (Figure 2.1). In addition, Gupta & Triphati (2011) reported that within shown materials on the figure, some materials have poor characteristics, such as instability in aqueous solution, photo-corrosion, toxicity and the potential to dissolve in water. For example, some materials, such as GaAs, PbS and CdS were reported to be unstable for catalysis in aqueous media, because they readily undergo photo-corrosion and are also toxic. ZnO also has been reported to be unstable because it inactivates the catalyst over time, as it readily dissolves in water to produce $Zn(OH)_2$ on its surface (Gupta & Triphati, 2011).

Moreover, some of the materials, such as Fe_2O_3, SnO_2, and WO_3 have their conduction band edges lower than the energy level of the reversible hydrogen. Thus their photocatalysis system requires additional energy to complete the splitting of water molecules and hydrogen evolution at the cathode.

It has been reported that TiO_2 has higher photocatalytic performance in photo-degradation of organic pollutants, due to its higher conduction band and its band edge potential location, as is depicted in Figure 2.1. Moreover, Gupta and Triphati reported that TiO_2 is an ideal photocatalyst among semiconductors (Gupta & Triphati, 2011).

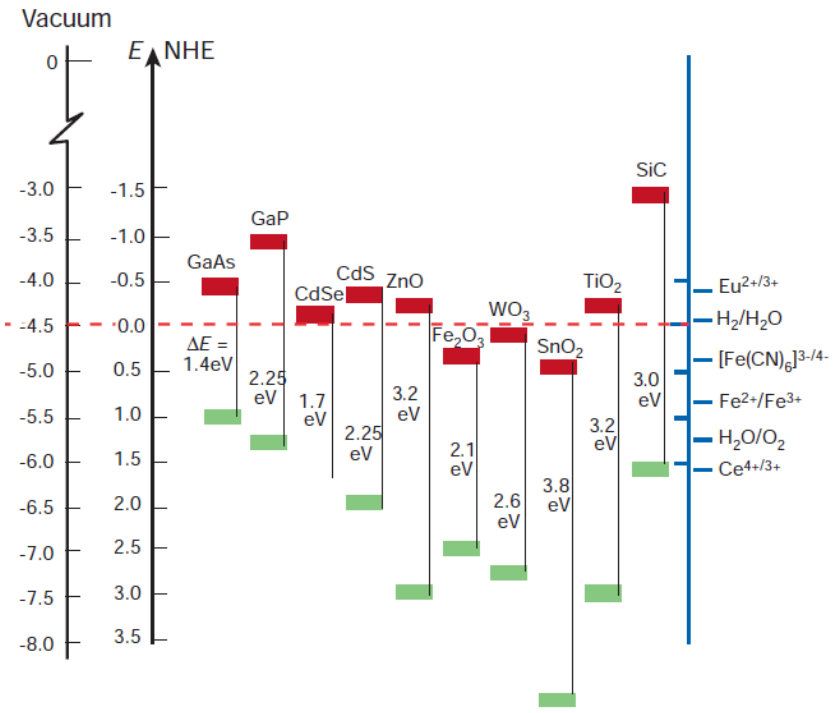

Figure 2.1 : Band positions of several semiconductors in contact with an aqueous electrolyte at pH 1 the lower edge of the conduction band (red colour) and upper edge of the valence band (green colour) are presented along the band gap in electron volts. The energy scale is indicated in electron volts using either the normal hydrogen electrode (NHE) or the vacuum level as a reference.

(Adapted from Grätzel, 2001:339)

2.4 Photocatalysis applications

Photocatalysis has been widely studied and used in many applications for environmental remediation and renewable energy as shown in Figure 2.2. Lee & Park (2013) report on the application of photocatalysis for hydrogen production, air cleaning, optical devices, anti-corrosion, hydrophilic processes, self-purification and antibacterial activity (Lee & Park, 2013; Ahmad *et al.*, 2015; Xiao *et al.*, 2015).

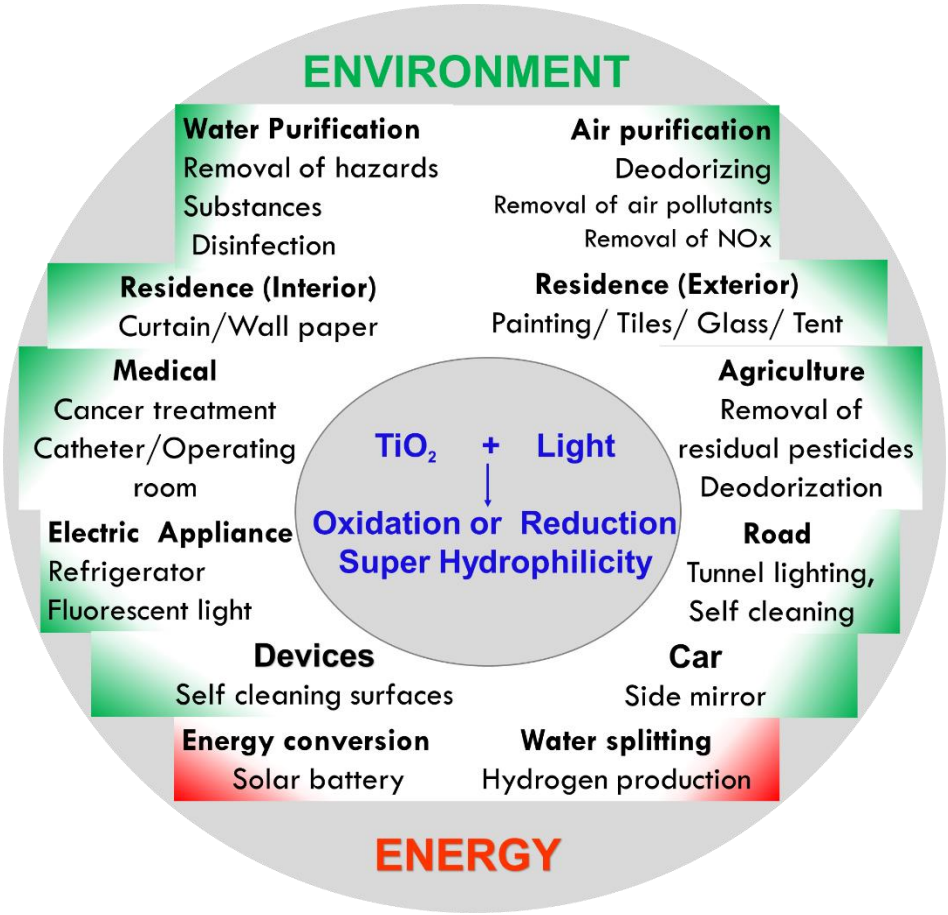

Figure 2.2 : Various applications of TiO_2 photocatalysis in environment and energy fields.

(Adapted from Lee & Park, 2013:1763)

2.5 TiO_2 surface morphology

2.5.1 TiO_2 crystal structures

TiO_2 is a polymorphous compound which appears in three different phases, namely (a) anatase, (b) rutile and (c) brookite with band gaps of 3.2, 3.02 and 2.96 eV respectively (Figure 2.4).

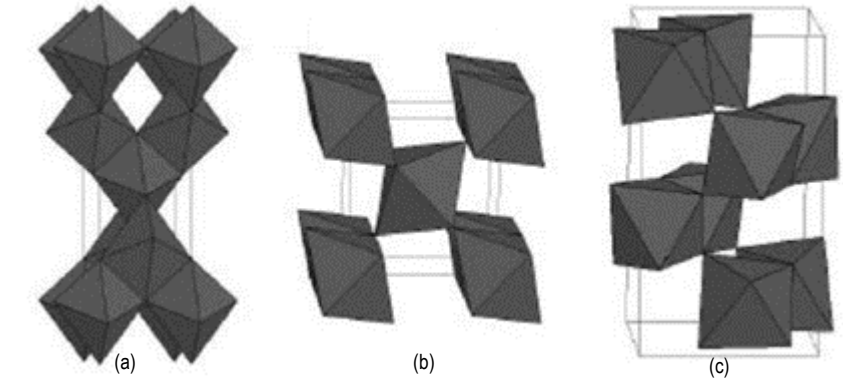

Figure 2.3 : Crystal structures of TiO_2: (a) anatase, (b) rutile and (c) brookite.

(Adapted from Schäffer, 2012:8)

Titanium belongs to the family of transitional metals and is a semiconductor characterised by a larger band gap (Gupta & Triphati, 2011). TiO_2 nanoparticles can be produced through hydrothermal synthesis. During its synthesis, anatase and brookite phases are transformed into rutile as the sintering temperature increases. The anatase phase has a tetragonal structure and is dominant on smaller particle sizes of less than 11 nm or when you have lower sintering temperatures of less than 600 °C. On the other hand, rutile is dominant at increased particle sizes of greater than 35 nm and when the sintering temperature is higher than 600 °C.

Within the three identified phases of TiO_2, anatase has a higher level of photocatalytic activity when compared to brookite and rutile in the oxidation of organic compounds and for solar cell synthesis (Bakardjieva *et al.*, 2006). It has been reported by Gupta & Triphati (2011) that the photoactivity of TiO_2 nanoparticles depends on the particle size, surface area, polymorph structure, crystallite size, porosity, band gap and surface hydroxyl density.

2.5.2 TiO_2 band edge positions

According to Gupta & Triphati (2011), the anatase structure is preferred for photocatalytic applications because of its high electron mobility, low dielectric constant, lower density, charge carrier dynamics, and higher energy band gap.

Schäffer (2012) reported that the anatase conduction band is 0.2 eV more than the conduction band of rutile. As an effect of this, the conduction of anatase favours reduction of O_2 in a wide pH range, as shown in Figure 2.4.

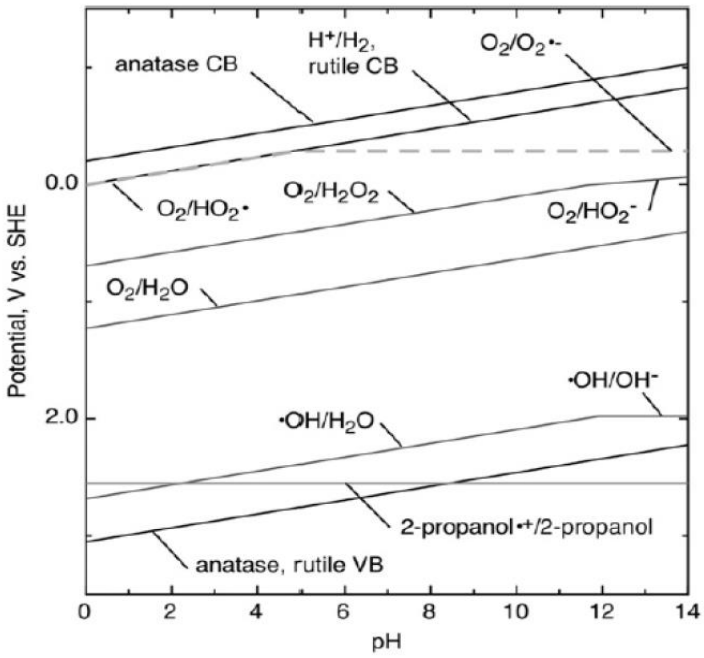

Figure 2.4 : TiO_2 energy bands and corresponding potential differences of redox reactions occurring on the TiO_2 surface as function of PH.

(Adapted from Schäffer, 2012:8)

Gupta & Triphati (2011) reported that anatase has an excellent photoreactivity due to low oxygen adsorption capacity, a higher degree of hydroxylation and a higher Fermi level. Anatase has a stronger upwards bending ability than other TiO_2 phases, inhibiting e^-/h^+ recombination, therefore holes are trapped and transferred to the surface. Nevertheless, Bakardjieva *et al.* (2006) reported that the most used TiO_2 is a commercial Degussa P-25, which is constituted of amorphous 90% (fraction by volume) anatase, rutile and brookite.

2.6 TiO_2 photocatalytic mechanism

2.6.1 Primary processes that occur on TiO_2 surface under UV light irradiation

Four primary processes are reported by Schäffer (2012) as occurring on TiO_2 surfaces upon UV light irradiation and these are charge-carrier generation, charge-carrier trapping, charge-carrier transfer and charge-carrier recombination (Schäffer, 2012). Each of these processes is discussed briefly in subsequent sections.

2.6.1.1 Charge carrier generation and excitation

When the TiO_2 semiconductor absorbs photons from light irradiation with sufficient energy greater or equal to its band gap energy, the electrons in the filled valence band (VB) will get excited and move toward the conduction band (CB) (Eq 2.1). Ohtani (2010) reported that every electron moving from VB to CB will leave a positive empty space, referred to as a photogenerated hole (h^+), in the VB (Ohtani, 2010). The continuous movement of photogenerated electrons to the CB induces electrons and holes pairs, as illustrated in Figure 2.5. The separation of charge carriers is essential for the purposes of photocatalysis.

2.6.1.2 Charge transport and trapping

According to Schäffer (2012) photon absorption must translate into surface photoactivity of the semiconducting photocatalyst. When generated charge carriers reach the surface, they should also be stabilised at the surface for electron/hole transfer processes. There is a direct relationship between the efficient charge carrier's separation and photocatalytic activity. The photocatalytic activity depends on the lifetime of photo-generated electron/hole pairs and surface redox potential.

Charge carrier trapping and transfer (Eq 2.2 - Eq 2.4) must be favoured for the complete photocatalytic reactions to take place. Unfortunately, these processes are always in competition with charge carrier recombination process. An increase of the charge carrier lifetime and interfacial charge transfer rate is very important to decrease charge carrier recombination rate so that the higher photocatalytic activity levels can be obtained (Schäffer, 2012).

2.6.1.3 Charge carrier recombination

Chong *et al.* (2010) reported that valence band electron and conduction band holes are trapped and well bounded on the surface of TiO_2 and that they do not recombine immediately after photon excitation (Eq 2.2 - Eq 2.4). However, electron and hole recombination is very likely to happen (Eq 2.5 - Eq 2.6) in nanosecond timespans, as shown by Table 2.1, in the absence of electron scavengers (Li, 2013).

Table 2.1 : Photocatalytic reaction primary processes and their characteristic times

(Adapted from Schäffer, 2012:7)

Primary process	Chemical equation	Time	Equation
Charge-carrier's generation	$TiO_2 + h\nu \rightarrow TiO_2\,(e^- + h^+)$	Faster (fs)	Eq 2.1
Charge carrier trapping	$h^+ + \mathrm{Ti^{IV}}OH \rightarrow \{\succ \mathrm{Ti^{IV}OH^{\bullet}}\}^+$ $e^- + Ti^{IV}OH \leftrightarrow \{\succ Ti^{III}OH\}$ $e^- + Ti^{IV} \rightarrow Ti^{III}$	Faster (10 ns) Shallow trap (100 ps) Deep trap (10 ns)	Eq 2.2 Eq 2.3 Eq 2.4
Charge carrier recombination	$e^- + \{\mathrm{Ti^{IV}}OH^{\bullet}\}^+ \rightarrow \succ Ti^{IV}\mathrm{OH}$ $\mathrm{h^+} + \{Ti^{III}OH\} \rightarrow Ti^{IV}OH$	Slow (100 ns) Fast (10 ns)	Eq 2.5 Eq 2.6
Interfacial charge transfer	$\{\succ \mathrm{Ti^{IV}}OH^{\bullet}\}^+ + \mathrm{Re}\,d \rightarrow \succ Ti^{IV}\mathrm{OH} + \mathrm{Red^+}$ $\mathrm{e^-} + Ox \rightarrow Ti^{IV}OH + Ox^-$	Slow (100 ns) Very slow (ms)	Eq 2.7 Eq 2.8

2.6.1.4 Interfacial charge transfer

It has been reported by Li, that redox reactions occur if there is an available suitable scavenger or surface defect state to trap the electron and hole. Thus, excited electrons and holes move to the cathode and anode respectively (Li, 2013). Schäffer (2012) reports that increases of the charge carrier lifetime (Eq 2.7) and interfacial charge transfer rate (Eq 2.8) are very important to decrease charge carrier recombination rate.

2.6.2 Photodecomposition of organic dye pollutants in heterogeneous systems

From the literature, degradation of toxic organic compounds in heterogeneous photocatalytic systems using TiO_2 nanoparticle is a well-known method (Gupta and Triphati, 2011). The organic compounds which can be targeted include: a great variety of dyes, pesticides, pharmaceuticals, herbicides, cosmetics, phenolic compounds and metal-ions.

Heterogeneous photocatalysis is also known to improve the biodegradability of cellulose effluent and is used in the treatment of many more wastewater effluents (Ahmed *et al*., 2011). To achieve complete degradation of organic compounds, Chong and co-authors report several independent steps leading to overall photocatalytic reactions which occur in the liquid phase with solid photocatalysts (Chong *et al.*, 2010).

Figure 2.5 represents the mechanism of organic pollutant degradation in a heterogeneous system.

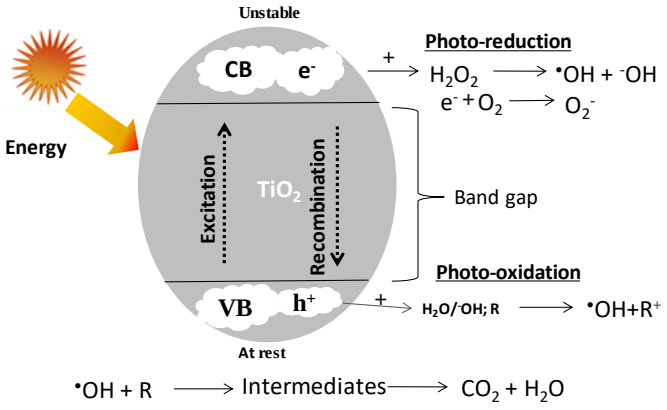

Figure 2.5 : The principles of TiO_2 photocatalysis

2.6.2.1 Dye absorption stage

Dye absorption is the initial stage during degradation of organic pollutants using heterogeneous photocatalytic systems. During this step, mass transfer of targeted organic pollutant in the liquid phase to the surface of TiO_2 photocatalyst occurs. According to Zhang and co-authors, sufficient absorption time should be allowed, in which the suspension is magnetically stirred in the dark to ensure adsorption-desorption equilibrium on the surface of the catalyst (M. Zhang *et al.*, 2014). This process results in the excitation of the molecule from the ground state to the excited states, creating electron-hole pairs. As reported by Gupta and Triphati (2011), dye absorption improves the photoefficiency by forming e^-/h^+ pairs. Also, Linsebigler and co-authors reported that the electron transfer process is favoured when organic compounds are preadsorbed on the surface of the photocatalyst (Linsebigler *et al.*, 1995).

2.6.2.2 The production of electron-holes pairs (e^-/h^+)

As shown by Eq 2.1 charge carriers (electron and holes) are generated when TiO_2 nanoparticles are irradiated with UV light.

2.6.2.3 The separation of electron and holes

The recombination of e^-/h^+ pair is most likely to happen when accompanied by heat generation, as shown by Eq 2.9.

$$e^-_{TR} + h^+_{VB}(h^+_{TR}) \rightarrow e^-_{CB} + heat \quad \text{Eq 2.9}$$

As mentioned before, poor photocatalytic activity occurs as a result of e^-/h^+ pair recombination. Therefore, the e^-/h^+ pair recombination should be prevented as much as possible, so that the valence band positive hole can go for further oxidation reactions which lead to complete oxidation of organic compounds. Akpan & Hameed (2009) reported that an electron scavenger is required to accept free electrons generated on TiO_2 surfaces to achieve an effective e^-/h^+ pair separation system. Affam and co-author suggested using hydrogen peroxide (H_2O_2) to achieve e^-/h^+ separation, because H_2O_2 acts as an electron accepter. The authors also explain in detail that H_2O_2 stops electron-hole pair recombination and enhances photoefficiency by producing more hydroxyl radicals and hydroxyl ions as shown by Eq 2.10. Furthermore, they reported that hydrogen peroxide can be converted to hydroxyl radical via Eq 2.11 increasing photocatalytic activity (Affam & Chaudhuri, 2013).

$$H_2O_2 + e^- \rightarrow {}^{\bullet}OH + OH^- \quad \text{Eq 2.10}$$

$$H_2O_2 \xrightarrow{h\nu} 2{}^{\bullet}OH \quad \text{Eq 2.11}$$

It has been reported in the literature that air can be fed into photocatalytic systems to improve e^-/h^+ pair separation. Chong and co-authors further explain that with oxygen, free electrons can be trapped and transferred to intermediate energy levels (Chong et al., 2015). As an example, in the investigation carried out by Boukhennoufa and co-authors, their results showed that electron trapping occurs at sites of defective Ti^{3+} instead of Ti^{4+} or molecular oxygen being adsorbed, allowing the formation of superoxide radicals ($O_2^{\bullet-}$), as shown in Eq 2.12 (Boukhennoufa *et al.*, 2011) . As a result, these superoxide radicals are further protonated to form hydroperoxyl radicals ($HO_2^{\bullet}$) and subsequently they become H_2O_2, as illustrated by Eq 2.12 to Eq 2.15.

$$TiO_2\ (e^-) + O_2 \rightarrow TiO_2 + O_2^{\bullet-} \quad \text{Eq 2.12}$$

$$O_2^{\bullet-} + OH^- \rightarrow HOO^{\bullet} \quad \text{Eq 2.13}$$

$$HOO^{\bullet} + e^- \rightarrow HO_2^{\bullet} \quad \text{Eq 2.14}$$

$$HO_2^{\bullet} + H^+ \rightarrow H_2O_2 \quad \text{Eq 2.15}$$

2.6.2.4 The oxidation and reduction of organic compounds

When the combination of e^-/h^+ pairs is prevented, the photo-generated valence band holes (h^+) migrate on the surface of TiO_2 and react with either water (H_2O) or hydroxyl ions (OH^-) adsorbed on the catalyst surface through Eq 2.16 and Eq 2.17. The reaction generates hydroxyl radicals ($^{\bullet}OH$) which non-selectively oxidise organic pollutants in the heterogeneous photocatalytic system (Affam & Chaudhuri, 2013).

These hydroxyl radicals oxidise directly organic molecules (OM) at the photocatalyst's surface by addition reactions to unsaturated bonds, which further form intermediate products (Eq 2.18). If the treatment time is adequate, complete mineralisation is achieved to form water and carbon dioxide as end products (Eq 2.19).

$$TiO_2\,(h^+) + H_2O \rightarrow TiO_2 + {}^{\bullet}OH + H^+ \quad \text{Eq 2.16}$$

$$TiO_2\,(h^+) + OH^- \rightarrow TiO_2 + OH^{\bullet} \quad \text{Eq 2.17}$$

$$^{\bullet}OH + MO \rightarrow Intermediates \quad \text{Eq 2.18}$$

$$^{\bullet}OH + Intermediates \rightarrow CO_2 + H_2O \quad \text{Eq 2.19}$$

Nevertheless, literature shows that the efficiency of TiO_2 heterogeneous photocatalytic systems is very low, and that enhancement of the photoactivity performance of TiO_2 under visible light is essential to its industrial application. The modification is made to extend TiO_2 absorption wavelength to the visible light region and to stop electron and hole pair recombination.

2.7 Modification of TiO_2 to respond under visible light

As mentioned earlier, TiO_2 has a wide band gap energy which limits its practical applications using solar light. Therefore, designing an effective visible light photocatalyst is essential from both an energy and economic point of view. In the preparation of TiO_2 visible light photocatalysts, morphological and electronic modification of the TiO_2 nanostructure is very important. A brief explanation is given here of the common approaches which have been used to extend the band gap energy of TiO_2 photocatalysts to the visible light region (Figure 2.6). Also, the specific objectives behind these optimisation processes are summarised in Table 2. 2.

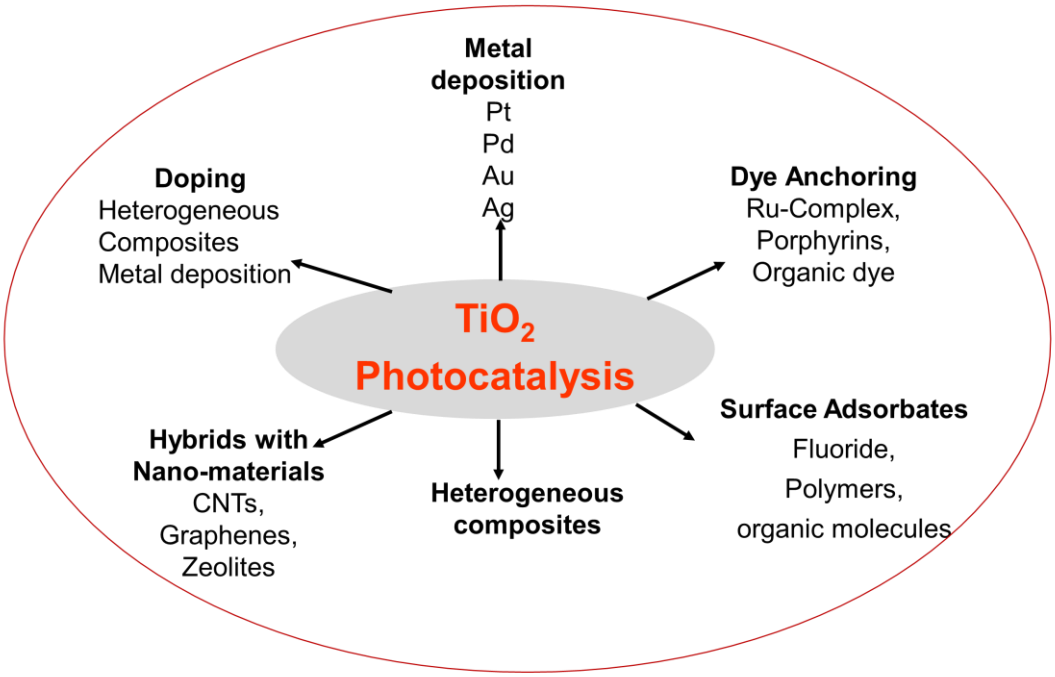

Figure 2.6 : Various approaches for TiO_2 photocatalyst modification

Table 2. 2 Shows that depending on the objectives behind different investigations, there is an extended literature on the optimisation approach and mechanisms to produce modified TiO_2 nanoparticle. Some investigations were done to extend the band gap energy of TiO_2 from the use of UV to visible light and a lot of studies were done to improve the photoefficiency of modified TiO_2. In addition, Table 2. 2. Shows that all TiO_2 modification are done to produce materials for different applications such as high performance UV activated materials and low energy costs materials for solar applications.

Table 2. 2 : The TiO_2 photocatalyst optimisation processes and their objectives

Optimisation objectives	Optimisation approaches	Optimisation mechanisms	Wastewater Applications
Enhance photocatalytic reaction kinetics	Surface area increment	More surface reactive sites, higher reactant adsorption, lower e^-/h^+ recombination	High performance UV activated photocatalytic reaction
	Nano-tube morphology	Shorter carrier diffusion in the tube walls, higher reactant mass transfer rate toward tube surface.	
	Noble metal doping	Better e^-/h^+ separation, lower e^-/h^+ recombination	
	Reactive crystallographic facets	Higher reactant sorption, better e^-/h^+ recombination	
Expanded photoactivity range	Metal impurity doping Anion doping Dye sensitiser doping Narrow ban-gap Semiconductor doping	Separation, lower e^-/h^+ recombination Impurity energy levels, Band gap narrowing Electron injection Electron injection	Low energy cost for solar, Visible light Photocatalytic reactors

2.7.1 Dye anchoring/sensitisation

Li and co-authors reported that the system requires molecular dye and a TiO_2 photocatalyst. Upon visible light irradiation, the dye is excited and the excited dye molecule transfers an electron into the CB of TiO_2. This injected electron in the CB reacts with the oxygen molecule adsorbed on the TiO_2 surface to generate active oxygen species such as $^{\bullet}OH$ (Li *et al.*, 2002). It is reported by Gupta and co-authors that organic dyes have a push-and-pull structure with an anchoring group (cyanoacrylic acid, carboxylic acid and rhodanine-3-acetic acid) which will allow dyes to adsorb on the oxides surface by carboxylic groups (Gupta *et al.*, 2015).

Using this dye anchoring strategy to form visible light TiO_2 photocatalysts, enhanced photoefficiency was reported for the degradation of 2,4-dichlorophenol using TiO_2 nanoparticles and xanthene dye as synthesiser (Li *et al.*, 2002). More observations on dye anchoring were carried out by Gupta & Triphati (2011), who reported that electrons and hole pairs recombination in dye sensitisation systems depend on the properties of TiO_2

nanoparticles used, the type and nature of the dye in question, and the resultant dye-nanoparticle interaction.

Moreover, Benkö *et al.* (2003) reported that the e^-/h^+ pair injection increases proportionally with the nanoparticle`s crystallinity. Benkö and co-authors also reported that one layer of dye coated to a high particle surface area is used to achieve the maximum photocatalytic performance (Benkö *et al.*, 2003). In a survey of photocatalytic materials for environmental remediation, written by Di Paola *et al.* (2012), it was reported that the anchored catalyst has better visible light photocatalytic performance than bare TiO_2. However, Benkö and co-authors reported that the drawback with this approach is that, as one increases the crystallinity, one eliminates the trapping states and one creates the surface state that increases the rate of back electron transfer to the oxidised dye.

2.7.2 Substitution of different metals or anions/cations to the Ti or oxygen sites

This is an approach used to introduce another compound into the TiO_2 structure in order to alter its optical properties to produce a visible light photocatalyst. There is a wide range of materials that have been reported by Han *et al.* (2009) as doping materials from metals and transitional metals to non-metals on the periodic table.

2.7.2.1 Modification with noble metals

Noble metal doping into TiO_2 nanoparticles has received much attention as a potential method of increasing the photocatalytic efficiency of TiO_2 (Han *et al.* 2009). It has been reported by Han and co-authors that noble metal doping can be used to shift the TiO_2 band gap from UV light to visible light, facilitating e^-/h^+ pair separation (Han *et al.*, 2009). It has been reported by Tan and co-authors that noble metal doping improves the photoefficiency by trapping photogenerated conduction band electron. Moreover, they reported that noble metal may process a localised surface plasmon resonance (LSPR) phenomenon which enable them to absorb visible light (Tan *et al*., 2015). However, during combination of noble metals and TiO_2, higher dosage levels have been reported to have a negative effect on photoactivity due to the creation of e^-/h^+ pair recombination centres (Aazam, 2016).

2.7.2.2 Modification with transition metal/cation-doped TiO_2

It has been reported by Han *et al.* (2009) that the modification of TiO_2 with transitional metal provides successful and cost-effective visible light photocatalysts.

It has been explained by Gupta & Triphati (2011) that transition metal ions are used to add extra energy levels in the TiO_2 semiconductor`s band gap. Therefore, excitation of electrons from these additional levels to the conduction band will require less absorption photo-energy than the energy that would be required for unmodified TiO_2 (Gupta & Triphati, 2011a). Cation (Fe, Cr, V, Mo, Ni, Nb, Mn, Cu and Co) doping with powdered TiO_2 has been carried out and many cation groups have been investigated to assess their effect on the TiO_2 absorption properties (Henderson, 2011). Doping of TiO_2 with metal ions such as Fe(III), Mo(V), Ru(III), Os(III), Re(V) and V(V) has created a catalyst with an improved trapping-to-recombination rate ratio (Gupta & Triphati, 2011a) . The photocatalyst showed enhanced photocatalytic efficiency for the photo-oxidation and reduction of $CHCl_3$ and CCl_4 respectively (Gupta & Triphati, 2011a).

However, literature shows that as with noble metals, cationic dopants in high concentration act as recombination centres with formation of localised d-states in TiO_2 (Y. Zhang *et al.*, 2014). Moreover, high concentrations of cations inhibit the penetration of light into TiO_2 structures, and they become trapping sites of electrons and holes. Therefore, it has been reported that transition metal doping decreases the lifetime of charge carriers and the e^-/h^+ pair recombination rate increases, which result in lower photocatalytic activity (Joshi *et al*., 2009).

2.7.2.3 Modification with lanthanide metals

Lanthanides have a special electronic structure of $4f^x5d^y$ which favours different optical properties and combination with other structures and enhancement of photocatalytic efficiency. Han *et al.* (2009) report that Lanthanides have an effective adsorption ability of organic compounds on the surface using TiO_2 due to their f-orbital interaction with other structures. Moreover, it was reported that when lanthanides are confined to the TiO_2 surface, they can trap conduction band electrons (Uzunova-Bujnova *et al*., 2008). Therefore, Lanthanum ion doping accelerate the separation of photo-induced electron-hole pairs (Li & Feng, 2016).

2.7.2.4 Anion-doped TiO_2

There has been an explosion of research on the subject of anion-doping of TiO_2 as an oxygen (O_2) substitute in TiO_2 lattices to enhance visible light. There are also studies available on N, C, S, P, F and B-doped TiO_2 for visible light photoactivity (Joshi *et al*., 2009). In this system, there is a mixing of p-states of dopants anion with 2p-states of oxygen. As a result of this, the valence band edges are shifted upwards, decreasing the band gap energy of TiO_2 to enable it to absorb visible light (Ahmadi *et al.*, 2014). By adding N to TiO_2 there is a significant shift of

the absorption edge in the visible light range, caused by mixing of the N 2p states with the O 2p states in TiO_2 (Di Paola et al., 2012; Gupta & Triphati, 2011).

In doping TiO_2 with carbon, many studies have focused on activated carbon (AC) and TiO_2/CNT composites. As reported by Gupta & Triphati (2011), these compounds have a particular 1D structure which facilitates the charge transfer for effective organic pollutants degradation. Moreover, conjugated carbon materials on TiO_2 have been investigated. These are added to TiO_2 for surface hybridisation (Gupta & Triphati, 2011). As illustrated in Figure 2.7, doping TiO_2 with anion creates a new energy level between the valence and conduction band of TiO_2, decreasing its band gap to enable visible light absorption (Lazar *et al.*, 2012).

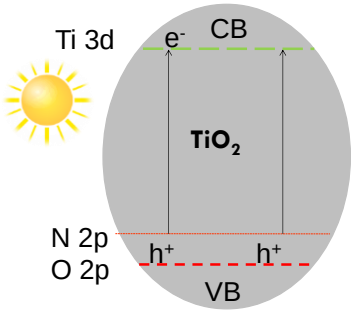

Figure 2.7 : Valence band shifting in TiO_2 nanoparticles by doping

According to Gupta and Triphati (2011), anions which are less electronegative than oxygen produce higher photocatalytic efficiency when substitutionally doped into the TiO_2 lattice. Anion-doped TiO_2 produces enhanced photocatalytic activity when compared with cation-doped TiO_2, because anions are unlikely to form e^-/h^+ pair recombination centres. The same observations has been made by Y. Zhang *et al.* (2014) that anion doping is better suited to extend visible light absorption than cation doping. Zhang and co-authors explained that when anions are attached with impurities their state more closely approaches the maximum valence band, keeping the minimum conduction band at H_2/H_2O potential energy level (Y. Zhang *et al.*, 2014).

2.7.2.5 Co-doping and multi-doped TiO_2

Co-doping and multidoping is used when more than one cation or anion is doped into the TiO_2 lattice, or with a cation and anion co-doped into the TiO_2 lattice to enhance visible light photocatalytic performance.

As reported by Gupta and Triphati (2011) co-doping of TiO_2 may be used as an effective way to improve charge separation. It was also reported by Y. Zhang *et al.* (2014), that introducing two or more elements into the TiO_2 monocrystalline increase its photoefficiency (Y. Zhang *et al.*, 2014).

In the study of visible light photocatalytic decomposing of xylenol orange using Cu, N co-doped TiO_2, the system showed a significant photoefficiency improvement when compared to undoped TiO_2 and TiO_2 doped with pure Cu or N (Kaixi *et al.*, 2008). Also many more TiO_2 co-doped systems such as (Eu^{3+}, Fe^{3+}); (Ce, C); (N, Ce) and Ag/V-TiO_2 are said to exhibit high photocatalytic degradation of different organic compounds (Gupta & Triphati, 2011a). However, it is also reported that photoactivity of TiO_2 is affected by co-doping of TiO_2 with non-metal and transition metal ions since the process results in a synergistic effect (Gupta & Triphati, 2011).

2.7.3 TiO_2 heterojunction/composite

It has been reported by Gupta & Triphati (2011) that with composite photocatalysts, TiO_2 is coupled with a narrower band gap semiconductor to form a composite structure. A heterojunction structure is formed within the composite as an interface between different semiconductors. Gupta & Triphati (2011) further reported that coupled semiconductor photocatalysts enhance high photocatalytic performance by increasing charge carrier separation and extending the band gap energy range of photo-excitation to visible light. The authors explained that upon visible light irradiation, the narrower band gap semiconductor produces a response in the TiO_2 semiconductor (Gupta & Triphati, 2011). Rawal and co-authors have shown that the combination of visible light harvesting semiconductors and TiO_2 is a suitable method to produce a TiO_2 visible light photocatalyst (Rawal *et al.*, 2013). Some binary compound such as Fe_2O_3, ZnO, WO_3, V_2O_5, Bi_2O_3, NiO, Nb_2O_5, Ta_2O_5, ZrO_2, CeO_2, Ga_2O_3 and Cu_2O have already been reported to improve visible light photoefficiency of TiO_2 (Di Paola *et al.*, 2012). However, the selection of suitable lower band gap semiconductors is a very important factor in the formation of visible light photocatalysts. Zhang and co-authors reported that there is a high possibility of creating a heterojunction with e^-/h^+ recombination centres, a concept illustrated in Figure 2.8 (X. Zhang *et al.*, 2014; Rawal *et al.*, 2009).

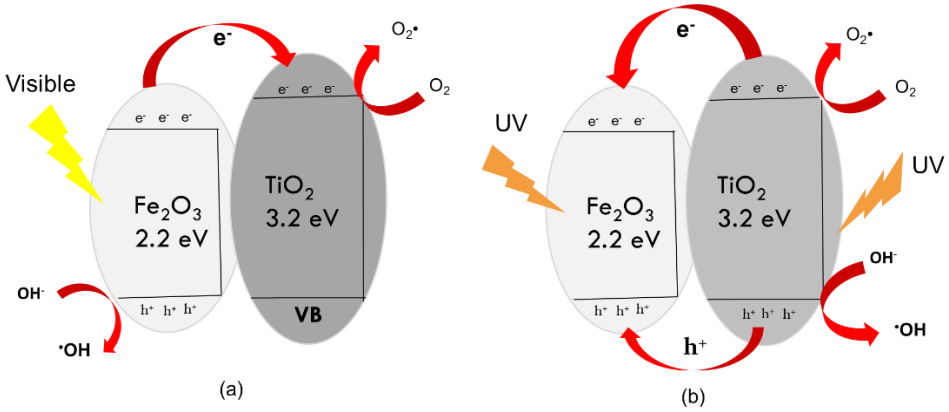

Figure 2.8 : (a) Electron transfer between Fe_2O_3 and TiO_2 under visible light and (b) Electron transfer between Fe_2O_3 and TiO_2 under UV light irradiation.

(Adapted from X. Zhang et al., 2014:47)

Zhang and co-authors have explained the electron and hole transfer mechanism between Fe_2O_3 and TiO_2 under visible light and under UV light. They report that, upon visible light illumination (Figure 2.8a), electrons are excited only from the VB of Fe_2O_3 to its CB. The electrons are then transferred to the CB of TiO_2 at the heterojunction interface by built-in electric fields and the concentration gradient. However, the same authors reported that holes are accumulated in the VB of Fe_2O_3. Moreover, Zhang and co-authors reported that upon UV light irradiation (Figure 2.8b), electrons are excited from the VB of both TiO_2 and Fe_2O_3 to the CB of Fe_2O_3, whereupon the holes of TiO_2 are transferred to Fe_2O_3, making Fe_2O_3 the recombination centre of photo-generated e^-/h^+ pairs (X. Zhang *et al.*, 2014). Rawal and co-authors tested a design of visible light photocatalysts by coupling narrower band gap semiconductors and TiO_2 and investigating the effect of their relative band positions on the photocatalytic efficiency (Rawal *et al.*, 2013).

2.7.4 The effect of relative energy band positions of coupled semiconductors on the photocatalytic efficiency

Rawal *et al.* (2013) classified all the combinations according to the relative energy band position between a coupling or visible light absorbing semiconductor and TiO_2 in three different types of heterojunctions as shown in Figure 2.9.

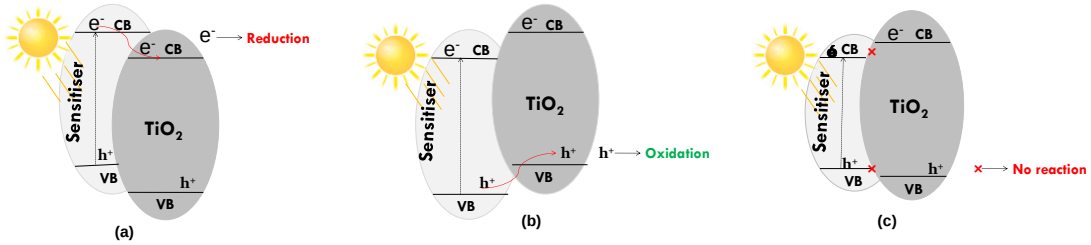

Figure 2.9 : Photo-induced charge flow under visible light irradiation for (a) Type-A, (b) Type-B, and (c) Type-C heterojunction structures.

Adapted from Rawal et al., (2013)

2.7.4.1 Type-A heterojunction:

E.g.: Cu_2O/TiO_2, CdS/TiO_2 and $CdSe/TiO_2$

The VB of the sensitiser is positioned lower (more on the negative side) than that of TiO_2. Rawal and co-authors report that, upon visible light irradiation, the electrons in the VB of the sensitiser are excited to the CB of TiO_2 because the CB of TiO_2 is lower than that of the sensitiser (Rawal *et al.*, 2013). It has been reported that these electrons induce reduction reactions, leading to partial decolouration of organic dyes (Rawal *et al.*, 2009).

2.7.4.2 Type-B heterojunction:

E.g.: $FeTiO_3/TiO_2$, Ag_3PO_4/TiO_2, $W_{18}O_{49}/TiO_2$, and Sb-doped SnO_2 (ATO)/TiO_2

It was reported by Rawal *et al.* (2013) that the VB of a sensitiser is higher than that of TiO_2. With visible light irradiation, the electrons in VB of the sensitiser are excited to its CB. Since the CB of TiO_2 is higher than that of the sensitiser, the holes in the VB of the sensitiser can be transferred to the VB of TiO_2 by inter-semiconductor hole-transfer mechanisms. The photo-generated VB holes assist in oxidation reactions, yielding the complete degradation of organic pollutants (Rawal *et al.*, 2013).

2.7.4.3 Type-C heterojunction:

E.g.: $NiTiO_3/TiO_2$, $CoTiO_3/TiO_2$, and Fe_2O_3/TiO_2

Rawal and co-authors reported that the VB and CB of the sensitiser are located between those of the TiO_2. When visible light irradiates the heterojunction, the electrons in the VB of the sensitiser are excited to its CB, but neither the electron in the CB nor holes in the VB of the sensitiser can be transferred to the CB or VB of TiO_2 due to unfavourable energy band

matching. There is therefore no photocatalytic performance in the degradation of organic compounds (Rawal *et al.*, 2013).

Within these three types, Rawal and co-authors report that the Type-B combination yields more enhanced photocatalytic activity (Rawal *et al.*, 2009; Rawal *et al.*, 2012; and Rawal *et al.*, 2013). Considering all the evidence given by literature, Zhang *et al.* (2014) deduced several critical properties which are required for a suitable coupling material (X. Zhang *et al.*, 2014).

- Suitable narrow semiconductor photocatalysts which absorb visible light.
- Formation of good interface structure and bonding between TiO_2 and doped semiconductor, since this is the key point for the e^-/h^+ pair's recombination process.
- Larger surface area for absorption of dyes to improve charge exchanges between photocatalysts and organic molecules, which result in high photocatalytic performance.

There is an extensive literature base which describes the modification of TiO_2 in the presence of visible light using the abovementioned approaches (as described in section 2.7). In addition, many studies have been carried out with regards to different photocatalysis applications and the results showed significant differences in the obtained photoefficiency. The summary of available studies and their applications are listened in Table 2.3.

Table 2.3 : Previous studies conducted on combined semiconductors with TiO_2

Photocatalyst	Dosage	Application	Concentration	Source of light	Time (min)	References
TiO_2 on porous Vycor glass	1 g/L	Decolourisation of salicylic acid and methylene blue	50 mol/L	125 W high pressure mercury lamp	120	Strauss *et al.*, 2014
Boron co-doped TiO_2	0.06 g/60 mL	Degradation of Acid Orange 7 and 2,4dichlorophenol	20 mg/L	Visible light of 1000 W tungsten halogen lamp	300	Bagwasi *et al.*, 2013
Degussa-P25 80% anatase/ 20% rutile and ECT1023t	1 g/L	Detoxification of the herbicide propanil	1g/L	UV light of Solarium Philips HB175 with four 15 W Philips CLEO lamps	120	González Sánchez *et al.*, 2014
TiO_2	-	Self-cleaning and aesthetic durability of cementitious material	-	Visible and UV light	-	Folli *et al.*, 2012
UV/TiO_2/H_2O_2	1.5 g/L	Degradation of pesticides chlorpyrifos, cypermethrin and chlorothalonil	400 mg/L	6W power UV lamp	30	Affam & Chaudhuri, 2013
N, Ce co-doped TiO_2	-	Methyl orange	5 ppm/70 mL	UV and Visible light 400 W high-pressure mercury lamp	120	Ahmadi *et al.*, 2014
TiO_2/β-FeOOH	0.01 g/50 mL	Reduction of Cr(VI)	100 μM	UV 100 W medium pressure Hg lamp	120	M. Zhang *et al.*, 2014
Multi-doped TiO_2	1 g/50mL	Photocatalytic treatment of 2,4,6-trinitotoluene in red water	149 mg/L	Visible light	720	Y. Zhang *et al.*, 2014
1DFe_2O_3@TiO_2core–shell	10 mg/L	Methyl orange (MO) in aqueous solution	10 mg/L	10 W UV lamp	80	(X. Zhang *et al.*, 2014)

Photocatalyst	Dosage	Application	Concentration	Source of light	Time (min)	References
Bi-B-TiO_2	0.06 g /60mL	Acid orange7 (AO7) and 2, 4-dichlorophenol (2, 4-DCP)	20 mg/L	1000 W Halogen tungsten lamp	300	Bagwasi *et al.*, 2013
Polypyrrole /TiO_2	20 mg /100 mL	MO	105 µmol/L	300 W Xenon lamp	120	Deng *et al.*, 2012
GR–TiO_2 and GR/Fe^{3+}–TiO_2	-	MB	4.5 ppm /40mL	Visible light	165	Low & Boonamnuay vitaya, 2013
MnO_2/TiO_2	0.8 × 2 cm^2	Acid Orange II	10 mg/L	Visible light	120	Xu *et al.*, 2014
CdSe/TiO_2; ATO/TiO_2, Ag_3PO_4/TiO_2, $W_{18}O_{49}$/TiO_2; $NiTiO_3$/TiO_2, $CoTiO_3$/TiO_2, and Fe_2O_3/TiO_2	8.0 mg	2-propanol (IP) in the gas phase	200 mL	300W Xenon lamp	120	Rawal *et al.*, 2013
MoO_3/TiO_2 WO_3/TiO_2	4 cm^2	2-propanol in gas-phase	200 mL	300 W Xenon lamp	60	Song *et al.*, 2001
N-$SrTiO_3$/TiO_2	-	Hydrogen production	-	Simulated sunlight lamp	-	Su *et al.*, 2016
N−F/TiO_2	0.02g /100 mL	MO	20 mg/L	UV light with a 300 W	120	He *et al.*, 2012
MWCNT/TiO_2	0.8 g/L	MO	10 mol/L	12 UVA lamps of 8 W	70	Da Dalt *et al.*, 2013

Photocatalyst	Dosage	Application	Concentration	Source of light	Time (min)	References
Ag/AgCl @ chiral TiO_2 nanofibers	0.1 g/100 mL	Ethinyl estradiol (EE2)	5 mg/L	300 W Xe arc lamp with a UV cut-off filter	12	Wang *et al.*, 2015b
TiO_2@MoS_2 heterostructures	4 mg/80 mL	Hydrogen evolution	-	A 300 W xenon arc lamp	-	Liu *et al.*, 2015
Ag/AgCl @ chiral TiO_2 nanofibers	-	Urban wastewater effluents treatment	-	150 W xenon light	120	Wang *et al.*, 2015a
Rutile and Degussa P25 TiO_2	1g/100mL	Removal of synthetic dye Direct Fast Blue B2RL	941 mg/L	15 W UVA light bulb	200	Mekkawi & Galal, 2013
TiO_2 graphene composites	500 mg/L	E. coli and F. solani spores	10^6 CFU/mL	sunlight	300	Fernández-Ibáñez *et al.*, 2015
Bi_2O_3/TiO_2	0.5 g/L	Ofloxacin drug	25 mg/L	Solar radiations (I =70.3 K lux)	120	Sood *et al.*, 2015
Fe/TiO_2	0.1g/ 200 mL	Phenol	-	UV lamp (757.28 W/m2)	120	Akhlaghian & Sohrabi, 2015
Cu_2O, Bi_2O_3 $ZnMn_2O_4$ /TiO_2	10 mg/L	Orange II, 4-hydroxybenzoic acid and benzamide	50 mg /100mL	vapour Xenon lamp		Bessekhouad *et al.*, 2005
Bi_2S_3/TiO_2	50 mg/100 mL	Orange II, 4-hydroxybenzoıque acid and benzamide (BZ)	10 mg/L	Xenon lamp	30	Bessekhouad *et al.*, 2004
Cu_2O-CuO /TiO_2	125 mg/L	Reactive Blue 49 (RB 49), Reactive Red 24 (RR 24) and Reactive Yellow 160 (RY 160)	5 mg/L	30 W UV irradiating tubes	120	Ajmal *et al.*, 2016

2.8 Combination of iron oxides with TiO_2 to form visible light photocatalysts

Nowadays, research effort is directed towards the combination of iron oxides and TiO_2 because of their availability, in addition to their visible light photocatalytic properties.

2.8.1 Different phases of iron oxides nanoparticles and their applications

There exist many different phases of iron oxides, such as FeO, Fe_3O_4, α-Fe_3O4, γ-Fe_2O_3, β-Fe_2O_3, ε-Fe_2O_3, α-FeOOH, β-FeOOH, γ-FeOOH and δ-FeOOH, etc. They have almost a similar molecular structure but they have different physicochemical and photocatalytic properties. The applications of iron oxides vary with their phases, as illustrated by Table 2.4. They have potential applications in different areas including catalysts, lubrications, sorbents, ion exchangers, magnetic recording, ink and toners for xerography.

Table 2.4: Various iron oxide nanoparticle phases and their applications.

(Ramimoghadam *et al.*, 2014; Ortega-Liebana *et al.*, 2015)

Iron oxide phase	Notation	Band gap (eV)	The application
Magnetite	Fe_3O_4	0.1	Catalyst
Hematite	α-Fe_3O_4	2.2	Magnetic data storage
Maghemite	γ-Fe_2O_3	2.03	Semiconductors
Goethite	α-FeOOH	2.1	MRI
Akaganeite	β-FeOOH	2.12	Wastewater treatment
Lepidococite	γ-FeOOH	2.06	Pigments
Feroxyhyte	δ-FeOOH	2.25	Gas sensing
Iron hydroxide	$Fe(OH)_2$	-	Coatings
Ferridrite	$5Fe_2O_3•9H_2O$	-	Lubricants
Wustile	FeO	2.3	Sorbents

2.8.2 Iron oxide based TiO_2 photocatalyst

As mentioned above, the challenge is to identify the most appropriate iron oxide which can be coupled with TiO_2 and produce a heterojunction with excellent visible light photocatalytic efficiency. A search of the literature reveals that many of these iron oxides have not been investigated as photocatalysts and few of them have been tested individually or in combination with other semiconductors. Table 2.5 summarises available studies on the photocatalytic performance of iron oxide in combination with TiO_2.

Though scarce, studies on iron oxides and TiO_2 systems such as γ-FeOOH/TiO_2 and Fe_2O_3@TiO_2 have shown that iron oxides have high potential to improve TiO_2-based visible light photocatalytic efficiencies (Zhang *et al.*, 2014). Rawal and co-authors have investigated FeOOH/TiO_2, using FeOOH with band gap of 2.6 eV. They have found out that the photocatalytic performance of FeOOH/TiO_2 under visible light was appreciably higher in decomposing 2-propanol in gas phase. Recently, X. Zhang *et al.* (2014) studied F_2O_3 with a band gap energy of 2.2 eV and they reported enhanced photodegradation of Rhodamine by F_2O_3/TiO_2, under visible light irradiation.

Table 2.5 : The photocatalytic performance of iron oxide combined with TiO_2

Visible light Photocatalyst	Targeted pollutant	Efficiency (%)	Time (min)	Reference
Fe_2O_3@TiO_2core–shell composites	RhB	~ 90	480	X. Zhang *et al.*, 2014
β-FeOOH/TiO_2	Cr(VI) reduction	~ 99	120	M. Zhang *et al.*, 2014b
α-Fe_2O_3–TiO_2/fly ash cenospheres	Rhodamine B	~ 98	70	Liu *et al.*, 2015
Fe_2O_3/TiO_2	Different dyes in water	~ 98	160	Ghorai *et al.*, 2011
TiO_2/Au: Fe_2O_3/ thin films	Industrial wastewater	87	320	Mahadik *et al.*, 2014
Branch-like α-Fe_2O_3/TiO_2	Trimethylene gas sensor	-	-	Lou *et al.*, 2013
Fe_2O_3/TiO_2 nanocomposite	Rhodamine B	60	300	Xia & Yin, 2013
Dendritic α-Fe_2O_3/TiO_2 nanocomposite	Eosin red (ER)	98.4	90	Li *et al.*, 2016
	Congo red (CR)	95.1	30	
	Methyl orange (MO)	1.1	160	
	Methylene blue (MB)	67.7	160	

β-FeOOH was therefore chosen to be coupled with TiO_2 as a suitable semiconductor with a narrower band gap energy, which will form a visible light photocatalyst for the degradation of textile industry wastewater.

To address the above issues, this research project focuses on the development of enhanced visible light photocatalysts. Another focus is on the production of heterojunction structures between a high band gap TiO_2 and lower band gap semiconductor (β-FeOOH) so that the heterojunction at their interface will harvest visible light to generate $^{\bullet}OH$. The main focus of this study is to achieve degradation of textile wastewater using a visible light TiO_2-based photocatalytic system with restricted photo-induced charge carrier recombination.

Furthermore, Zhang and co-authors have detailed the reduction of Cr(VI) by a TiO_2/β-FeOOH photocatalyst, which was considered to have the most enhanced photocatalytic efficiency (M.

Zhang *et al.*, 2014). Moreover, β-FeOOH semiconductors, according to Rawal *et al.* (2013) form Type-B heterojunction structures when coupled with TiO_2 (Rawal *et al.*, 2013). Therefore, β-FeOOH has been selected as a suitable narrow band gap semiconductor for use in conjunction with TiO_2 to achieve high photoefficiency of a TiO_2 heterogeneous photocatalyst under visible light irradiation. The reasons behind the suitability of β-FeOOH are very well explained in the literature. The most commonly-reported properties were also covered by Zhang and co-authors (M. Zhang *et al.*, 2014). They reported that β-FeOOH possesses a smaller band gap energy of 2.12 eV, a suitable, larger surface area which promotes pollutants adsorption, and a large tunnel-type channel structure which facilitates electrons and hole movements.

2.9 Optimisation of operating parameters

2.9.1 Effect of light intensity and wavelength/UV irradiation

According to Ahmed and co-authors relight intensity is an important reaction parameter, since it determines the overall pollutant conversion and degradation efficiency (Ahmed *et al.*, 2011). The overall light intensity and wavelength increases proportionally with photodegradation rates. Behnajady and his co-authors made this observation when they were studying the decolourisation of azo dye AR27 using P-25 as the photocatalyst. However, they discovered that with low light intensity (18.8 Wm^{-2}), the photoreaction rate increases linearly with light intensity, following first order reaction. At medium light intensity the kinetic was half-order, corresponding to the square root of the light intensity. For higher light intensities, the reaction rate showed itself to be independent of the light intensities (Behnajady *et al.*, 2007).

2.9.2 Effect of pH

Ahmed and co-authors reported that in polluted water, organic compounds have different physicochemical properties, such as speciation, solubility and hydrophobicity behaviour which influence their photodegradation rate. The authors further reported that the pH of a solution affects the ionisation (speciation pKa) of organic pollutants, since they are neutral at a pH lower than their pKa value and negatively charged above that pKa value. It was added that the pH of the solution affects the surface charge of the photocatalyst and the size of aggregates it can form. In addition, it was reported that the PH of the suspension affects electrostatic interaction between the surface of the photocatalyst, substrate and water affecting the formation of charged radicals during photocatalytic oxidation processes (Ahmed *et al.*, 2011).

Moreover, Hoffmann and co-authors have calculated the zero charge point of TiO_2 (Degussa P25) to be the pH of 6,25 (Hoffmann *et al.*, 1995). Ahmed and co-authors added that the surface of TiO_2 gets more positively charged in acidic medium as the pH falls down from the zero charge point and more negatively charged in basic medium as the pH increases higher than the zero charge point (Ahmed *et al.*, 2011).

In the study of Xiang and co-authors on the quantitative characterisation of hydroxyl radicals produced by various photocatalysts, it was observed that the acidic medium promoted formation of $^{\bullet}OH$. It was explained the weakness of the oxidising ability of the valence band hole in an alkaline medium since the redox potential of the valence band hole decreases by 0.059 when the pH increases by one unit. In addition, it was reported that the pH effect is related to ionisation state of the surface according to Eq 2.20 and Eq 2.21. The negatively charged OH^- is adsorbed on the photocatalyst surface of a positively charged TiO_2 in acidic medium. Therefore, pH can influence the adsorption of dye molecule onto the surface of the catalyst enhancing formation of hydroxyl radicals and increasing degradation rate of organic compounds through oxidation reactions (Xiang *et al.*, 2011).

$$TiOH + H^+ \rightarrow TiOH_2^+ \quad \text{Eq 2.20}$$

$$TiOH + OH^- \rightarrow TiO^- + H_2O \quad \text{Eq 2.21}$$

2.9.3 Effect of catalyst load

Affam and Chaudhuri (2013) reported that the amount of catalyst used is an important factor in photo-reactor design. A number of studies have indicated that the photodegradation rate increases with photocatalyst loading until a certain point when further photocatalyst loading will result in lower photocatalytic activity, because of light scattering and catalyst particle aggregation at high concentrations (Affam & Chaudhuri, 2013). Ahmed and co-authors reported similar results during their investigation. It was reported that an increase in catalyst load results in enhanced photoactivity due to an increase in active sites. However, it was reported that there exists an optimum value when higher solid concentration results in lower photoefficiency due to the reduced surface area available for light absorption (Ahmed *et al.*, 2011).

2.9.4 Effect of H_2O_2 concentration

Some researchers have investigated the effect of an electron acceptor or donor in photocatalytic systems. Ahmed and co-authors reported that molecular oxygen is the general known electron acceptor. They have also reported the use of H_2O_2, $KBrO_3$ and $K_2S_2O_8$ and reported that in all cases an electron acceptor influences the photocatalytic system via three different approaches.

Firstly, by it enhances electron/hole pair separation by reacting with conduction band electrons. Secondly, it increases the hydroxyl radical concentration and oxidation rate of intermediate organic compounds. Lastly, it generates of more hydroxyl radicals and other oxidising species, which enhances the photodegradation of pollutants. They added that in the absence of a suitable electron acceptor, there is no separation of photogenerated charge carriers, resulting in lower photocatalytic activity (Ahmed, *et al.*, 2011).

In a study conducted by Daneshvar and co-authors, it was shown that peroxide is the suitable electron acceptor which inhibits electron-hole recombination by accepting the conduction band electron (Ahmadi *et al.*, 2014; Daneshvar *et al.*, 2004; Pekakis *et al.*, 2006). Affam & Chaudhuri (2013) reported the highest photocatalytic performance as being achieved by the addition of 100 mL/L H_2O_2. They pointed out that lower concentrations of H_2O_2 result in low photodecomposition of organic compounds due to direct photolysis of peroxide under UV light.

Thus, with a lower peroxide concentration, there is decreased generation of hydroxyl radicals according to the available concentration of H_2O_2 (Affam & Chaudhuri, 2013). However, it was reported by the same authors that excess H_2O_2 concentration resulted in lower photocatalytic performance because excess peroxide scavenges hydroxyl radicals which should be used for organic compound photodecomposition purposes. They reported that reactions between H_2O_2 and hydroxyl radicals form a weak oxidant which scavenges useful formed hydroxide radicals (Affam & Chaudhuri, 2013).

2.10 Conclusion

In general, wastewater treatment is the solution to the scarcity of water in the world. The existing technologies of biological and chemo-physical processes such as membranes and reverse osmosis are naturally used. However, these technologies are expensive and ineffective for the removal of some wastewater compositions such as synthetic dyes due to their non-biodegradable nature. Immobilised photocatalyst is also under development to facilitate separation processes for the applicability of heterogeneous photocatalysis systems in real world situations, especially with regard to degradation of dyes from textile industry. Comparing the existing and new advanced oxidation processes, including photocatalysis for wastewater treatment, there are always advantages and side-effects on both sides. So far, TiO_2 photocatalysts using UV light have shown high potential for the degradation of wastewater pollutants. However, the system is still under investigation to optimise its photoefficiency under natural sunlight and this study explores it further. In particular, this study focuses on the combination of Akaganeite (β-FeOOH) and TiO_2. It is known from the literature that β-FeOOH has a lower band gap energy of 2.12 eV and a tunnel structure which make it a promising material which can be combined with TiO_2 to form β-FeOOH/TiO_2 heterojunction structure as a visible light photocatalyst.

CHAPTER 3. EXPERIMENTAL PROCEDURE

3.1 Introduction

In this chapter, the design and methodology which was used to achieve the objectives of this study are discussed in depth. Also, the chapter covers the materials, equipment and the procedure used to prepare and evaluate photocatalytic activity of β-FeOOH/TiO_2. Moreover, a full methodology is given for the characterisation and recycling of the prepared photocatalyst material.

3.2 Material and method

3.2.1 Research material

Iron (III) chloride hexahydrate ($FeCl_3$•$6H_2O$), ammonium hydroxide (NH_4OH) and hydrochloric acid (HCl) used were purchased from B & M Scientific, in Cape Town, South Africa and were used as received. Methyl orange (MO), Synoset Yellow (SY2Y), Synoset Grey (SG) and Synoset Red (SY2R), as well as real textile wastewater were obtained from Falke textile industry in Bellville (Cape Town, South Africa). A purity analyst system was used to obtain deionised water (16MΩ). The benchmark commercial TiO_2 P-25 Degussa of 80% anatase and 20% rutile was used throughout the study and 30% peroxide solution (H_2O_2), both of which were purchased from SIGMA.

3.2.2 Hydrothermal precipitation of β-FeOOH nanoparticles

The iron oxyhydroxide (β-FeOOH) nanoparticles synthesis was carried out using a batch reactor (Figure 3.1) by the hydrothermal method derived from the methodology used by Chowdhury (2014). A typical synthesis procedure is as follows:

- A graduated measuring cylinder was used to measure 280 mL ethanol (99% C_2H_5OH), which was mixed with 120 mL of deionised water. Ammonium hydroxide (NH_4OH) was added drop-wise into the solution to obtain a pH of 10.
- 3 g of $FeCl_3$•$6H_2O$ was added into the solution with continuous stirring until the iron salt was dissolved completely. The solution's pH was adjusted to ~2.
- The prepared solution (400 mL) was transferred in a 1L autoclave Teflon-lined stainless steel pressure vessel and heated for two hours at constant temperature of 100 °C. A heating jacket connected to a controller was used to control the temperature (Figure 3.1).

- After the synthesis reaction time of two hours, the reactor was allowed to cool down naturally. The supernatant solution was decanted and then the precipitate was centrifuged and washed three times with ethanol to remove any chloride impurities.
- The solids obtained were dried at 60 °C overnight. The final particles were ground and stored in an appropriate container.

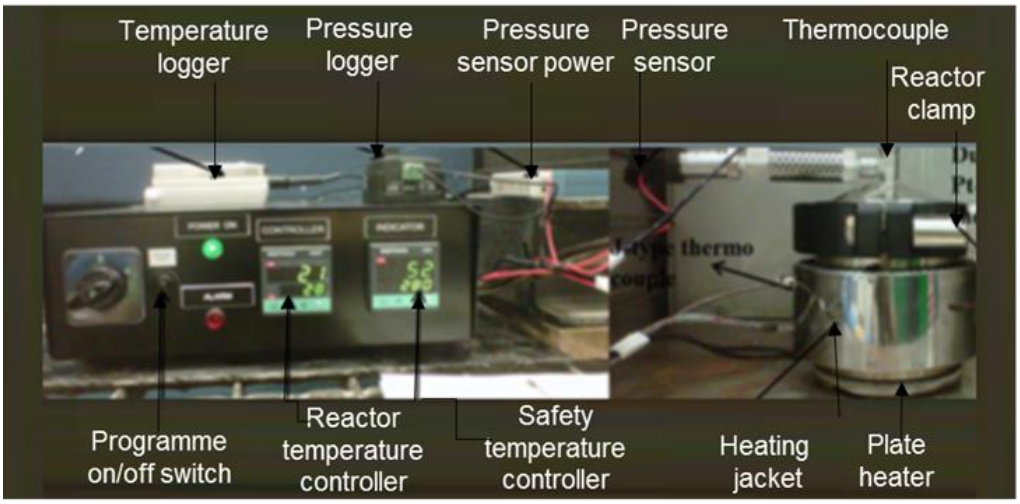

Figure 3.1: β-FeOOH synthesis experimental setup with a controlling unit and autoclave pressure vessel.

3.2.3 Preparation of β-FeOOH/TiO_2 heterojunction/composite structure

TiO_2 nanoparticles were used to synthesise the composite structure. Three different β-FeOOH loading i.e. 2, 5 and 10% β-FeOOH to TiO_2 loading were used to synthesise the heterojunction structures.

For the preparation of 5% β-FeOOH/TiO_2, the following steps were used:

- A solution of 0.1 M maleic acid was prepared by dissolving 5.8035 g of maleic acid into 500 mL of ethanol.
- A solution named A was prepared by adding a mass of 0.05 g β-FeOOH to 30 mL of ethanol and 10 mL of the prepared maleic acid solution into a 250 mL graduated covered bottle with continuous mixing for five hours.
- In a different covered container, a solution named B was prepared by adding 1 g of TiO_2 in 30 mL of ethanol and continuously stirring for five hours.
- Solution A (β-FeOOH-maleic acid and ethanol) was added into solution B and stirred for 12 hours.

- The mixture was centrifuged and then the precipitate was washed several times with deionised water to remove any organic impurities. The solids obtained were dried at 60 °C for 12 hours overnight and calcinated at 220 °C for 4 hours. The final particles were ground and stored in an appropriate plastic container.
- The same procedure was used for the preparation of 2% and 10% β-FeOOH/TiO_2, except that 0.02 g of β-FeOOH and 0.1 g of β-FeOOH was added during the preparation of 2% and 10% β-FeOOH/TiO_2 respectively.

3.2.4 Characterisation of XRD, TEM and FTIR spectrometer analysis

The crystal structures analysis of the prepared products was determined using a Phillips PW 3830/40 Generator with Cu-Kα radiation. The surface methodology of the synthesised crystal was studied using a Tecnai TF20 thermionic TEM, equipped with a La B6 filament and a Gatan GIF energy filter. Images were captured at 200 keV in bright field mode. Selected area electron diffraction (SAED) patterns were obtained using the smallest area aperture available. Infrared spectra were collected with a PerkinElmer 1000 series FTIR spectrometer in the range of 4000-200 cm^{-1} in a KBr matrix. UV-vis diffuse reflectance spectra were collected using a Perkin Elmer lambda 35 spectrophotometer. FTIR spectra were recorded using a Perkin Elmer spectrum 1000. Photoluminescence was measured using a Perkin Elmer 2565 luminescence spectrophotometer.

3.3 Evaluation of β-FeOOH/TiO_2 photocatalyst under simulated solar light irradiation

All photocatalytic tests were carried out using a batch reactor supplied with a halogen tungsten lamp. The halogen tungsten lamp was used to mimic solar light. The reactor used was surrounded by a jacket for a cooling system, as shown by Figure 3.2 and the temperature was increased until a constant value of ±60 °C was attained.
For the photoactivity study the following procedure was applied:

- A 300 W halogen tungsten lamp was positioned inside a cylindrical batch reactor, surrounded by a circulating water jacket to keep the temperature constant.
- A 0.008 g solution of methyl orange and 0.2 g of β-FeOOH/TiO_2 photocatalyst were suspended in 100 mL of deionised water and then 3 mL hydrogen peroxide was added as an electron acceptor.

- The solution was continuously stirred for about 30 minutes in the dark for dye absorption into the catalyst before light irradiation.
- After dye absorption, the solution was irradiated by a 300 W lamp with continuous mixing using a magnetic stirrer.
- A 2 mL sample suspension was regularly (every 15 minutes) drawn from the reactor and the photocatalyst powder was separated from water by centrifugation. A 1 mL filtered sample was diluted to make a 5 mL sample. The residual MO concentration was analysed using a UV-vis spectrometry technique. The calibration curve generated is presented in Figure 3.3.

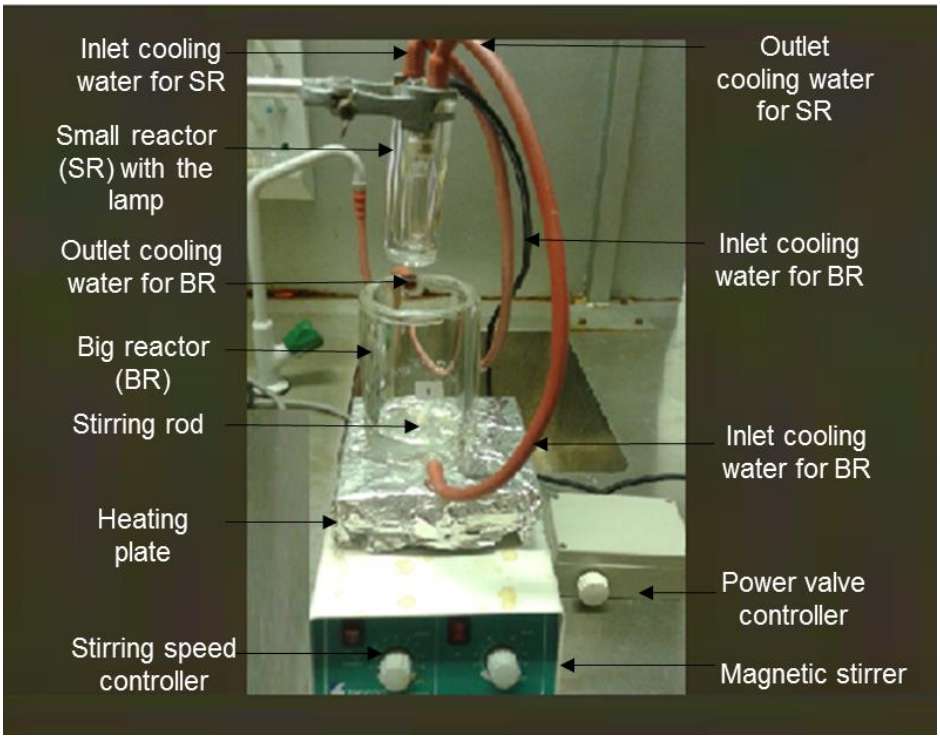

Figure 3.2: The setup for dye photodegradation experiments.

The maximum absorption wavelength for MO solution was determined and found to be 464 nm. The maximum absorption wavelength for commercial metal dyes Sunset Yellow (SY2Y), Grey (SY2R) and Red (SY2G) were found at 444, 586 and 495 nm respectively. To plot the MO calibration curve, MO solutions with different concentrations (0, 1, 2.5, 5, 10, 20, 30, 40 mg/L) were prepared and their absorbances were analysed at 464 nm. Figure 3.3 shows the MO calibration curve correlated from absorbance versus prepared known concentrations. The colour of the solution changes from dark orange to colourless, as the measured absorbances

decrease at the same wavelength. To evaluate the concentration of the supernatant over irradiation time (C_t), the measured absorbance was correlated to its concentration by using the above calibration curve equation.

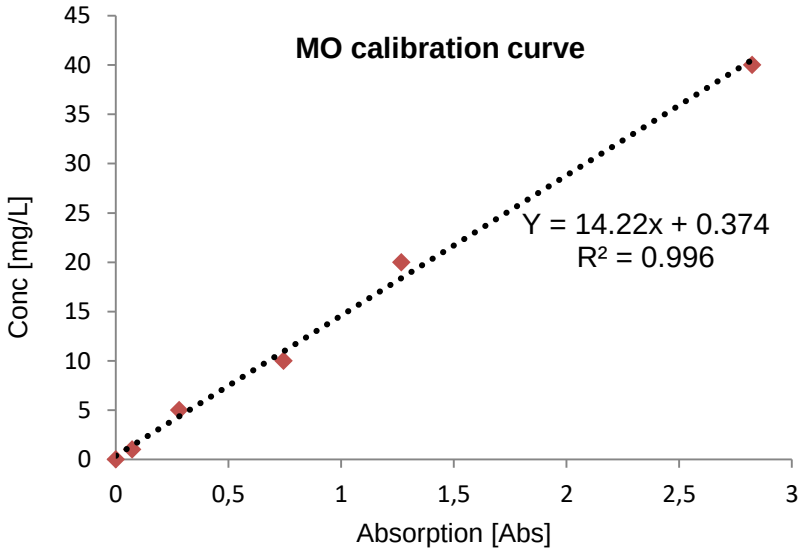

Figure 3.3: MO calibration curve relating the absorbance with concentration.

The process of optimisation was undertaken by studying different process parameters and the best conditions were selected. A summary of the process variables studied is presented in Table 3.1. Moreover, the material was recycled over four different stages. The catalyst was readily recycled by centrifuging it from the solution and used in another batch for experimentation without prior drying or calcination.

Table 3.1: Optimisation of the photocatalytic performance parameters

Sample No	Wattage (W)	pH	Catalyst (mg /L)	Dye type	Dye Concentration (mg/L)	β-FeOOH /TiO_2 ratio	H_2O_2 (mL/L)
Effect of β-FeOOH load in β-FeOOH/TiO_2 heterojunction							
MO1	300	4.5	200	MO	80	10%	30
MO2	300	4.5	200	MO	80	5%	30
MO3	300	4.5	200	MO	80	2%	30
Effect of catalyst loading							
MO4	300	4.5	200	MO	80	5%	30
MO5	300	4.5	100	MO	80	5%	30
MO6	300	4.5	50	MO	80	5%	30
Effect of dye concentration							
MO7	300	4.5	200	MO	25	5%	30
MO8	300	4.5	200	MO	50	5%	30
MO9	300	4.5	200	MO	80	5%	30
MO10	300	4.5	200	MO	150	5%	30
MO11	300	4.5	200	MO	200	5%	30
Effect of light intensity							
MO12	300	4.5	200	MO	80	5%	30
MO13	250	4.5	200	MO	80	5%	30
MO14	150	4.5	200	MO	80	5%	30
Effect of pH							
MO15	300	2	200	MO	80	5%	30
MO16	300	6	200	MO	80	5%	30
MO17	300	7	200	MO	80	5%	30
Effect of H_2O_2							
MO18	300	4.5	200	MO	80	5%	50
MO19	300	4.5	200	MO	80	5%	30
MO20	300	4.5	200	MO	80	5%	10
MO21	300	4.5	200	MO	80	5%	5

3.4 Conclusion

This chapter presented briefly the equipment, material and the procedure used for the preparation and photocatalytic activity evaluation of the β-FeOOH/TiO_2 heterojunction structures. Furthermore, the chapter explained the material structure characterisation method and the experimental method used to study the effect of β-FeOOH in the β-FeOOH/TiO_2 heterojunction structure, the role of H_2O_2 and the effect of fundamental experimental conditions in optimisation of β-FeOOH/TiO_2 photodegradation efficiency.

CHAPTER 4. RESULTS

4.1 Introduction

The results obtained during the experimental work of this research are presented and discussed in depth in this chapter. The structural analysis of the catalysts was performed using various techniques including X-ray diffraction (XRD), Transmission electron microscopy (TEM) and Fourier Transform Infrared Spectroscopy (FTIR spectra). These techniques were used to evaluate the differences between the pristine TiO_2, β-FeOOH and synthesised β-FeOOH/TiO_2 heterojunction structures. The effect of various processing parameters, i.e. hydrogen peroxide, initial dye concentration, light intensity, solution pH and catalyst loading was evaluated and reported in this chapter. A comparison between the developed photocatalyst and the ones reported in the literature is also presented in this chapter. Reusability and its application in commercial dye degradation was evaluated and discussed in this chapter. Lastly, the enhanced photocatalytic activity of the catalyst was derived and critically analysed in this chapter.

4.2 Structural characterisation of β-FeOOH/TiO_2 heterojunction structure

4.2.1 X-ray diffraction analysis

XRD patterns were obtained for individual materials in order to investigate the structural changes which occur after the formation of a chemically bonded interface between β-FeOOH and TiO_2 to produce β-FeOOH/TiO_2 heterojunction structure. The resulting XRD patterns of the pure β-FeOOH (JCPDS, NO.42-1315), TiO_2 (JCPDS, NO.71-1166) and three different mole ratios of 2%, 5% and 10% β-FeOOH/TiO_2 heterojunction structures are illustrated in Figure 4.1a. It demonstrates the diffraction peak visibility of ultra-small β-FeOOH and TIO_2. The XRD patterns of 2%, 5% and 10% β-FeOOH/TiO_2 heterojunction structures do not show the diffraction peaks which were observed for the pristine β-FeOOH material. The loss of these peaks is possibly due to the fact that data obtained from XRD is insensitive to the distribution of Ti and Fe in oxides, since X-rays are scattered by electron density. Therefore, in the case of Ti and Fe, the same electron numbers make it more difficult to distinguish (Pal *et al.*, 1999).

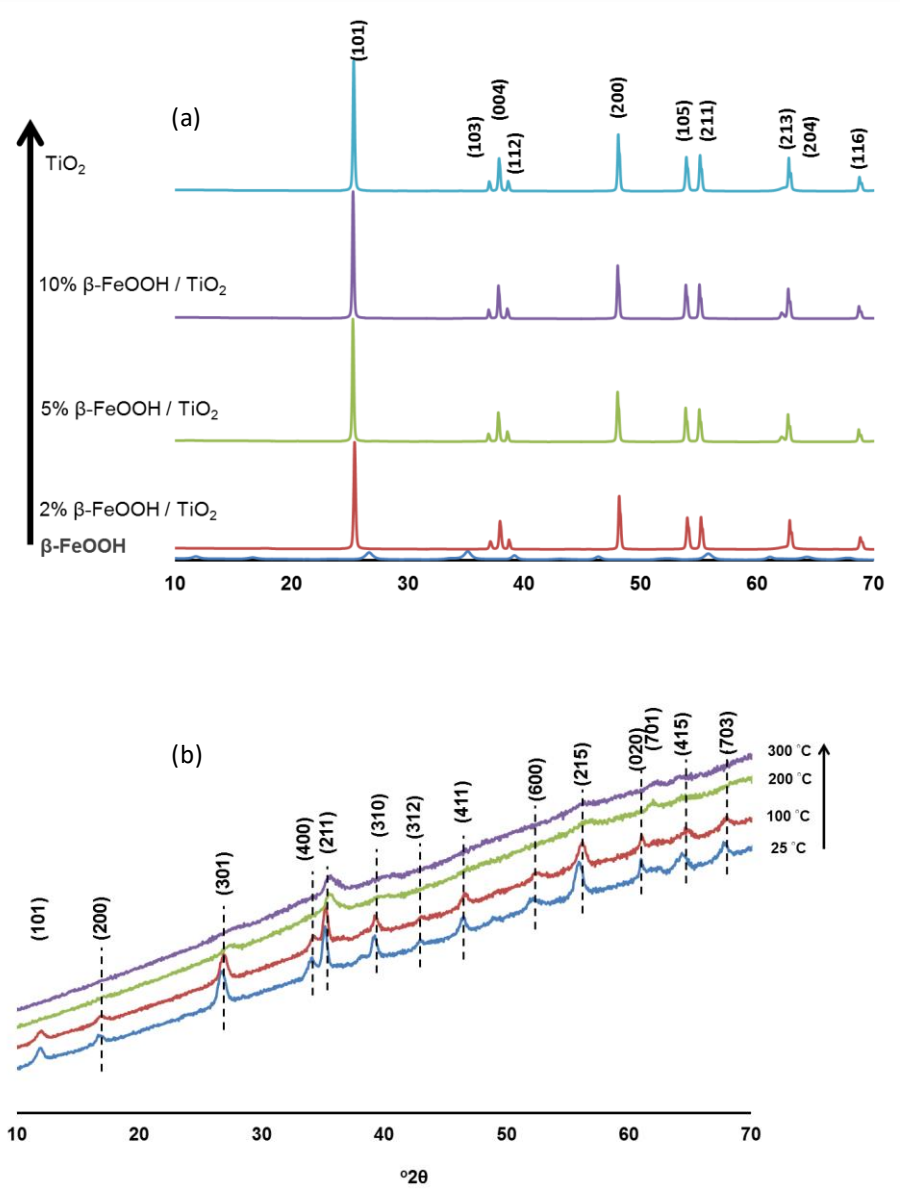

Figure 4.1: (a) XRD patterns of the different materials and (b) high-temperature XRD patterns of β-FeOOH nanorods.

However, there is a presence of β-FeOOH within the β-FeOOH/TiO_2 nanocomposite, as the catalyst was synthesised at lower temperatures to ensure that its structure was not destroyed by the high temperature. Previous research work shows that the morphology of β-FeOOH nanorods remains the same up to 300 °C of annealing temperature in the air (Chen *et al.*, 2008). β-FeOOH nanorods in air can be sustained to temperatures as high as 300 °C, as shown in Figure 4.1b. Hence, it was assumed that no phase transformation of β-FeOOH material occurred during the annealing stage of β-FeOOH/TiO_2 composite material.

4.2.2 TEM results of TiO_2, β-FeOOH and β-FeOOH /TiO_2 heterojunction structure

TEM images were also used to evaluate the morphology of the synthesised materials. Figure 4.2 illustrates TEM images of the pristine TiO_2, β-FeOOH nanorods and 5% β-FeOOH/TiO_2 heterojunction structure. The figure demonstrates clearly that there is a difference in morphology and size of individual materials and the product from their combination. As reported by Zhang and co-authors, the bigger particles of the product show that the β-FeOOH/TiO_2 heterojunction structure has a larger surface area, which leads to the increase of reaction contact area between photocatalyst and dye (M. Zhang *et al.*, 2014).

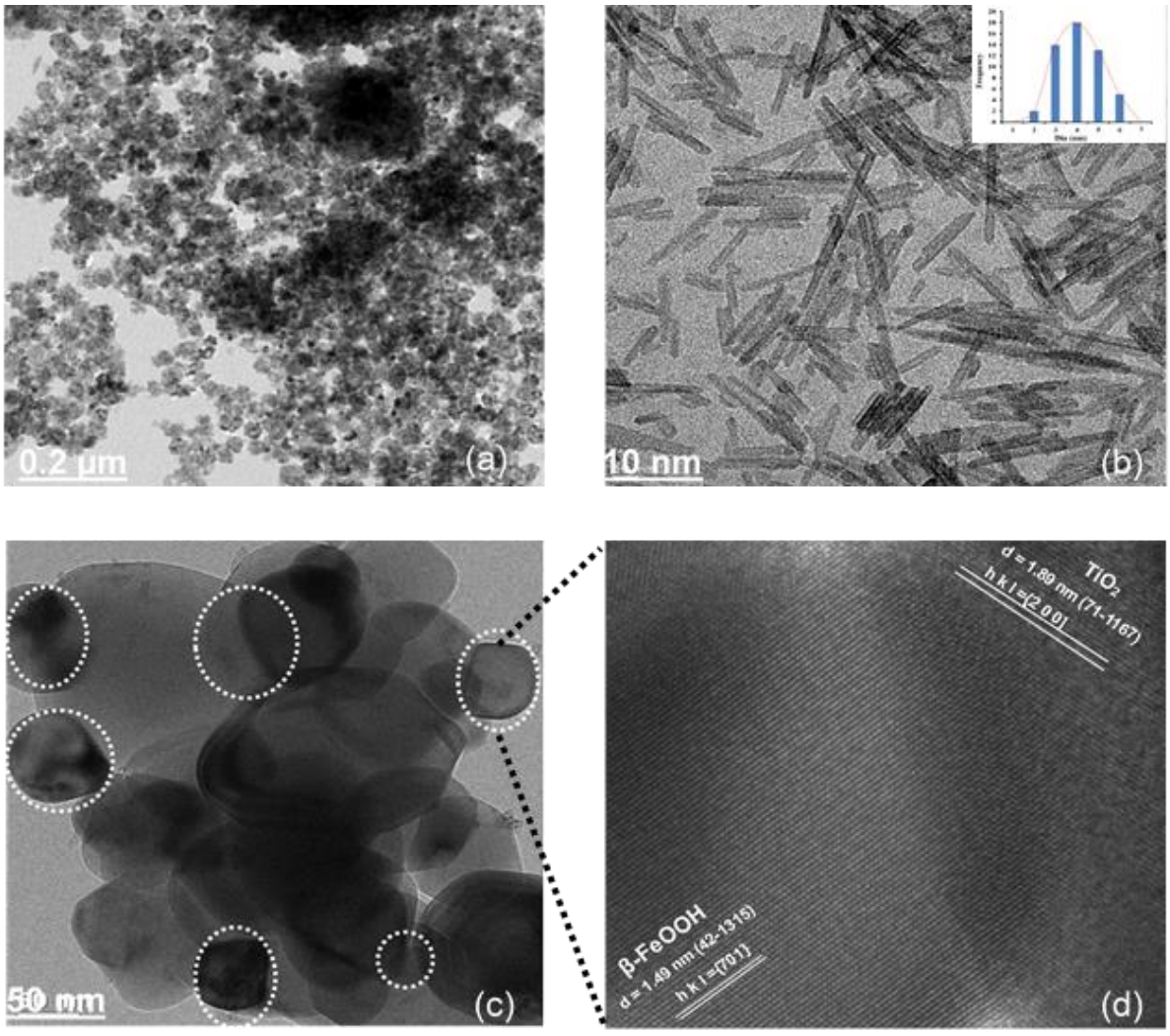

Figure 4.2: (a) TEM image of TiO_2 nanoparticles, (b) TEM image for β-FeOOH, (c) TEM image of 5% β-FeOOH/TiO_2 heterojunction structure and (d) HRTEM of 5% β-FeOOH/TiO_2 heterojunction structure.

It is visible from the TEM image that TiO_2 nanoparticles (Figure 4.2a) have a single morphology with almost globular structures and loose agglomeration, with a particle size of 0.24 µm. β-FeOOH (Figure 4.2b) has a very narrow size distribution, cylindrical-like or rod-shaped structures with average particle size of 10 nm.

Interestingly, an unexpected observation was seen in the TEM grid (Figure 4.2c) of β-FeOOH/TiO_2 heterojunction structure. It can be seen that the synthesised material has an oval-like shape with no rod-like structure. The structure features are tightly packed, with small and large particles which can be characterised by an elongated diameter. Therefore, to get more insight into the synthesised β-FeOOH/TiO_2 heterojunction structure, further observations were carried out using HRTEM.

The HRTEM image of β-FeOOH/TiO_2 structure in Figure 4.2d shows that the measured d-spacing of the particles was 1.49 nm for small particles and 1.89 nm for the larger ones. The d-spacing value of the smaller particles matches with the (701) plane of the pure β-FeOOH particles (JCPDS, No. 42-1315) and the big particles matched with the diffraction plane 200 for TiO_2 particles (JCPDS, No. 71-1167). It is reported by Chowdhury and co-authors in their study that β-FeOOH transforms into α-Fe_2O_3 at elevated temperatures. In their study, they conducted tests to show that β-FeOOH nanorods self-assemble into a α-Fe_2O_3 pseudo cube or spherical particles during hydrothermal synthesis at a temperature of 120 °C. They also demonstrate that the morphology of β-FeOOH changes via oriented attachment mechanism over long synthesis periods (Chowdhury *et al.*, 2014).

However, at temperatures of 300°C, the β-FeOOH nanorods were still present, as seen from the TEM image. Nevertheless, only a single peak of (701) plane of β-FeOOH (JCPDS, No. 42-1315) was observed (Figure 4.2b), even after calcination at 300°C. This XRD peak matched the d-spacing depicted in Figure 4.2d. Therefore, it was postulated that there was no phase transformation during calcination of β-FeOOH at 220 °C. Furthermore, this observation most likely entails that the rod-like β-FeOOH particles changed shape only to spherical-like particles (marked with a white dotted circle, Figure 4.2c) coupled with TiO_2, in the heterojunction structure.

The shape transformation can be explained by the fact that during heat treatment at temperatures of 220 °C, a certain fraction of ultra-small β-FeOOH diffuses into the TiO_2 lattice through the chemically-bonded interface. This is further explained by the fact that the ionic radius of the two ions i.e., Fe^{3+} and Ti^{4+}, are the same, hence the substitution of iron in the TiO_2

matrix can be seen as a favourable process (Pal *et al.*, 1999). It was also confirmed by Zhang *et al.* (2014) that during the synthesis of TiO_2/β-FeOOH composite, the TiO_2 nanoparticles served as heterogeneous nuclei for β-FeOOH growth and that the existence of TiO_2 nanoparticles inhibits the growing up of β-FeOOH nanoparticles (M. Zhang *et al.*, 2014).

4.2.3 FTIR results for structural analysis of TiO_2, β-FeOOH and β-FeOOH /TiO_2 heterojunction structures

For further structural characterisation of β-FeOOH/TiO_2, FTIR spectra were measured, as demonstrated in Figure 4.3.

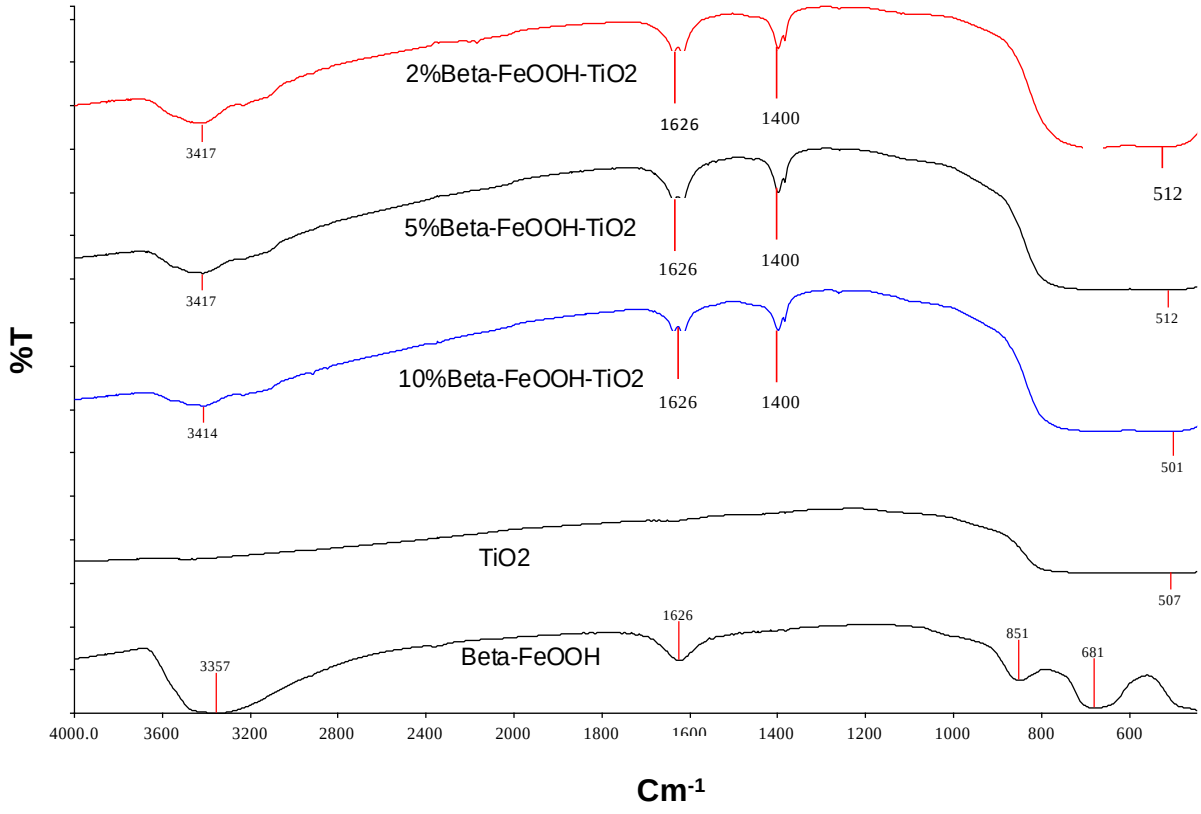

Figure 4.3: FTIR spectra of the β-FeOOH, TiO_2, 10% β-FeOOH/TiO_2, 5% β-FeOOH/TiO_2 and 2% β-FeOOH/TiO_2.

From the FTIR spectra above, the structural differences of β-FeOOH, TiO_2, 10% β-FeOOH/TiO_2 and 5% β-FeOOH/TiO_2 heterojunction were clearly depicted. The absorption peaks at wavenumber ranges of 3357–3417 cm^{-1} and 1400–1626 cm^{-1} were associated with the O-H vibrations of absorbed H_2O molecules, as reported by Wei & Nan (2011) and Xu *et al.*

(2013). Similarly, the absorption peaks of the pure β-FeOOH were in the range of 851 and 681 cm^{-1} and they were associated with a Fe–O vibration mode. Such peaks have been observed by Musić *et al.* (2004) during their investigation into the effect of HCl addition on forced hydrolysis of $FeCl_3$ solution. They also related them to the absorption of Fe–O vibrational modes (Musić *et al.*, 2004). The absorption peak of TiO_2 was detected at a wavenumber corresponding to 507 cm^{-1}. Similar absorbances have been noted by Wang *et al.* (2007) and linked to the stretching vibrations of Ti–O in anatase TiO_2 particles (Wang *et al.*, 2007). It is remarkable to note that the Fe–O vibration modes of β-FeOOH vanish when TiO_2 is introduced (Figure 4.3). This behaviour could be related to the formation of the Fe–O–Ti bond, as explained by Li *et al.* (2009).

Taking all the above into consideration, it is evident that β-FeOOH can disperse itself at the TiO_2 lattice in the β-FeOOH/TiO_2 heterojunction structure. In consequence, the rod-like shape of β-FeOOH nanoparticles disappeared and started to enhance transversal growths, as seen in Figure 4.2c.

4.3 Photocatalytic activity of β-FeOOH/TiO_2 heterojunction structure

4.3.1 The effect of β-FeOOH in the β-FeOOH/TiO_2 heterojunction structure

The photocatalytic performance of synthesised β-FeOOH/TiO_2 heterojunction was evaluated under simulated solar light irradiation. To evaluate the effect of the synthesised catalyst, MO photodegradation kinetics were investigated under different experimental conditions (Appendix A.2). The photodegradation kinetics of 80 mg/L MO concentration in the presence of 0.01 g/L catalyst and 3 mL/L of 30% hydrogen peroxide are presented in Figure 4.4.

As shown in Figure 4.4a (insert), during the treatment of the MO solution, the colour changed from dark orange to colourless. The obtained MO degradation kinetics are different as results of using different catalysts.

It can be seen from Figure 4.4 that MO removal efficiency of 97% was achieved within 60 minutes of treatment using 5% β-FeOOH/TiO_2. Under the same experimental conditions, less than 20% degradation was obtained using β-FeOOH and less than 40% degradation was achieved by using pristine TiO_2 photocatalyst. In addition, it is clear from Figure 4.4 that there was a very slow degradation of less than 10% when MO solution was kept in absence of light and no degradation observed when MO solution was left over time without any treatment.

Evidently, the addition of only 2% β-FeOOH/TiO_2 catalyst increased photocatalytic performance significantly compared to pure β-FeOOH or TiO_2 (Figure 4.4a). An addition of 5% β-FeOOH in the β-FeOOH/TiO_2 heterojunction structure showed to have enhanced photoefficiency compared to the photocatalytic performance of 2% β-FeOOH/TiO_2 heterojunction.

However, no significant improvement was noticed at higher β-FeOOH/TiO_2 content ratios. Figure 4.4a shows that the use of a 10% β-FeOOH/TiO_2 catalyst resulted in a reduction of photoactivity compared to the photocatalytic performance of 2% and 5% β-FeOOH/TiO_2 nanocomposite.

There are two major possibilities at the core of these observed behaviours pertaining to the reduction of photoactivity of β-FeOOH/TiO_2 heterojunction with higher β-FeOOH content.

Firstly, there might be insufficient or non-interacting material at the hetero-interface of β-FeOOH/TiO_2 heterojunction. Secondly, the results may be due to the increase of the recombination sites, which occurs as a result of an increase in β-FeOOH content in the β-FeOOH/TiO_2 nanocomposite.

Similar results were found by Zhang and co-authors, where they reported that a higher ratio of 98% β-FeOOH/TiO_2 produced increased Fe^{3+} ion content, which was acting as recombination sites to trap the photo-induced electrons and holes (M. Zhang *et al.*, 2014). Indeed, the hetero-interface of the combined semiconductors must have a tightly bonded interface for photo-generated electrons to achieve spatial inter-semiconductor transfer.

Thus, a reduced photoactivity of 10% β-FeOOH/TiO_2 was initially expected, due to larger amounts of dispersed non-interacting material. On the other hand, with a lower ratio of 2% β-FeOOH/TiO_2, the available β-FeOOH material is in competition to form a hetero-interface with TiO_2, resulting in decreased photocatalytic efficiencies.

Therefore, it was deduced that recombination sites increased with an increase of β-FeOOH content up to 5% β-FeOOH/TiO_2, giving decreased photocatalytic efficiencies at higher concentrations than 5%. Therefore, 5% β-FeOOH/TiO_2 nanocomposite exhibited the highest level of photocatalytic performance in the degradation of MO dye from its solution. And hence, 5% β-FeOOH/TiO_2 heterojunction was used throughout this study for all other experiments.

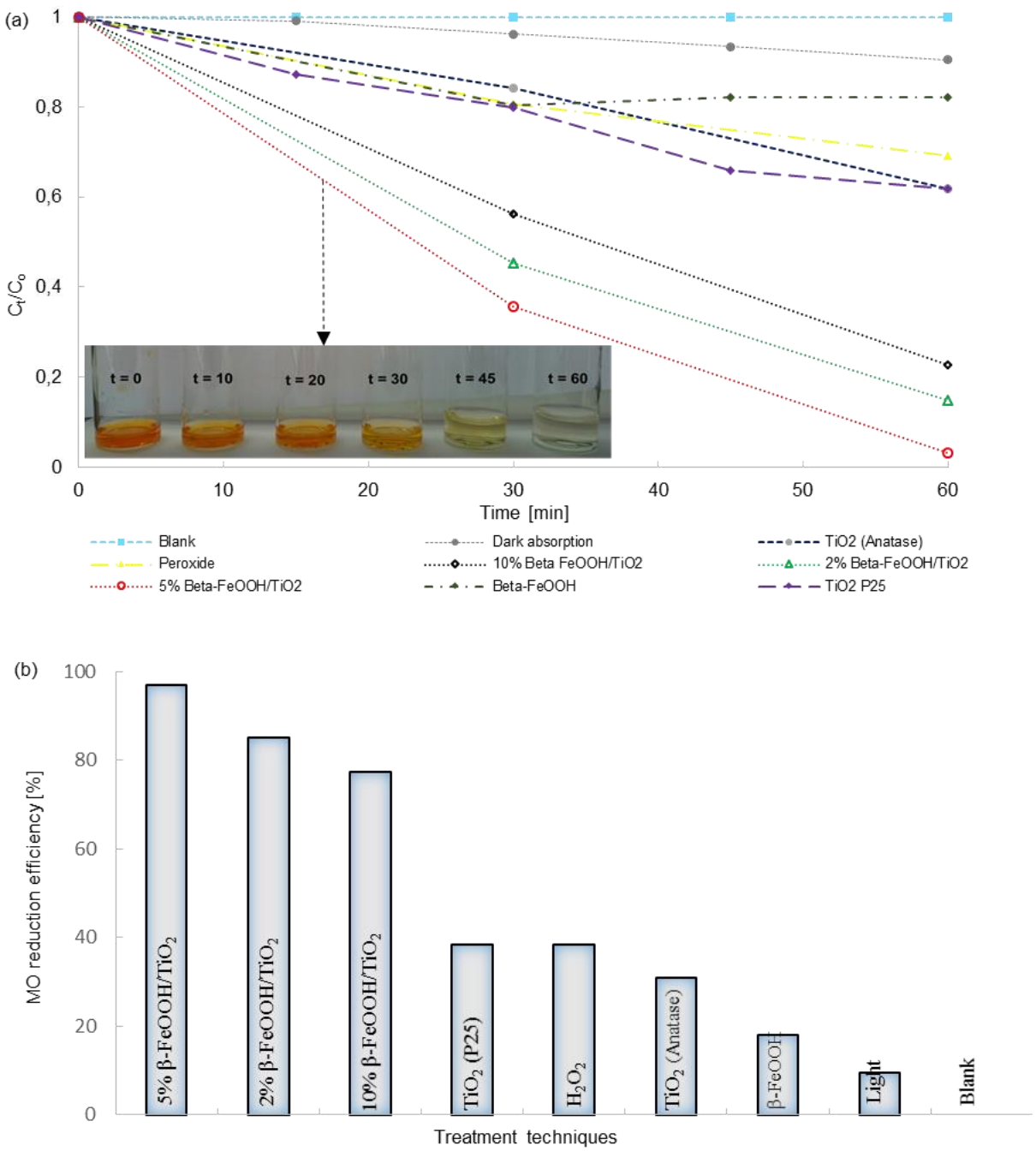

Figure 4.4: (a) Photodegradation of MO in the presence of different catalysts under visible light irradiation and (b) The % colour removal efficiency after 60 minutes of treatment with different catalysts.

From Figure 4.4a, with the blank curve, it is clear that MO does not degrade under photolysis, in the absence of the catalyst and hydrogen peroxide. Thus, MO dye concentration did not change over the study time limits of 60 minutes. This is because organic pollutants have long

and complex aromatic structures with strong bonds which require extra energy (chemical or physical) to break.

When the MO solution with catalyst was kept in the dark with continuous stirring, some of the dyes were degraded or absorbed by the catalyst over time. However, there are adsorption and absorption limits. In this specific study, it can be seen from Figure 4.4b that only 10% of initial MO was degraded or absorbed during the absorption time of 60 minutes. This amount of absorbed dye has been assumed to be negligible compared to 97% degradation or complete MO discolouration, which was achieved after 60 minutes using catalysts and peroxide under simulated solar light irradiation. Shifu and co-authors made the same assumption in their investigation, where the change in concentration of Cr(VI) was assumed to be negligible during the absorption stage (Shifu *et al.*, 2009).

An addition of 3 mL of 30% hydrogen peroxide (H_2O_2) and light without photocatalyst, achieved only 20% degradation within 60 minutes of irradiation time. This decomposition of MO dye with slightly improved degradation results is in line with the results of Behnajady and Daneshvar; in which photo-destruction of acid orange (AO7) and acid red 27 (AR 27) was achieved using a UV/H_2O_2 photocatalysis system (Behnajady *et al.*, 2004 and Daneshvar *et al.*, 2004). They reported that in the photolysis process, the UV light breaks down H_2O_2 into powerful oxidising species, i.e. hydroxyl radicals as was shown in Eq 2.11 (Chapter 2, Section 6.2.3).

It can also be seen from Figure 4.4b, that the pristine TiO_2 (Anatase) and β-FeOOH achieved only 39% and 18% MO degradation efficiency respectively over 60 minutes of irradiation time under identical treatment conditions. Similarly, with anatase, around 40% MO removal efficiency was achieved by the commercially available P25 within 60 minutes of treatment.

Generally, Figure 4.4b shows that prepared 2%, 5% or 10% β-FeOOH/TiO_2 heterojunction structures possess enhanced photoactivity under simulated solar irradiation compare to other available treatment techniques and catalysts reported in this study. Table 4.1 represents the % photoefficiencies for MO colour removal using different catalysts. It is clear from this table that the synthesised 2% β-FeOOH/TiO_2, 5% β-FeOOH/TiO_2 and 10% β-FeOOH/TiO_2 showed enhanced photoefficiency of 85%, 97% and 77% within 60 min of irradiation.

Under identical experimental conditions for the same time of treatment, the MO dye destruction percentage efficiency was 18%, 31%, 38%, 39%, using synthesised β-FeOOH nanorods, hydrogen peroxide, commercially available TiO_2 (P25) and pristine TiO_2 (Anatase).

As shown in Figure 4.5 the reaction rate constant (k-values) for the photocatalytic reduction of MO by different photocatalysts were found to possess pseudo-first-order reaction kinetics. Zhang and co-authors report similar orders of reaction from their results during the reduction of Cr(VI) using a photocatalytic system (M. Zhang *et al.*, 2014). The results obtained in this study (Figure 4.5) show that a faster kinetics rate was given by a 5%β-FeOOH/TiO_2 photocatalyst, which corresponds to 0.058 min^{-1} (Table 4.1).

The rate of reactions for different photocatalysts used in this study are shown in Figure 4.5.

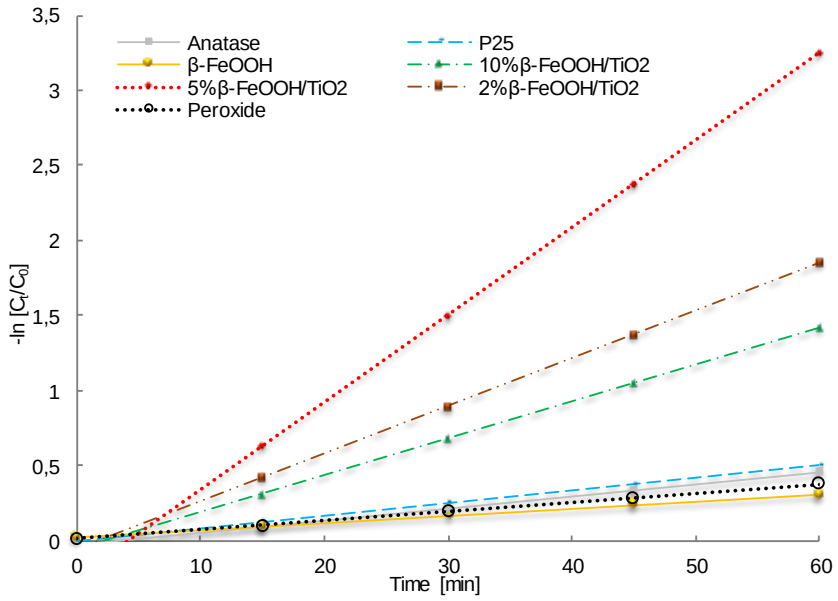

Figure 4.5: Kinetic evaluation of MO degradation using first order fit for different catalysts

The other evaluated photocatalysts, such as synthesised β-FeOOH, H_2O_2, commercially available TiO_2 (P25), pristine TiO_2 (Anatase), synthesised 10% β-FeOOH/TiO_2, and 2% β-FeOOH/TiO_2 heterojunctions have shown decreased rates when compared to the reaction kinetics of 5% β-FeOOH/TiO_2, of 0.0048, 0.0061, 0.008, 0.0083, 0.0246 and 0.0318 min^{-1} respectively. These k-values show that the rate of photocatalytic reaction of β-FeOOH is lower than that of both anatase or Degussa P25 and that the degradation rate of MO using anatase/Degussa P25 is slower than that of β-FeOOH/TiO_2 heterostructures.

Table 4.1: The pseudo-first-order reaction rate constants for MO degradation using different catalysts

Photocatalyst	k (min^{-1})	μ (%)
5% β-FeOOH/TiO_2	0.06	96.94
2% β-FeOOH/TiO_2	0.03	85.14
10% β-FeOOH/TiO_2	0.02	77.20
TiO_2 (Anatase)	0.008	38.30
TiO_2 (P25)	0.008	30.78
H_2O_2	0.006	38.303
β-FeOOH	0.005	17.86

4.3.2 The role of hydrogen peroxide (H_2O_2) in photocatalytic process

The addition of H_2O_2 was important to enhance the performance of the synthesised photocatalyst, since hydrogen peroxide inhibits electron and hole pair recombination in the photocatalytic system as it is an electron acceptor (Eq 2.10). To evaluate the effect of H_2O_2 in the discolouration of an MO solution, the amount of the peroxide added was varied from 0 to 50mL/L of MO solution in the presence and absence of the catalyst. 0.01 g of catalyst was used to degrade 80 mg/L MO dye solution under 300 tungsten lamp.

To evaluate the effect of H_2O_2 only in the absence of a catalyst, controlled experiments were conducted in which the MO solution was degraded by peroxide under a halogen tungsten lamp without catalyst addition (Figure 4.6a). However, the degradation reaction rate is very slow (k-value=0.006 min^{-1}); only 41% degradation efficiency was achieved by the optimum peroxide addition of 30 mL/L and 50 mL/L after one hour of irradiation time (Figure 4.6b). In the presence of a catalyst, it is clear from Figure 4.6b that with the addition of any amount of H_2O_2, degradation of MO occurred at a very slow rate, only 19% in 60 minutes of irradiation time (Figure 4.6b). It can also be seen that the degradation efficiency increases as the amount of peroxide added increases from 5mL to 50 mL H_2O_2/L MO solution.

Similar hydrogen peroxide effects are found in the work of Daneshvar and co-authors. They report that the addition of H_2O_2 generates more hydroxide radicals to attack the aromatic ring structure in organic pollutants, which gives the result of higher photocatalytic efficiency (Daneshvar *et al.*, 2004). In Figure 4.6c, the addition of only 5 mL or 10 mL H_2O_2 per litter of MO solution increased the degradation rate significantly in the presence of a catalyst. However, there was no significant increase in MO degradation efficient between 30 mL or 50mL H_2O_2/L MO solution. It took 60 min for both cases to achieve total decolourisation. There was no surprise in that observation, as it is well known that when H_2O_2 is used in excess, there is a quenching effect, which slows the reaction rate.

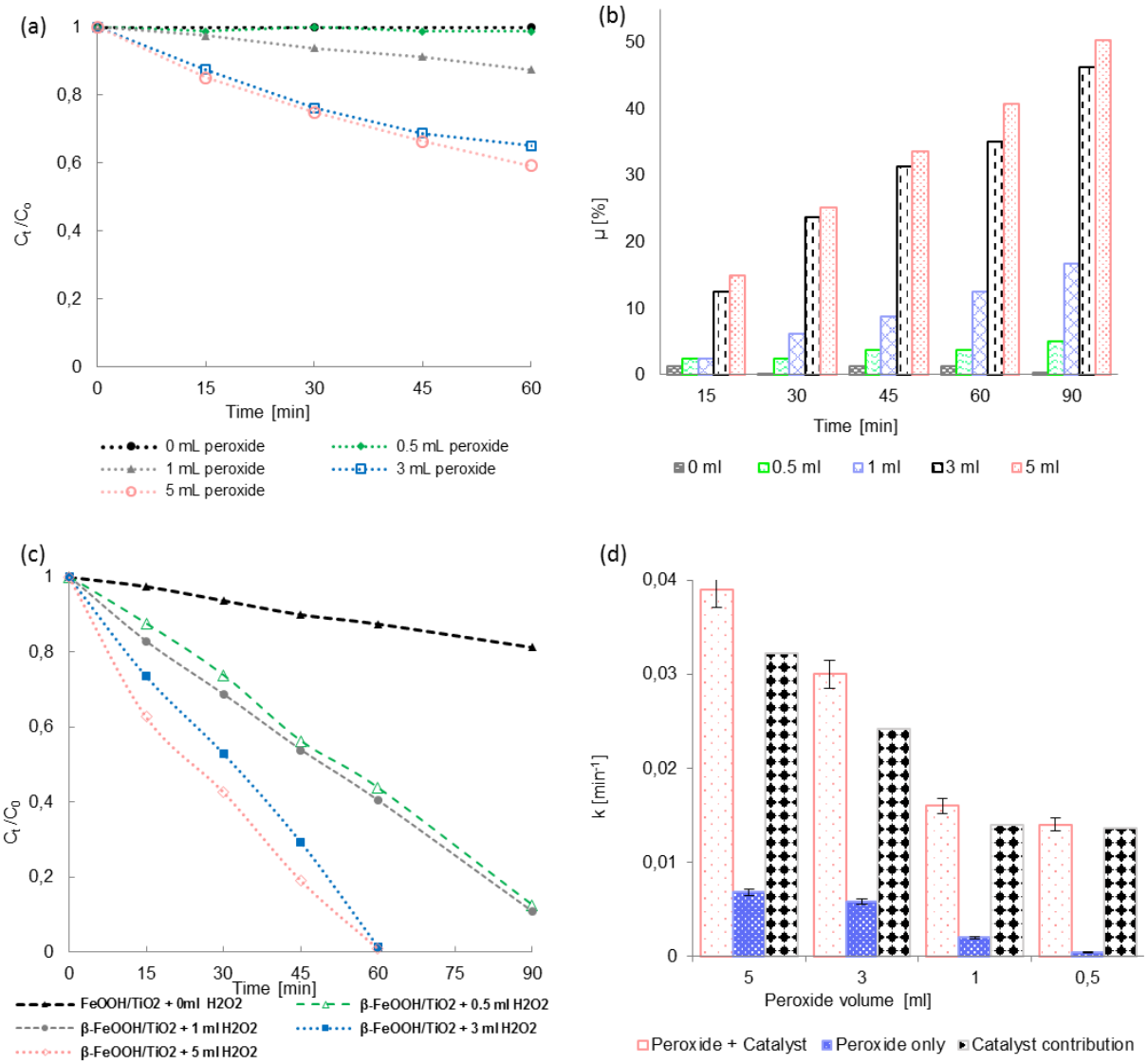

Figure 4.6: (a) The plot of degradation of MO solution by H_2O_2 without the addition of catalyst, (b) The photoefficiency of H_2O_2 only in MO degradation, (c) the graph of H_2O_2 and β-FeOOH/TiO_2 photocatalyst on the degradation of MO solution and (d) The contribution of peroxide or the catalyst during the decomposition of MO using both peroxide and β-FeOOH/TiO_2 photocatalyst.

The reaction rate constant obtained for the combined system (light + catalyst + peroxide) was shown to be a combination of the rate constant for single components, as shown in Table 4.2.

Table 4.2: The MO solution degradation reaction rate constant by H_2O_2 and β-FeOOH/TiO_2 heterojunction photocatalyst.

H_2O_2 (mL)	**H_2O_2 + β-FeOOH/TiO_2 K(min^{-1})**	**H_2O_2 only K(min^{-1})**	**Contribution of β-FeOOH/TiO_2 K(min^{-1})**
5	0.039	0.0068	0.0322
3	0.03	0.0058	0.0242
1	0.016	0.002	0.014
0.5	0.014	0.0004	0.0136

As discussed in the following sections, some reasons were identified as being behind the enhanced photocatalytic efficiency for MO photodegradation in the presence of both catalyst and peroxide. Similar reasons were also reported by previous researchers, such as Ghoreishian *et al.* (2014).

First of all, H_2O_2 is a green electron scavenger in the system; it hinders the e^-/h^+ pair recombination rate in the semiconductor material by accepting conduction band electrons on the surface of the photocatalyst (Eq 2.10). As a result, there is an increased generation of positively-charged valence band holes. These valence band holes react with water to produce powerful photogenerated oxidisers, i.e. hydroxyl radicals (•OH). Consequently, the produced •OH radicals oxidise organic compounds present in the system, resulting in carbon dioxide and water as final products (Eq 2.19).

Secondary, H_2O_2 enhances the photocatalytic activity as it increases the formation of •OH radicals when it reacts with a photogenerated electron in the conduction band (Eq 2.10) after scavenging surface electrons. Finally, ultraviolet light (200 μW cm^{-2}) from halogen tungsten lamps can photo-catalytically split H_2O_2 to initiate •OH radicals via photolysis Eq 2.11.

4.3.3 The effect of operational parameters on the photocatalytic performance

4.3.3.1 Initial dye concentration

To study the effect of initial dye concentration on the discolouration rate of MO, all other reaction parameters were kept constant (Table 3.1) except the MO concentration, which was varied from 25 to 200 mg/L. The effect of initial MO dye concentration on the overall MO degradation reaction rate in the presence of the catalyst is illustrated in Figure 4.7.

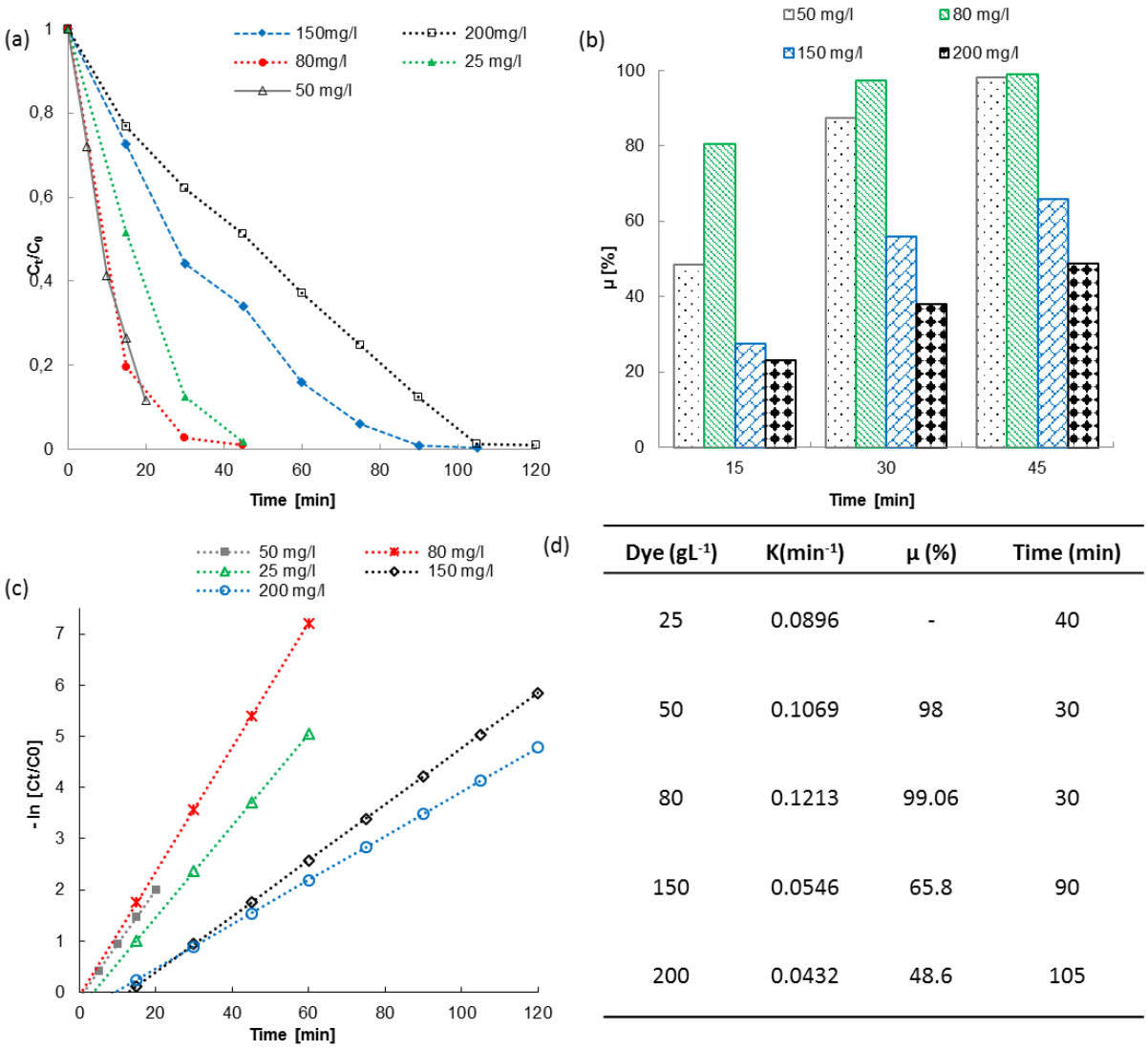

Dye (gL^{-1})	K(min^{-1})	μ (%)	Time (min)
25	0.0896	-	40
50	0.1069	98	30
80	0.1213	99.06	30
150	0.0546	65.8	90
200	0.0432	48.6	105

Figure 4.7: (a) Photodegradation of MO with different initial dye concentration, (b) The effect of initial dye concentration on the % removal efficiency of MO at 60 min (c) The effect of the initial dye concentration on the first order reaction rate and (d) Photodegradation rate constant values and time it took to achieve complete colour removal for different MO initial concentrations.

As illustrated by Figure 4.7, the degradation of highly concentrated dye solutions requires long treatment times. In Figure 4.7a, complete MO colour removal required less than 45 min when the initial dye concentration was 25 mg/L, 50 mg/L and 80 mg/L. It is also clear from Figure 4.7a the degradation of MO dye took much more time as the initial dye concentrations increased to 150 mg/L and 200 mg/L. For the 150 mg/L concentration it took 90 min to achieve complete colour removal and even longer (i.e. 105 min) when it was increased to 200 mg/L.

As illustrated in Figure 4.7c, the reaction rate constant increases with an increase of initial MO dye concentration from 25 mg/L to 80 mg/L. However, there was a poor MO degradation rate constant as the initial MO dye concentration was increased to 150 and 200 mg/L (Figure 4.7b). The reaction rate constant shows that MO degradation rate follows pseudo-first-order reaction kinetics, independent of the initial MO dye concentration. The reaction rate constants (k-values) are given in Figure 4.7c and they show that the decolourisation rate increased from 0.0896 to 0.1213 min^{-1} as the initial dye concentration was increased from 25 mg/L to 80 mg/L. After the 80 mg/L mark, the k-value decreased as initial dye concentration levels were raised, which corresponds to a decrease in degradation rate.

From this observation, it can be suggested that for less than 80 mg/L initial MO dye concentration, the starting dye concentration is not a kinetic rate limiting factor. It can be also deduced that the faster degradation is due to more active catalytic sites available on the surface of the photocatalyst when the MO initial dye concentration is below 80 mg/L.

4.3.3.2 Effect of the light intensity

In this study, the effect of light intensity on the degradation of MO was studied by conducting several degradation experiments with an adjustable light source. The intensity of light was changed by varying the wattage of the halogen tungsten lamp using a voltage regulator (voltage controller) which was adjusted to 150 W, 250 W, and 300 W. The reactor used for all photocatalytic activity evaluation was surrounded by a cooling water system to keep the reaction temperature constant around 63 °C, so that the effect of temperature can be suppressed throughout all experiments. The photosynthetic photon flux density (PPFD) was measured to be 10 000, 9 500, and 4 600 µmol S^{-1} m^{-2} for different voltages of 300, 250 and 150 Watts respectively. The light emitted from the halogen tungsten lamp was mostly in the visible region, with higher PPFD.

Figure 4.8a illustrates that by keeping constant other experimental parameters (Table 3.1), the increase in light intensity results in enhanced photocatalytic activity. It can be seen from Figure 4.8a that with decreasing light intensity, the photodegradation rate of MO decreased significantly. Under the same experimental conditions, the discoloration of MO solution was achieved very faster within 45 min of irradiation using 300 W. The colour of MO solution was not clear within 60 min of irradiation time by lowering the intensity of light from 300 W to 250 W under the same experimental condition. By using 150 W light, there is no significant MO solution colour change within 60 min of irradiation time. It is evident from Figure 4.8b that the highest percentage photocatalytic efficiency (99.08 %) of β-FeOOH/TiO_2 is at 300 W and 250 W achieved a better photoefficiency (92.73 %) of β-FeOOH/TiO_2 than its photoefficiency (73.68 %) at 150 W under similar experimental conditions. This result suggests that the photocatalytic activity of β-FeOOH/TiO_2 composite increases with the light intensity, as it is highly active under visible light. From Figure 4.8c the MO degradation rates decrease as the intensity of light is decreased. The highest kinetic with k-value of 0.12 min^{-1} was achieved when the experiment was carried out under 300 W tungsten lamp irradiation. Lower k-values of 0.06 min^{-1} and 0.01 min^{-1} were achieved using 250 W and 150 W respectively. Figure 4.8b also shows the role of the produced β-FeOOH/TiO_2 heterojunction. Taking example on the photoefficiency of produced β-FeOOH/TiO_2 and P25 under 250 W tungsten lamp irradiation. The figure illustrates the relative ineffectiveness (µ = 34.04 %) of P25 compared to the photodegradation efficiency (µ = 92.73 %) of β-FeOOH/TiO_2 heterojunction under the same experimental conditions.

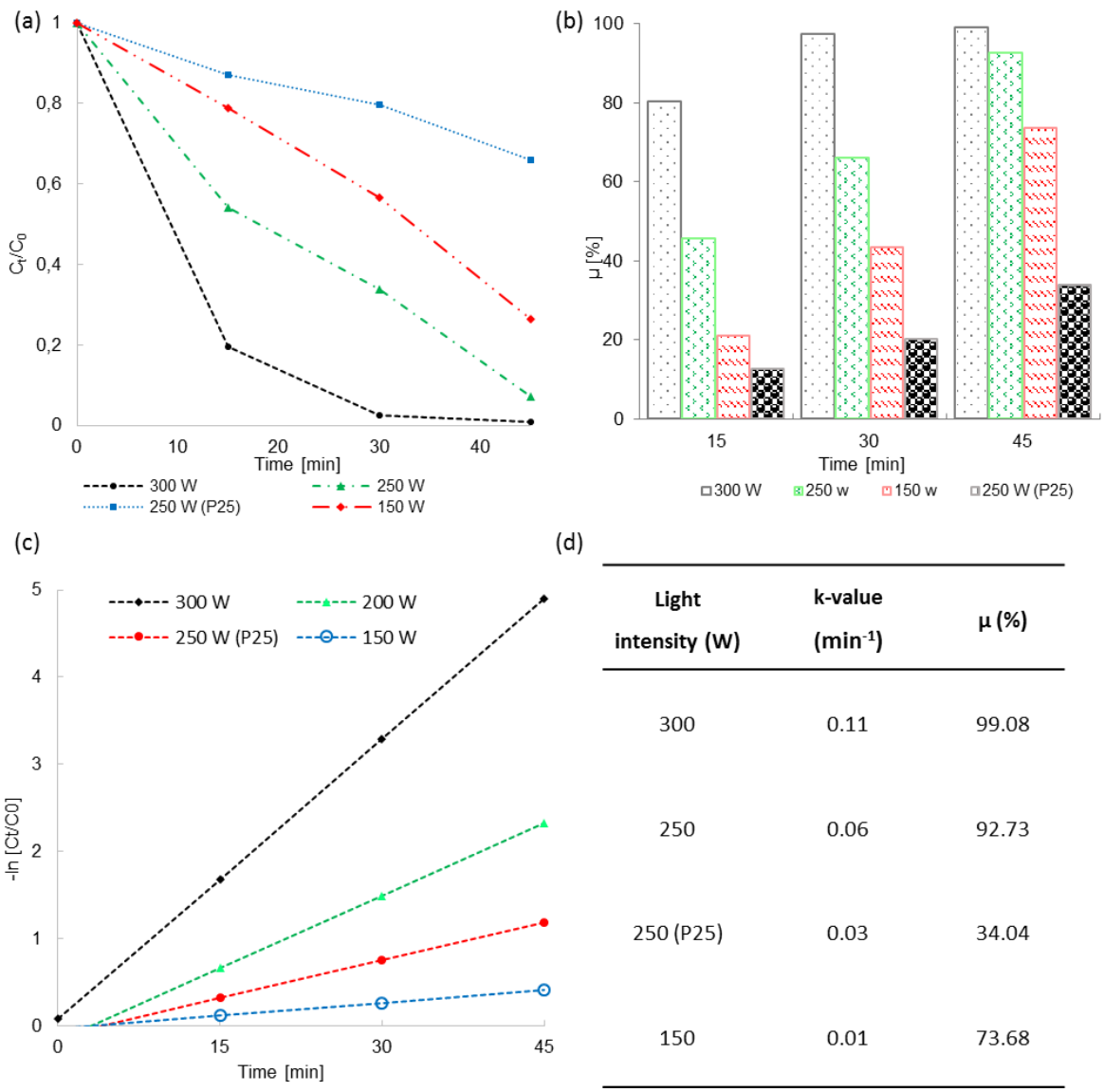

Light intensity (W)	k-value (min^{-1})	μ (%)
300	0.11	99.08
250	0.06	92.73
250 (P25)	0.03	34.04
150	0.01	73.68

Figure 4.8: Effect of the light intensity on the degradation of MO dye solution, (b) The effect of the light intensity on the % removal efficiency of MO and (c) The effect of the light intensity on the reaction rate of MO degradation. (d) Photodegradation rate constant values and time it took to achieve complete colour removal for different MO initial concentrations.

4.3.3.3 Effect of the pH solution

The effect of pH on MO degradation rate by β-FeOOH/TiO_2 heterojunction structures was evaluated by varying the pH of the MO solution in the range of 3 to 7.5. The results presented in Figure 4.9a show that the photocatalytic performance of β-FeOOH/TiO_2 decreases when the pH of the solution is increased. Figure 4.9b shows that at pH 3 nearly complete MO colour removal was achieved within 30 minutes of irradiation time.

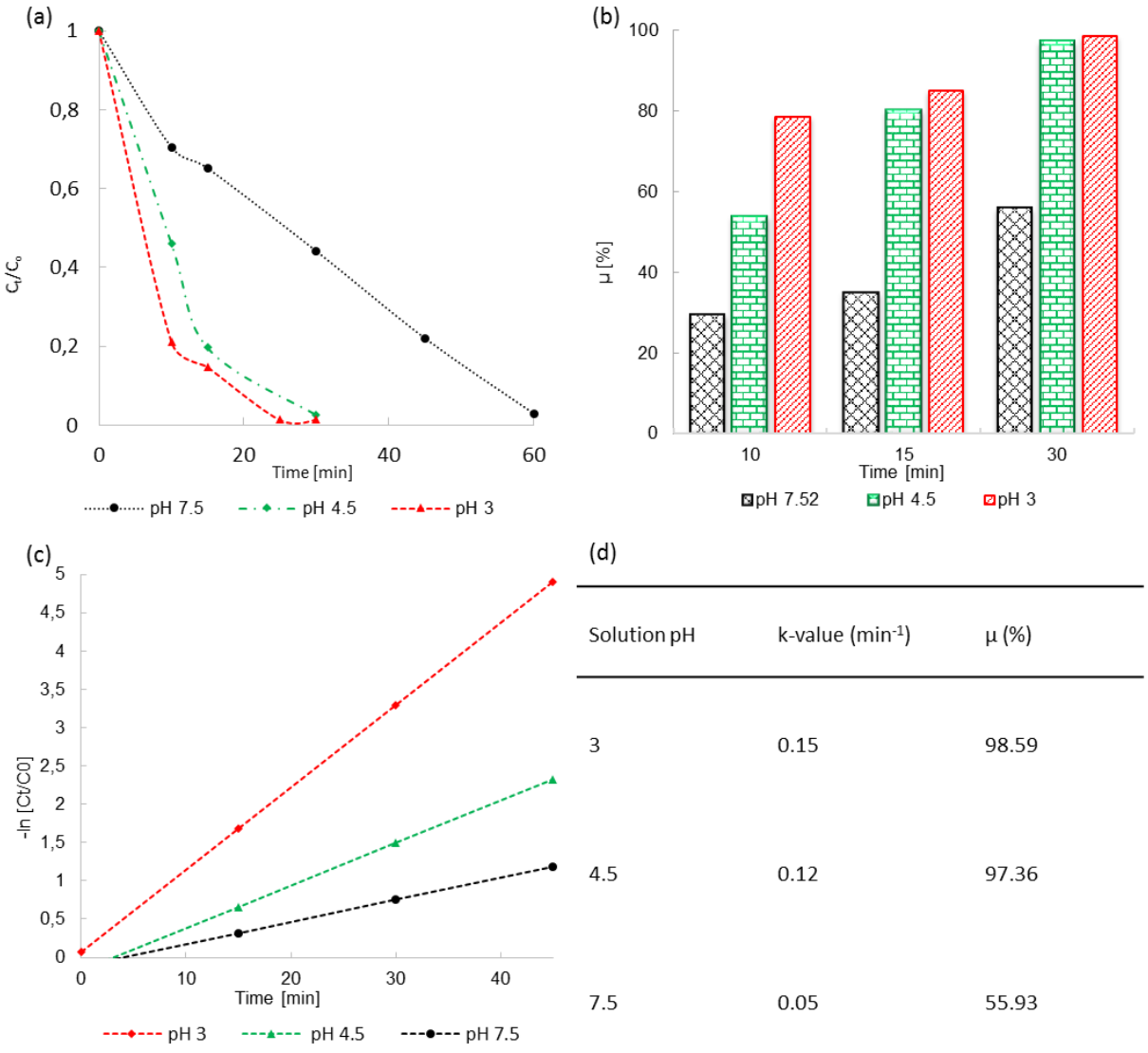

(d)

Solution pH	k-value (min^{-1})	μ (%)
3	0.15	98.59
4.5	0.12	97.36
7.5	0.05	55.93

Figure 4.9: (a) The effect of solution pH on the degradation of MO solution, (b) The effect of solution pH on the % removal efficiency of MO. (c) The effect of solution pH on the reaction rate of MO degradation and (d) The comparison between degradation efficiency of MO with different solution pH.

Figure 4.9b shows that the pH of 7.5 resulted in lower photoefficiency compare to lower pH values. In addition, Figure 4.9b shows that there was no significant difference between the percentage photoefficiency of MO solution at the pH of 4.5 and 3. Hence, the photoactivity of β-FeOOH/TiO_2 is higher in the acidic medium (pH = 4.5) than basic medium when the pH value of the solution is raised even a bit higher to 7.5.

From Figure 4.9c, at pH 3, the MO degradation was enhanced with a k-value of 0.15 min^{-1}, which was found to be higher than the reaction rate constant (k = 0.12 min^{-1}) at pH 4.5. A significant photocatalytic efficient drop was observed in the MO solution at a pH of 7.5. With this pH of 7.5, only 56% degradation with k-value of 0.05 min^{-1} was achieved in 30 minutes of irradiation time, with all other experimental conditions constant.

The drop in the reaction kinetics is attributed to the relationship between solution pH and the redox potential of the photo-generated valence band hole (h^+). As reported by Grätzel (2003) and Hoffmann *et al.* (1995), the redox potential of h^+ decreases by 0.059 V per unit of increased pH (Grätzel, 2003; Hoffmann *et al.*, 1995). The proposed photocatalysis mechanism entails that the oxidation ability of h^+ decreases as solution pH increases, resulting in low levels of photocatalytic efficiency. Similar observations are presented by Xiang *et al.* (2011), who demonstrate that the ionic species such as MO dye adsorb on protonated surfaces of TiO_2 and β-FeOOH surfaces when the solution pH is lower than their isoelectric points, which are 6.25 and 8.8 respectively. Xiang and co-authors also show that this can favour the reaction of positive holes with OH^- on the surface of the catalyst, increasing the photoefficiency of the material (Xiang *et al.*, 2011).

With a solution pH value of 4.5, the degradation reaction took 45 minutes for complete discolouration. This value was used for all experiments, since a pH value of 4.5 was a standard for treating the MO solution without the requirement of additional pH adjustments.

4.3.3.4 The effect of the β-FeOOH/TiO_2 catalyst load

The photocatalyst load was also examined in this study as a factor which influences the photodegradation rate of MO. Catalyst load can affect the number of photo-generated e^-/h^+ pairs and ultimately affect the photoactivity of β-FeOOH/TiO_2.

As illustrated by Figure 4.10a, the photoefficiency of β-FeOOH/TiO_2 was examined, and the difference was depicted for different levels of catalyst loading of 0.05, 0.1 and 0.2 g/L. It was found that the photocatalytic performance increased with increasing catalyst load (Figure

4.10a). The increase in catalyst load from 0.1 to 0.2 g/L brought a significant increase in the photocatalytic performance. As shown by Figure 4.10b, almost complete (99%) degradation of MO solution was achieved within 45 minutes of irradiation time using 0.2 g/L of β-FeOOH/TiO_2, while the degradation efficiency of 99.05 % took 60 minutes of irradiation time using 0.1 g/L under the same conditions. However, there was no significant changed between the photoefficiencies when the catalyst load was increased from 0.05 g/L to 0.1 g/L. In both cases it took 60 min of irradiation time to achieve complete discolouration of MO solution. The degradation efficiency of 98.35 % was achieved within 60 min of irradiation time using 0.05 g/L. Figure 4.10c also shows that the MO photodegradation kinetic is higher for the catalyst load of 0.2 g/L with a k-value of 0.12 min^{-1}. The rates of 0.07 and 0.06 min^{-1} are observed for 0.1 g/L and 0.05 g/L catalyst loading respectively as it can be depicted from Figure 4.10d. Therefore, it can be deduced that by increasing the catalyst load, the available active sites were increased, leading to enhanced photocatalytic efficiency. A 0.2 g/L photocatalyst load showed the highest performance levels and it was used as the optimum catalyst load for process parameter evaluation experiments undertaken in this study.

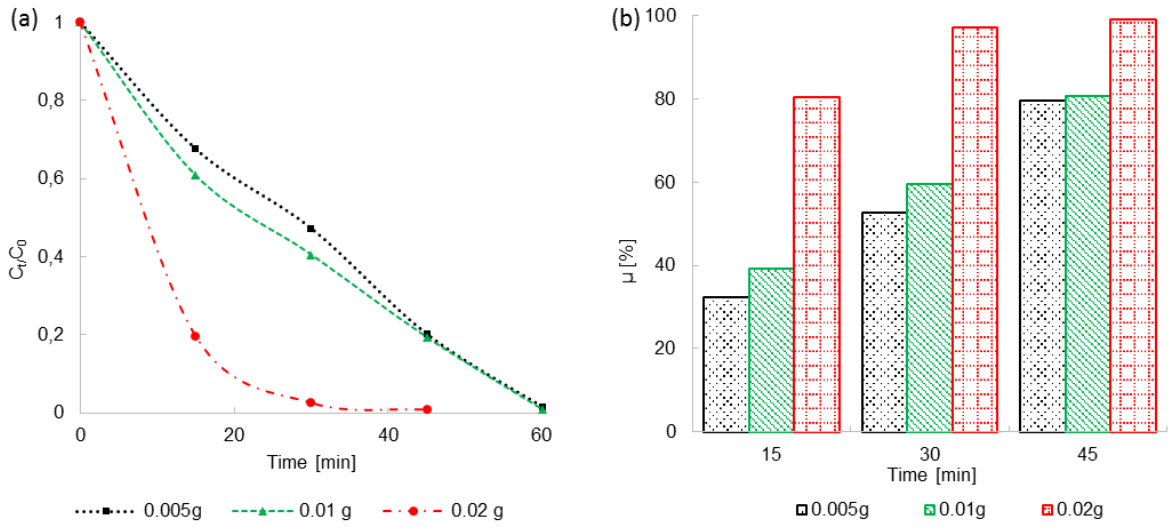

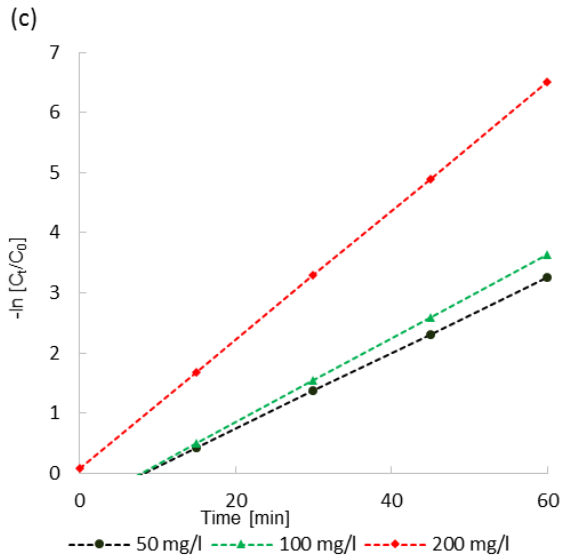

(d)

Catalyst load (mg)	Time (min)	k-value (min^{-1})	μ (%)
50	60	0.06	98.35
100	60	0.07	99.05
200	45	0.11	99.08

Figure 4.10: (a) The effect of β-FeOOH/TiO_2 photocatalyst load on the degradation of MO solution and (b) The effect of catalyst load on MO % removal efficiency at 60 min of irradiation. (c) The effect of catalyst load on the photodegradation reaction rate. And (d) The effect of catalyst load on MO degradation efficiency and values.

4.4 Application of β-FeOOH/TiO_2 heterojunction for the treatment of commercial metal-complex dyes, and wastewater effluent from Falke textile industry

This study also investigated the photocatalytic performance of β-FeOOH/TiO_2 in the degradation of commercial metal-complex dyes namely Synoset Red (SY2R), Synoset Grey (SY2G) and Synoset Yellow (SY2Y) (Figure 4.11).

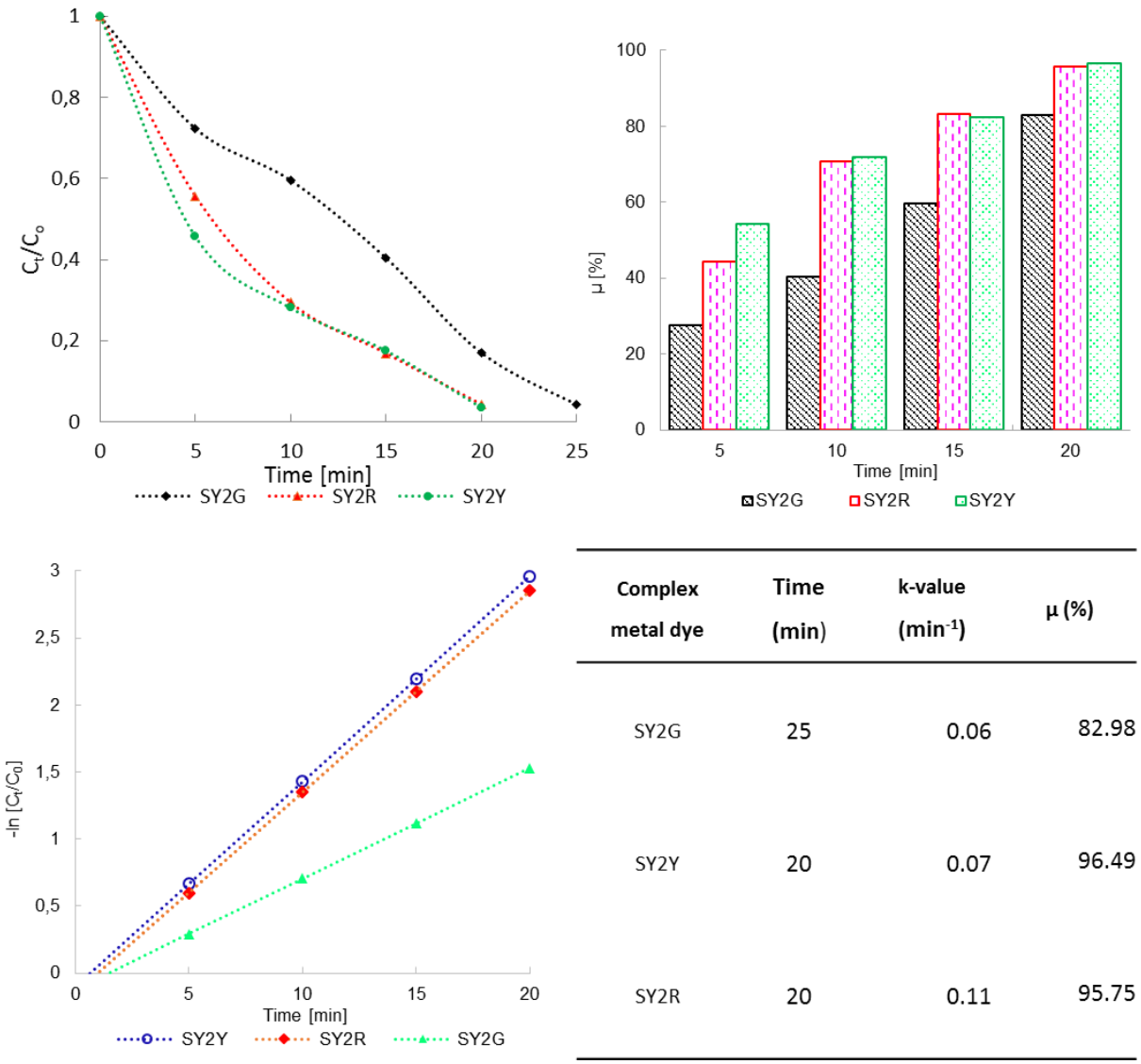

Complex metal dye	Time (min)	k-value (min^{-1})	μ (%)
SY2G	25	0.06	82.98
SY2Y	20	0.07	96.49
SY2R	20	0.11	95.75

Figure 4.11: (a) Degradation of commercial metal-complex dyes (SY2Y, SY2G and SY2R) using β-FeOOH/TiO2 photocatalyst, (b) The photoefficiency of β-FeOOH/TiO2 photocatalyst in removing the colour of the metal-complex dye. (c) First order reaction rate for degradation of SY2Y, SY2R and SY2G and (d) The variation of k-value and MO degradation efficiency for different commercial metal dyes.

Figure 4.11a illustrates the photodegradation kinetics of SY2R, SY2G and SY2Y complex metal dyes. Within 20 minutes of irradiation time, there was 96.49% degradation efficiency for the degradation of SY2Y, 95.75% degradation of SY2R and 82.98% degradation of SY2G (Figure 4.11b). It took 15, 20 and 17 minutes of irradiation time to remove colour completely from SY2Y, SY2G and SY2R respectively. Also, the results in Figure 4.11c show that the degradation of commercial complex dyes followed the first order reaction. In Figure 4.11d the rate of the reaction for the degradation of SY2Y was found to be higher than the rate of SY2R and SY2G, with a k-value of 0.1531 min^{-1}, 0.1502 min^{-1} and 0.0825 min^{-1}. According to the environmental regulations for wastewater discharge into the environment, decolouration is the first step prior to mineralisation of wastewater with dyes.

The real wastewater effluent from the nylon dye bath of Falke Textiles with three dye components was treated under simulated solar light irradiation. At specific irradiation time (t), a sample for analysis was taken out of the reactor and tested three times for different colours. A specific wavelength was set to detect a reading in a range of the corresponding colour, according to the dye concentration to be measured. The wavelength of 444, 586 and 495 nm were used for SY2Y, SY2G and SY2R respectively.

Figure 4.12a illustrates the decolouration of real textile wastewater containing a mixture of SY2Y, SY2G and SY2R using the β-FeOOH/TiO_2 photocatalyst. In all cases, the same UV-vis spectra machine was used to measure the dye content in the solution over irradiation time. The rate of degradation for all commercial dyes in the solution followed the same trends, with a high degradation of colours from the solution. The colour removal efficiency of 91%, 89% and 91 % was achieved within 120 min of irradiation time for SY2R, SY2G and SY2Y respectively. However, the solution was discoloured to the naked eye after 30 minutes of irradiation time, as shown by Figure 4.12d.

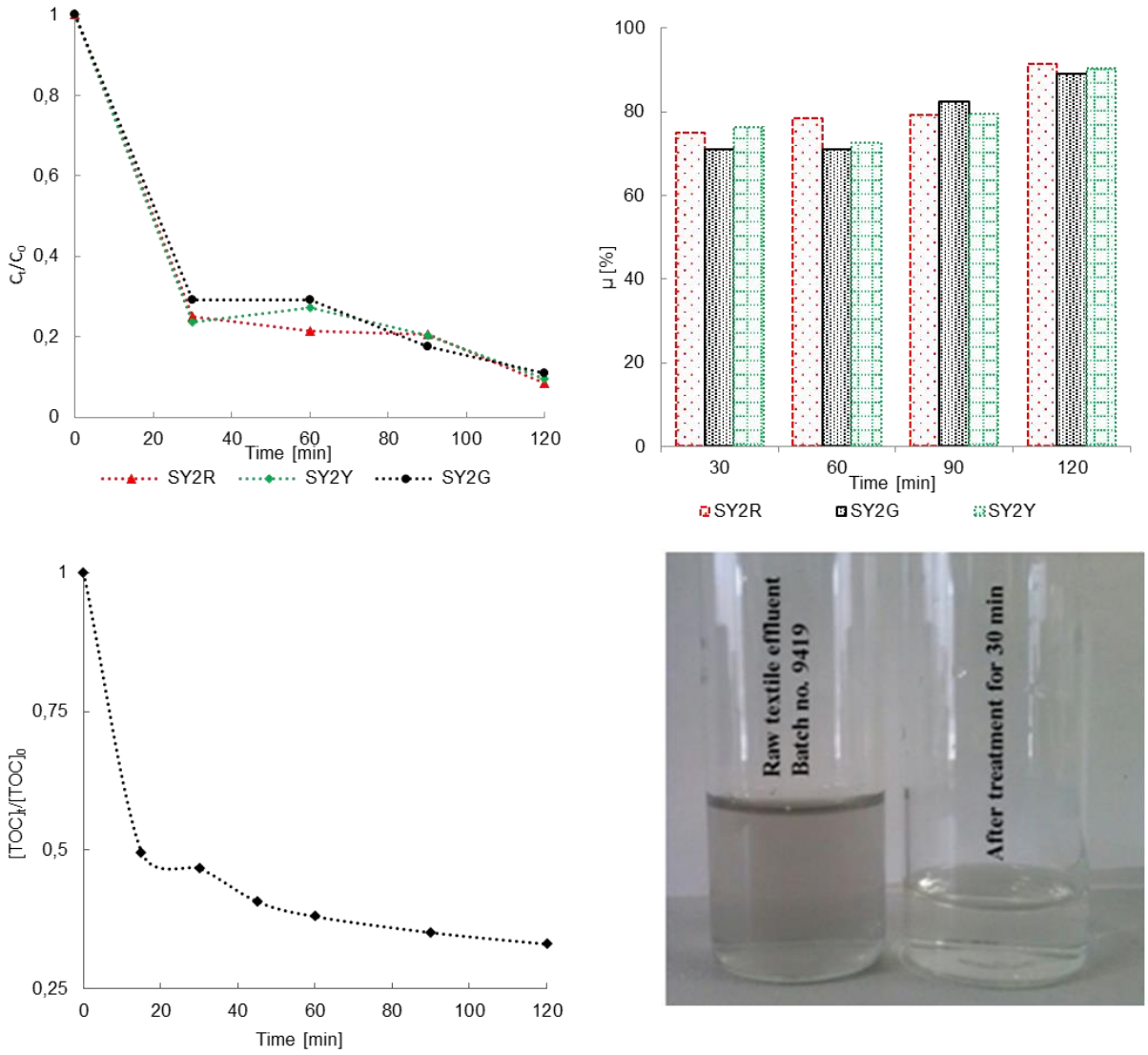

Figure 4.12: (a) Degradation of the real textile wastewater effluent containing Synoset Yellow, Grey and Red commercial metal-complex dyes. (b) Photo-degradation % removal efficiency after 120 min of treatment (c) The decrease of TOC components from real textile wastewater by β-FeOOH/TiO_2 photocatalyst and (d) The colour change from grey to colourless during the photodegradation of grey real textile wastewater.

The total oxygen demand (TOC) value of the textile effluent was analysed before and after the treatment process to evaluate the photodegradation efficiency of β-FeOOH/TiO_2 heterojunction on the mineralisation of textile effluent. The results show that there was a 48.3 mg/L initial TOC value in the raw effluent, which was decreased to 16 mg/L after two hours of irradiation time, which corresponds to 67% TOC removal. This highlights the potential of the developed catalyst in treating industrial wastewater.

After the development and extensive study on the performance of novel ultra-small β-FeOOH/TiO_2 heterojunction structure, further experiments were conducted to evaluate its reusability.

4.5 β-FeOOH/TiO_2 photocatalyst recycling

The recycling of the catalyst is very important for its reusability to save time and for both practical and economical purposes. The as-prepared β-FeOOH/TiO_2 nanocomposite was reused through a very simple process of centrifuging it from the treated water. After centrifugation, the photocatalyst was readily used in another batch of the experiment without any further processing stages of drying or calcination.

Figure 4.13a illustrates that β-FeOOH/TiO_2 photocatalyst has high photocatalytic performance for all recycling stages. The catalyst was recycled up to three times without any significant loss of photocatalytic efficiency, as shown by Figure 4.13b. However, only 91% degradation efficiency was achieved after the fourth cycle, compared to 99% degradation efficiency achieved in the first stage (i.e. before catalyst recycling). This decrease in photocatalytic activity can be attributed to the minor loss (less than 10% of total material) of the material during the centrifugation stage with the samples.

As reported in the literature, when the photocatalyst absorbs light, surface Fe^{3+} get reduced to Fe^{2+} states (Eq 4.1) which are consumed in one of two different ways; either by reacting with H_2O_2 to produce $^{\bullet}OH$ or by suffering dissolution (Eq 4.2).

$$Fe^{3+} + e_{cb}^{-} \rightarrow Fe^{2+} \qquad \text{Eq 4.1}$$

$$Fe^{2+} + H_2O_2 \rightarrow Fe^{3+} + OH^{-} + {}^{\bullet}OH \qquad \text{Eq 4.2}$$

Iron concentration in the solution was measured using atomic absorption spectroscopy (AAS) at the end of the experiment. No iron traces were found in the solution. This suggested that there was no dissolution of Fe^{3+} when the catalyst was irradiated with halogen tungsten lamps during photocatalytic experiments. Hence, the material showed good recycling ability.

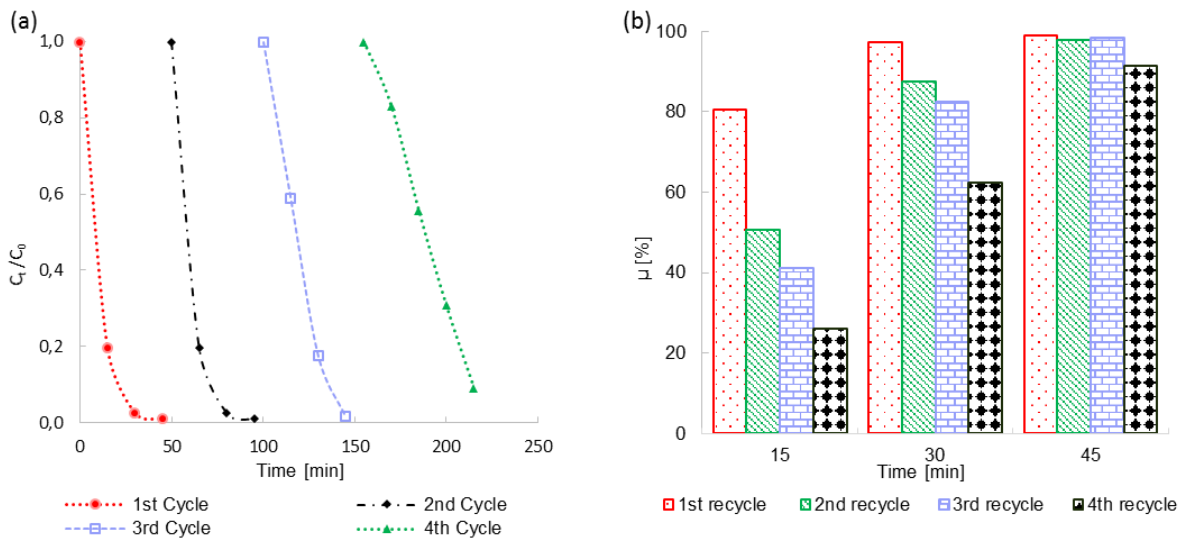

Figure 4.13:(a) The degradation of MO by β-FeOOH/TiO_2 photocatalysts over four recycling stages. (b) Photo-degradation % removal efficiency of four recycling stages.

4.6 Repeatability studies on the photocatalytic activity of β-FeOOH/TiO_2 heterojunction structure

The photoefficiency of the 5% β-FeOOH/TiO_2 nanocomposite was validated by performing repeat experiments for the degradation of methyl orange as a probe dye for this study. Furthermore, repeat experiments were conducted to evaluate the reliability of the catalyst in photodegradation of Acid black dye.

Under similar experimental conditions, the same MO dye concentration was degraded in four different batches. Figure 4.14a illustrates that the complete colour removal of the MO required less than 60 minutes of irradiation time for all four similar runs. Also, it is clear from Figure 4.14a that all of the runs followed the same dye degradation trend over irradiation time. Figure 4.14b shows that there was 40 % of the total dye degradation in the first 15 min of irradiation, more than 60 % efficiency was achieved within 30 min and the highest efficiency of 97% was achieved in 60 min of irradiation time. Furthermore, the error bars illustrated in Figure 4.14b shows the standard deviation of each run from the mean run at any given interval time. The results show that there is no significant deviation between the efficiency of each run and the mean degradation efficiency. Figure 4.14c shows that there is no significant difference between the photodegradation rates (k-values) for different runs and initial run. Moreover, there was no deviation between the percentage degradation efficiency of the initial run and four repeats as it can be observed in Figure 4.14d. The results, depicted in Figure 4.14, show

the evidence for the repeatability of MO degradation by 5% β-FeOOH/TiO_2 heterojunction structure.

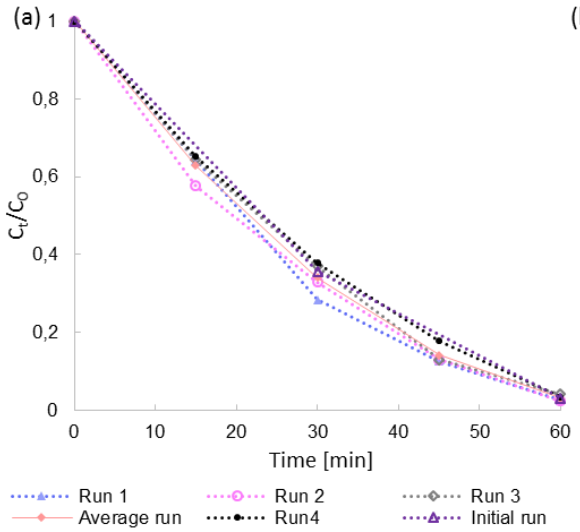

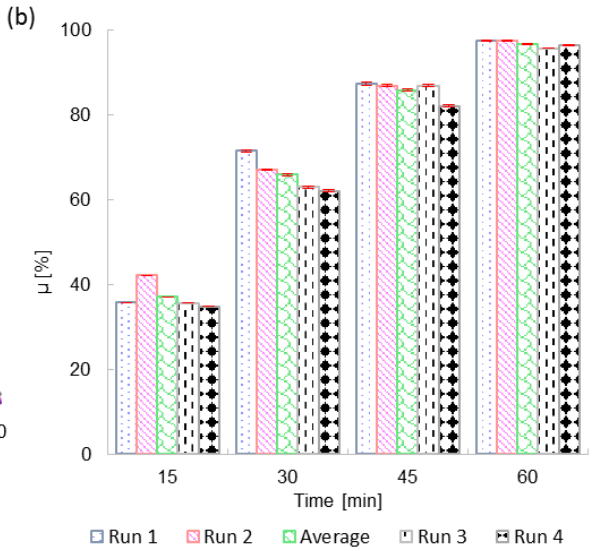

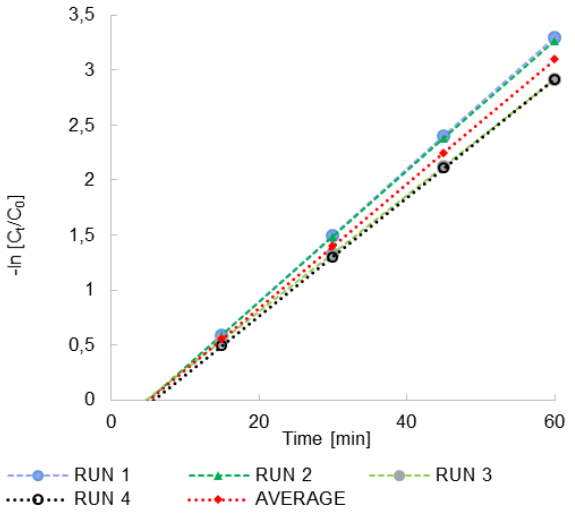

(d)

Run	k-value (min^{-1})	Efficiency (%)	% Error
RUN 1	0.06	97.53	5.76
RUN 2	0.06	97.57	4.53
RUN 3	0.05	95.83	6.89
RUN 4	0.05	96.62	5.48
Initial run	0.06	96.94	2.07

Figure 4.14: (a) The MO photodegradation kinetics for five repeated experiments. (b) The MO % removal efficiency validation (c) The k-values of MO degradation for five different runs. (d) The table of k-values and % efficiency for different runs of MO degradation by 5% β-FeOOH/TiO_2.

Figure 4.15a shows the degradation of acid black for three different runs and their average run under the same conditions (Appendix B.3). The results in Figure 4.15a indicate that there was no significant photodegradation difference in three runs of acid black degradation under similar experimental conditions. The degradation of acid black dye under similar conditions also resulted in identical photoefficiency (Figure 4.15b). More than 90% photoefficiency was achieved for all runs within 60 minutes of irradiation time.

In Figure 4.15c, the photodegradation reaction rate constant (k- values) for all the runs were experimentally determined and there was no significant percentage error between k-values for different runs, as can be observed in Figure 4.15d. Hence, it can be deduced from the results obtained that the photocatalytic activity of 5% β-FeOOH/TiO_2 can be repeated for the degradation of different pollutants to yield identical results.

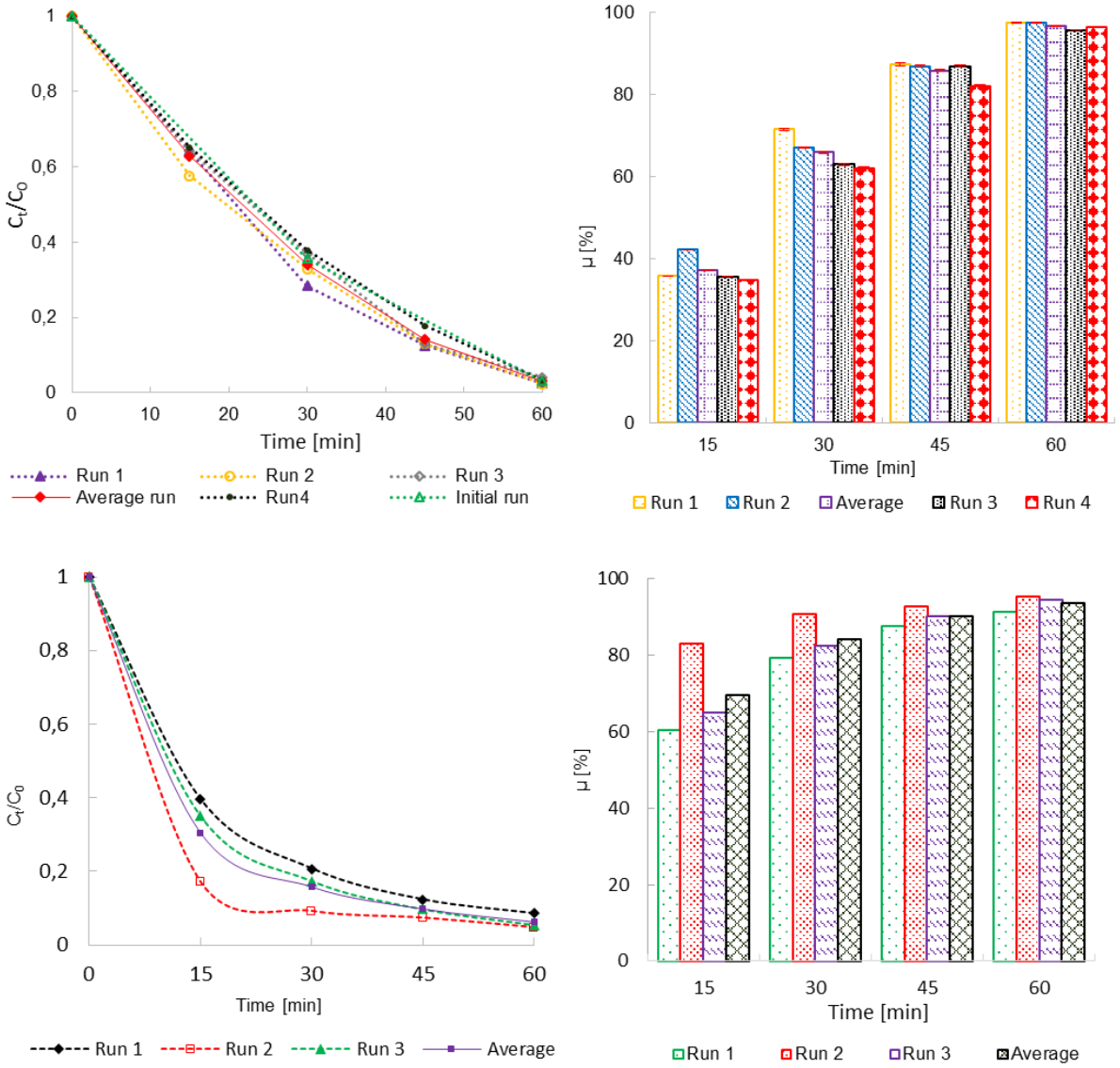

Figure 4.15: (a) The validation of 5% β-FeOOH/TiO_2 photocatalytic efficiency for the degradation of Acid black dye. (b) The % removal efficiency (c) The k-values of acid black degradation for three different runs. (d) The table of k-values and % efficiency for different runs of acid black degradation by 5% β-FeOOH/TiO_2.

4.7 Comparison between the novel synthesised β-FeOOH/TiO_2 heterojunction and previous available visible light photocatalysts

A comparison was carried out between the photocatalytic activity of β-FeOOH/TiO_2 and other visible light photocatalysts reported in the literature for the degradation of organic compounds. Figure 4.16 represents a comparison of photodegradation kinetics of MO by the developed catalyst and other visible light photocatalysts which were reported in the literature to have enhanced photoefficiency as it can be seen from Table 4.3.

It is clear from Figure 4.16 that the newly developed photocatalyst exhibited higher photocatalytic activity than other visible light photocatalysts described in the literature. It is also remarkable that under visible light irradiation, the photocatalyst developed in this study has enhanced photocatalytic performance when compared to the commercially-available nitrogen-doped TiO_2 which is known to be an excellent visible light photocatalyst.

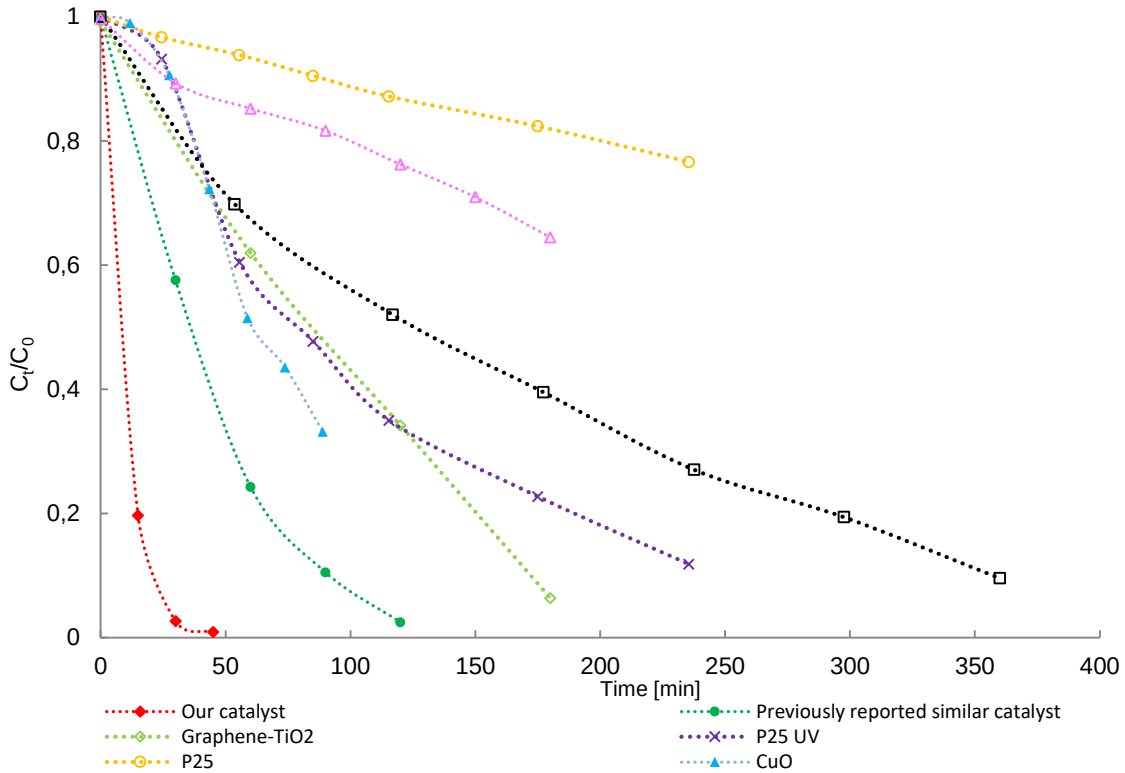

Figure 4.16: The comparison of MO photodegradation kinetics between the developed catalyst in this work and previously published catalysts in available literature.

Table 4.3 shows the comparison of MO photodegradation efficiency between the developed catalyst in this work and previously published catalysts in the available literature. For the first example, the photocatalytic performance of heterojunction was compared with the photoactivity of graphene oxide/TiO_2 composite, Fe^{3+} doped TiO_2 and nitrogen-fluorine codoped TiO_2 nanobelts which were developed by Chen and co-authors. In their work, they reported enhanced photocatalytic performance of graphene oxide/TiO_2 composite in the degradation of MO under visible light irradiation. However, it took more than 180 min to achieve less than half the degradation of the initial MO using their optimum experimental parameters, as illustrated in Table 4.3 (Chen *et al.*, 2010).

Based on the exceptional enhanced photocatalytic performance of 99.08% degradation efficiency for the prepared catalyst, it can be suggested that the developed catalyst has potential industrial applications, particularly in the textile industry for decolouration of real effluent under visible light irradiation. The objective behind this study was to develop a visible light photocatalyst and to evaluate its photoefficiency under simulated solar light irradiation. This objective has arguably been achieved.

Table 4.3: The comparison of MO photodegradation efficiency between the developed catalyst in this work and previously published catalysts in available literature

Photocatalyst	Targeted pollutant	Light	Cataly (mg/L)	Vol (mL)	Conc (mg/L)	Time (min)	μ (%)	Reference
Graphene oxide/TiO_2	MO	1000 W	500	50	12	180	93.6	Chen *et al.*, 2010
F-N co-doped/ TiO_2 nanobelts	MO	500 W	200	100	20	180	35.5	He *et al.*, 2012
Fe^{3+} doped TiO_2	MO	-	200	-	80	360	90.4	Tong *et al.*, 2008
CuO micro-particles	MO	100 W	500	100	3X10 M	89	66.8	Li *et al.*, 2011
Micro sized TiO_2/β-FeOOH	MO	500 W	200	100	80	120	97.5	Zhihui *et al.*, 2013

4.8 Determination of hydroxyl radical (•OH) by photoluminescence (PL) technique

Several studies (Mahmoodi *et al.*, 2006; Daneshvar, Salari & Khataee, 2004) point out that Eq 2.10 and Eq 2.11 are commonly applicable in photocatalysis in the presence of H_2O_2, while Eq 2.16 is only applicable when a positive proton (h^+) is present at the valence band of the semiconductor materials. Within this study, some experiments were conducted to prove Eq 2.16 and the existence of valence band holes at the surface of the composite material.

Coumarin (COU) was used as a fluorescence probe, since it can react with •OH radicals (Eq 4.3) and be converted into high luminescence 7-hydroxycoumarin (7HC) (Xiang *et al.*, 2011). Similarly to the previously-mentioned photocatalytic activity evaluation procedure, the solution was irradiated under identical conditions and 0.02 g photocatalyst was used. The only difference was that this time, the catalyst was dispersed in 0.001 M of COU solution and there was no addition of H_2O_2. This was carried out to eliminate the generation of •OH via photolysis and reduction mechanism.

A 4 mL sample was taken from the reactor at regular intervals and the photoluminescence (PL) spectra were recorded at the wavelength of 456 nm. The PL results obtained (Figure 4.17) show that there was no 7HC peak at the beginning of the experiment. The absence of 7HC in the solution before irradiation and generation of peaks as the irradiation time increases can be associated with the formation of •OH. Hence, it can be suggested that the degradation of MO was caused by •OH. However, they were generated from Eq 2.16 in addition to Eq 2.10 and Eq 2.11.

Enhanced photocatalytic activity is shown in Figure 4.6d for the degradation of MO in presence of both catalyst and peroxide. However, there is a synergistic effect, since ineffective photoefficiency was observed in the absence of catalyst (Figure 4.6a) or peroxide (Figure 4.6b).

$$C_9H_6O_2 + 2^{\bullet}OH \rightarrow C_9H_6O_3 + H_2O \qquad \text{Eq 4.3}$$

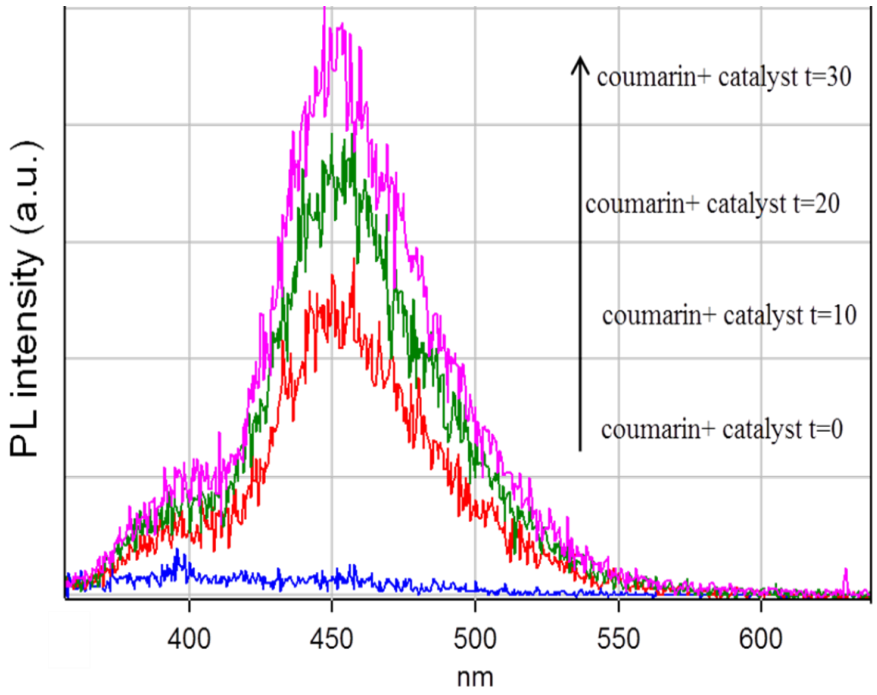

Figure 4.17: Changes observed in PL spectra after irradiation of β-FeOOH/TiO_2 under halogen tungsten lamp.

4.9 Mechanism of β-FeOOH /TiO_2 heterojunction structure

In this study, the β-FeOOH/TiO_2 nanocomposite exhibited enhanced photocatalytic performance when compared with both pristine β-FeOOH and TiO_2 under halogen tungsten lamp irradiation. From these results it can be suggested that matching of relative energy band potentials of the two semiconductors is needed to enhance photoefficiency of a nanocomposite material.

Zhihui and co-authors also reported that introducing a narrower bandgap energy semiconductor into the TiO_2 structure produces a composite photocatalyst with extended spectral response range (Zhihui *et al.*, 2013).

The enhanced photoefficiency showed by β-FeOOH/TiO_2 nanocomposite is primary as a result of the inter-semiconductor charge transfer mechanism at the heterojunction interfaces between β-FeOOH and TiO_2. This inter-semiconductor charge transfer mechanism is possible between these two semiconductors due to the unique energy levels band locations of both materials. The valence band (VB) and conduction band (CB) edge potentials can be calculated empirically using Eq 4.4 and Eq 4.5, as has been reported in literature (Huang *et al.*, 2007; Tang & Ye, 2005).

$$E_{VB} = X - E^e + 0.5E_g \quad \text{Eq 4.4}$$

$$E_{CB} = E_{VB} - E_g \quad \text{Eq 4.5}$$

Where:

E_{VB}: Valence band edge potential

E_{CB} : Conduction band edge potential

X: Electronegativity of the semiconductor, which is the geometric mean of the electronegativity of the constituent atoms.

E^e: The energy of free electrons (~4.5 eV) on the hydrogen scale

E_g : The band gap energy of the semiconductor (Chakraborty & Kebede, 2012; Huang *et al.*, 2007).

Energy band gap of TiO_2 and β-FeOOH materials were calculated by using the equation presented below:

$$E_g = \frac{hC}{\lambda} \quad \text{Eq 4.6}$$

Where:

h: is Planks constant (6.626 X 10^{-34} Js)

c: Speed of light (ms^{-1}) and λ is the cut off wavelength (nm).

The UV–vis diffused spectra was used to obtain the cut-off wavelength of the materials. Figure 4.18 represents UV–vis diffused spectra of pristine β-FeOOH, TiO_2 and β-FeOOH/TiO_2 nanocomposites.

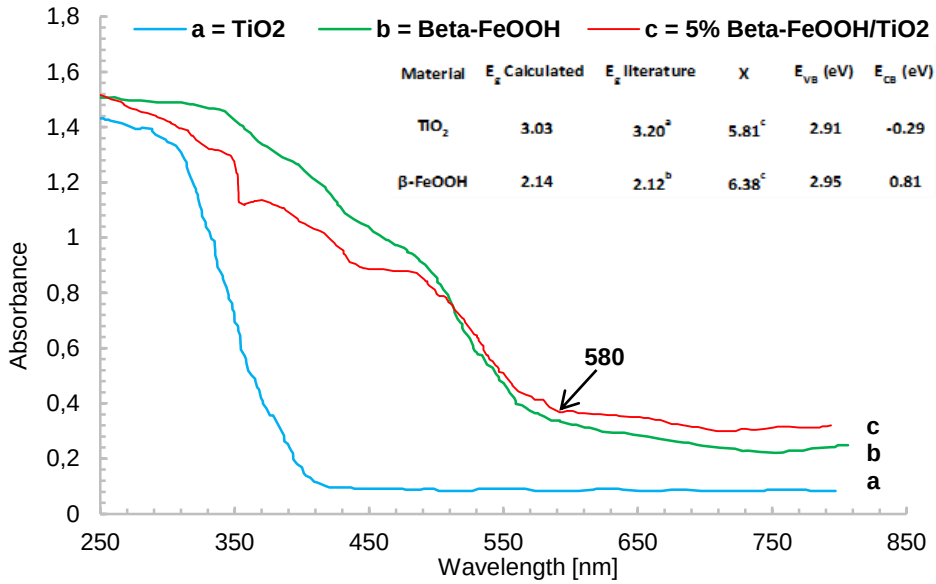

Figure 4.18: UV-Vis diffuse spectra of the different materials, (a) TiO_2 (b) β-FeOOH and (c) 5% β-FeOOH/TiO_2.

It can be seen from Figure 4.18 that the photo-absorption of pure TiO_2 in visible regions is very poor, with a strong cut-off point at 410 nm. Greater photo-absorption in the visible region was found for the pristine β-FeOOH material, with an absorption cut-off point of 580 nm. The 5% β-FeOOH/TiO_2 heterojunction structure was shown to have two different cut-off point in the visible (580 nm) and UV light (350 nm) region.

This result suggests that 5% β-FeOOH/TiO_2 composite material has high photo-absorption in both UV and visible light regions. As shown in Figure 4.18 (inset), the calculated E_{CB} for TiO_2 and β-FeOOH was found to be -0.29 and 0.81 eV respectively, and the calculated corresponding E_{VB} for TiO_2 and β-FeOOH was calculated to be 2.91 and 2.95 eV, respectively.

When β-FeOOH/TiO_2 nanocomposite is irradiated with a halogen tungsten lamp, photons are absorbed by the materials and electrons in the VB of the β-FeOOH and TiO_2 are excited to the CB of the materials. The fact that E_{CB} of TiO_2 is positioned higher than the E_{CB} of β-FeOOH (Figure 4.19), makes the E_{CB} of TiO_2 more active than the E_{CB} of β-FeOOH. Hence, photogenerated electrons on the surface of TiO_2 can be transferred to the β-FeOOH via the heterojunction. This also explains why the role of $O_2^{\bullet-}$ in the degradation of MO is limited, as the CB level of β-FeOOH is considerably lower than the standard hydrogen potential, hence direct electron transfers to oxygen molecules, requiring -0.284 V (vs. NHE), will be difficult (Rawal *et al.*, 2013). Therefore, application of hydrogen peroxide was required to scavenge the conduction band electron to enhance MO degradation efficiency. Similarly, the holes (h^+)

generated at the VB of β-FeOOH are transferred to the VB of TiO_2 due to the different valence band edge potentials between β-FeOOH and TiO_2. Photogenerated holes (h^+) in the VB of TiO_2 can take part in oxidation reactions to generate hydroxyl radicals (•OH) which are non-selective oxidants leading to photodegradation and mineralisation of organic compounds. The presence of valence band holes was also proved by the PL study (section 4.8).

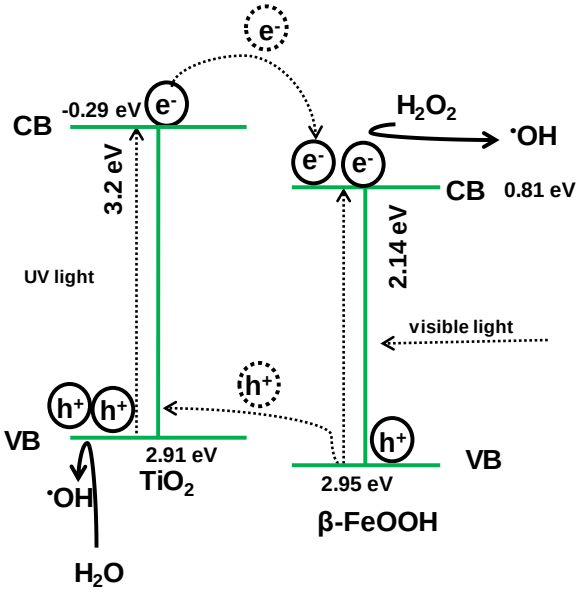

Figure 4.19: Photocatalysis mechanism of FeOOH/TiO_2 heterojunction structure. Potential levels vs NHE are presented.

During this study, the β-FeOOH/TiO_2 photocatalysis mechanism was also verified in a comparative experiment with β-FeOOH/ZnO. To synthesise the β-FeOOH/ZnO heterojunction structure, a ZnO photocatalyst was used instead of TiO_2. Similar calculations were used to get the band edges of ZnO and they have shown to be similar to the band edges of TiO_2. The E_{VB} and E_{CB} of ZnO were calculated to be 2.89 and -0.31 eV respectively. Similar experimental conditions were also used to evaluate the photocatalytic activity of β-FeOOH/ZnO heterojunction. However, surprisingly β-FeOOH/ZnO showed extremely poor photocatalytic performance under the very same halogen tungsten lamp irradiation. This result suggested that there are other factors to consider in the formation of visible light nanocomposite materials besides matching relative energy band potential semiconductors. Huang *et al.* (2007) suggest the following two factors to consider, besides the obvious relative energy band potential matching of the semiconductors. Electron conduction ability is an indispensable requirement for the electron accepting material so that electrons can easily move to the surface of the material. The hole accepting material should also possess fair mobility for the hole transport. In addition, the materials should have good electron and hole conducting ability to produce

enhanced photocatalytic activity. The excellent electron and hole separation in the β-FeOOH/TiO_2 nanocomposite is due to the fact that both materials have open structures. As reported by Huang *et al.* (2007), this is because TiO_2 in the anatase phase has a loosely-packed structure and it is well known that β-FeOOH possesses a tunnel structure.

4.10 Conclusion

Globular-shaped TiO_2 nanoparticles were combined with rod-like β-FeOOH nanoparticles to produce a spherical β-FeOOH/TiO_2 heterojunction structure due to the dispersion of the rod shape of β-FeOOH into the TiO_2 lattice. MO was used as a probe to evaluate the photocatalytic activity of the material as prepared. A 5% β-FeOOH/TiO_2 heterojunction structure showed the highest level of photocatalytic activity. Complete degradation of 80 mg/L MO dye was achieved in a solution of 100 mL with a pH value of 4.5, containing 200 mg/L of β-FeOOH/TiO_2 photocatalyst and 3 mL of hydrogen peroxide under a 300 W halogen tungsten lamp. In the decontamination of real textile wastewater effluent, 67% TOC was removed only after two hours of irradiation time. The regeneration of 5% β-FeOOH/TiO_2 photocatalyst from treated water was made possible simply by centrifuging it from the solution and using it in another batch experiment. In over four recycling stages, the photocatalyst still showed high performance without any significant loss in photoactivity enhancement. The novel photocatalyst showed unique matching energy band potentials which promoted inter-semiconductor e^-/h^+ transfer and inhibited these e^-/h^+ pairs from recombination.

CHAPTER 5. SUMMARY OF RESULTS AND CONCLUSION

5.1 Introduction

The study has presented visible light degradation of textile wastewater using ultra small β-FeOOH/TiO_2 heterojunction structure as a heterogeneous photocatalyst. Numerous authors have reported on the degradation of organic pollutants using TiO_2 photocatalysts (Zaleska, 2008; Chong *et al.*, 2010; Shi *et al.*, 2013; Singh *et al.*, 2013; Zhang *et al.*, 2014). However, it has also been reported that the industrial application of TiO_2 nanoparticles is limited because a TiO_2 semiconductor has a high band gap energy which shows no photo-response under available solar light (Behnajady *et al.*, 2007; Lee & Park, 2013; Wang *et al.*, 2014; Zhang *et al.*, 2014). Therefore, extensive research has been carried out to extend the band gap energy of TiO_2 to the visible light region and different approaches have been applied (Akira Fujishima *et al.*, 2008; Di Valentin & Pacchioni, 2013; Khairy & Zakaria, 2014). Combination of lower band gap semiconductors with TiO_2 has been shown to be a successful technique, with the exception that the available visible light photocatalysts showed poor and ineffective photoefficiency because of charge carriers recombination (Rawal *et al.*, 2009; Huang *et al.*, 2007; Bagwasi *et al.*, 2013; Kaixi *et al.*, 2008; Y. Zhang *et al.*, 2014; C. Liu *et al.*, 2015; Song *et al.*, 2016; Chen *et al.*, 2010; Cong *et al.*, 2012; Wang & Zhou, 2011). Therefore, the objectives of this study were to synthesise an effective visible light photocatalyst with restricted electron and hole pair recombination rate and to evaluate its photoefficiency by the degradation of MO and real textile wastewater effluent. The novel β-FeOOH/TiO_2 heterojunction was synthesised, its structural properties were analysed and its photocatalytic performance was evaluated. Furthermore, there was a detailed study on the major operating parameters and the photocatalyst recycling ability was tested. In addition, the photocatalytic mechanism was derived for the β-FeOOH/TiO_2 heterojunction.

5.2 Summary

The preparation and photoefficiency of β-FeOOH/TiO_2 heterojunction structure was reported in this chapter. A β-FeOOH/TiO_2 visible light photocatalyst was successfully synthesised from ultra-small β-FeOOH doped TiO_2 nanoparticles. The results show that the rod-like structure of β-FeOOH particles disappeared whilst producing the β-FeOOH/TiO_2 heterojunction structure. The produced nanocomposite showed a spherical structure which resembled the circular TiO_2 nanoparticles. The rod-like β-FeOOH nanoparticles dispersed themselves into the TiO_2 lattice

at the heterojunction interface of the combined material. The dispersion process of β-FeOOH nanoparticles prevented their longitudinal growth and favoured transversal growth into the spherical structure during the annealing step.

Different percentage ratios of 2%, 5% and 10 % β-FeOOH/TiO_2 were produced and their photocatalytic activities were evaluated for the degradation of MO. The results showed that all the combination ratios resulted in higher photocatalytic activities compared to the photoactivity of the individual materials i.e., either pristine TiO_2 or ultra-small β-FeOOH. The 5% β-FeOOH/TiO_2 heterojunction showed higher photoefficiency than 2% and 10 % β-FeOOH/TiO_2 under halogen tungsten lamp. The addition of H_2O_2 into the system significantly enhanced the photoefficiency of the β-FeOOH/TiO_2 nanocomposite. This was illustrated by the result obtained whilst using 5% β-FeOOH/TiO_2 and H_2O_2, which showed that complete degradation of MO was achieved within 45 minutes of irradiation, whereas only 30% efficiency of removal was achieved for the same period of irradiation without the addition of H_2O_2.

The different operating parameters, such as initial dye and H_2O_2 concentration, light intensity, solution pH and catalyst load were found to have a significant effect on the β-FeOOH/TiO_2 heterojunction photoefficiency. Optimum value was chosen as 80 mg/L concentration for initial dye and 30 mL/L for H_2O_2 concentration, 300 W light intensity, solution pH of 4.5 and catalyst load of 200 mg/L. A complete colour removal of MO solution was achieved within 45 minutes of irradiation time using β-FeOOH/TiO_2 heterojunction under the abovementioned operating parameters.

The visible light photocatalyst proved to be effective in the degradation of commercial metal-complex dyes. Complete colour removal and 96% degradation of SY2R, SY2Y, and SG was achieved within 25 minutes of irradiation time under a 300W halogen tungsten lamp. The application of the synthesised photocatalyst was also effectively achieved in the treatment of real textile wastewater effluent. Complete colour removal from real textile wastewater effluent was achieved within 30 minutes of irradiation time, using 5% β-FeOOH/TiO_2 heterojunction. Since colour removal is the first step in fulfilling the ultimate objective from an environmental standpoint, the effectiveness of the catalyst to decolourise wastewater demonstrated its viability for such industrial applications. Also, the novel photocatalyst demonstrated powerful effectiveness in the mineralisation of textile wastewater. It was found that 67% of the initial TOC of the wastewater from the nylon bath was removed within two hours of irradiation time.

The recycling of β-FeOOH/TiO_2 was achieved in a straightforward manner by the centrifugation process and there was no leaching of iron in the treated water. The material showed good recycling ability over four cycles without significant loss of its photocatalytic activity, which suggests that the catalyst is very effective from both a practical and economic point of view.

The novel photocatalyst showed enhanced photocatalytic activity compared to other visible light photocatalysts available in the literature (see chapter 4, Table 4.3). For example, the β-FeOOH/TiO_2 heterojunction showed enhanced photocatalytic activity compared to nitrogen-doped TiO_2 which is commercially available and widely known as an excellent visible light photocatalyst. Therefore, the β-FeOOH/TiO_2 photocatalyst can be commercially used for decolourisation of industrial wastewater effluent under visible light irradiation.

There are two particular factors which enhanced the photocatalytic activity of the β-FeOOH/TiO_2 heterojunction structure. The first factor is the unique matching of energy band potentials of the combined photocatalysts. The energy band potential positions promoted inter-semiconductor electron and hole (e^-/h^+) transfer and inhibited photogenerated e^-/h^+ pairs from their recombination. Secondly, heterojunction was made from materials with both good electron and hole conduction ability. i.e. in β-FeOOH/TiO_2 heterojunction, both material structures promoted electron and hole conduction. This is because TiO_2 (anatase) possesses a loosely packed structure and it is well known that β-FeOOH is characterised by a tunnel structure.

5.3 Conclusion

A novel visible light photocatalyst β-FeOOH/TiO_2 heterojunction structure has been successfully synthesised and its photocatalytic activity has been tested. It has an overall spherical structure and showed enhanced photocatalytic performance for the degradation of MO and real textile wastewater effluent.

A 5% β-FeOOH/TiO_2 has excellent photoactivity when compared to β-FeOOH or TiO_2 or other ratios and the addition of H_2O_2 enhanced significantly the photoefficiency of the β-FeOOH/TiO_2 heterojunction. The selected critical experimental parameters are summarised in the following table.

Table 5.1: The selected experimental parameters

Parameter	Optimum conditions
Initial dye concentration	80 mg/L
Photocatalyst load	200 g/L
Intensity of the light	300 W
Hydrogen peroxide concentration	30 mL/L
Solution pH	4.5

Under the selected operating parameters, the complete degradation of MO was achieved within 45 minutes of irradiation. The photocatalyst effectively removed the colour of commercial metal-complex dye and real textile wastewater effluent. It took less than 30 minutes of irradiation time to achieve colourless from dark colours.

Furthermore, the photocatalyst showed that it can be used for industrial applications since it shows reliability in the decolourisation of real wastewater and excellent regeneration capabilities. In addition, β-FeOOH/TiO_2 heterojunction has excellent photoactivity because of the unique matching energy band potentials. Moreover, the excellent photoactivity of β-FeOOH/TiO_2 heterojunction structure was due to the fact that the photocatalyst possesses good e^-/h^+ conduction ability.

5.4 Contributions

This research produced and evaluated an effective TiO_2 visible light photocatalyst with real-world applications in textile wastewater treatment, especially, for the removal of colourants from wastewater effluent of textile industry. Moreover, the study provided information on fundamental critical parameters for the treatment of wastewater in a 100 mL reactor.

The findings of this research work have been published in Materials Research Bulletin Journal: **Chowdhury, M., Ntiribinyange, M., Nyamayaro, K. & Fester, V. 2015. Photocatalytic activities of ultra-small β-FeOOH and TiO_2 heterojunction structure under simulated solar irradiation. *Materials Research Bulletin*, 68(0): 133–141. Doi:10.1016/j.materresbull.2015.03.044**

Best MSc Oral Presentation Award was also awarded to the presentation of the findings of this research work during the 6th International Conference on Nanoscience & Nanotechnology in Africa (NanoAfrica 2016).

Also, the findings of this research work were presented during the 7th International Symposium On Macro-and Supramolecular Architectures and Materials (MAM-14).

5.5 Recommendation for further research

This research focused on the development and photocatalytic performance of the ultra-small β-FeOOH/TiO_2 heterojunction structure under simulated solar irradiation. However, it is clear that the following research work is required:

- Immobilisation of the photocatalyst on a solid substrate
- Scaling up of the photoreactor to a larger volume.
- Toxicity studies of this matrial

REFERENCES

Aazam, E.S. 2016. Enhancement of the photocatalytic activity of europium(III) oxide by the deposition of gold for the removal of atrazine. *Journal of Alloys and Compounds*, 672: 344–349.

Affam, A.C. & Chaudhuri, M. 2013. Degradation of pesticides chlorpyrifos, cypermethrin and chlorothalonil in aqueous solution by TiO_2 photocatalysis. *Journal of Environmental Management*, 130: 160–165.

Ahmad, R., Mohsin, M., Ahmad, T. & Sardar, M. 2015. Alpha amylase assisted synthesis of TiO_2 nanoparticles: structural characterization and application as antibacterial agents. *Journal of Hazardous Materials*, 283: 171–177.

Ahmadi, N., Nemati, A. & Solati-Hashjin, M. 2014. Synthesis and characterization of co-doped TiO_2 thin films on glass-ceramic. *Materials Science in Semiconductor Processing*, 26(1): 41–48.

Ahmed, S., Rasul, M.G., Brown, R. & Hashib, M.A. 2011. Influence of parameters on the heterogeneous photocatalytic degradation of pesticides and phenolic contaminants in wastewater: a short review. *Journal of Environmental Management*, 92(3): 311–330.

Ajmal, A., Majeed, I., Malik, R.N., Iqbal, M., Nadeem, M.A., Hussain, I., Yousaf, S., Zeshan, Mustafa, G., Zafar, M.I. & Nadeem, M.A. 2016. Photocatalytic degradation of textile dyes on Cu_2O-CuO/TiO_2 anatase powders. *Journal of Environmental Chemical Engineering*, 4(2): 2138–2146.

Akhlaghian, F. & Sohrabi, S. 2015. Fe/TiO_2 catalyst for photodegradation of phenol in water. *International Journal of Engineering*, *IJE Transactions A: Basics*, 28(4): 499–506.

Akpan, U.G. & Hameed, B.H. 2009. Parameters affecting the photocatalytic degradation of dyes using TiO_2-based photocatalysts: a review. *Journal of Hazardous Materials*, 170(2–3): 520–529.

Amine, K., Yasuda, H. & Yamachi, M. 1999. β-FeOOH, a new positive electrode material for lithium secondary batteries. *Journal of Power Sources*, 81–82: 221–223.

Asghar, A., Abdul Raman, A.A. & Daud, W.M.A.W. 2015. Advanced oxidation processes for *in-situ* production of hydrogen peroxide/hydroxyl radical for textile wastewater treatment: a review. *Journal of Cleaner Production*, 87: 826–838.

Bagwasi, S., Tian, B., Zhang, J. & Nasir, M. 2013. Synthesis, characterization and application of bismuth and boron Co-doped TiO_2: a visible light active photocatalyst. *Chemical Engineering Journal*, 217: 108–118.

Bakardjieva, S., Stengl, V., Szatmary, L., Subrt, J., Lukac, J., Murafa, N., Niznansky, D., Cizek, K., Jirkovsky, J. & Petrova, N. 2006. Transformation of brookite-type TiO_2 nanocrystals to rutile: correlation between microstructure and photoactivity. *Journal of Materials Chemistry*, 16(18): 1709–1716.

Behnajady, M.A., Modirshahla, N. & Shokri, M. 2004. Photodestruction of Acid Orange 7 (AO7) in aqueous solutions by UV/H_2O_2: influence of operational parameters. *Chemosphere*, 55(1): 129–134.

Behnajady, M.A., Modirshahla, N., Daneshvar, N. & Rabbani, M. 2007. Photocatalytic degradation of an azo dye in a tubular continuous-flow photoreactor with immobilized TiO_2 on glass plates. *Chemical Engineering Journal*, 127(1–3): 167–176.

Benkö, G., Skårman, B., Wallenberg, R., Hagfeldt, A., Sundström, V. & Yartsev, A.P. 2003. Particle size and crystallinity dependent electron injection in fluorescein 27-sensitized TiO_2 films. *The Journal of Physical Chemistry B*, 107(6): 1370–1375.

Bessekhouad, Y., Robert, D. & Weber, J.V. 2004. Bi_2S_3/TiO_2 and CdS/TiO_2 heterojunctions as an available configuration for photocatalytic degradation of organic pollutant. *Journal of Photochemistry and Photobiology A: Chemistry*, 163(3): 569–580.

Bessekhouad, Y., Robert, D. & Weber, J.V. 2005. Photocatalytic activity of Cu_2O/TiO_2, Bi_2O_3/TiO_2 and $ZnMn_2O_4/TiO_2$ heterojunctions. *Catalysis Today*, 101(3–4): 315–321.

Boukhennoufa, A., Bouhelassa, M. & Zoulalian, A. 2011. Photocatalytic degradation of Solophenyl red 3 BL in an aqueous suspension of titanium dioxide. *Journal of Advanced Chemical Engineering*, 1: 1–8.

Carp, O., Huisman, C.L. & Reller, A. 2004. Photoinduced reactivity of titanium dioxide. *Progress in Solid State Chemistry*, 32(1–2): 33–177.

Chakraborty, A.K. & Kebede, M.A. 2012. Preparation and characterization of WO_3/Bi_3O_4Cl nanocomposite and its photocatalytic behavior under visible light irradiation.

Chatzisymeon, E., Petrou, C. & Mantzavinos, D. 2013. Photocatalytic treatment of textile dye house effluents with simulated and natural solar light. *Global NEST Journal*, 15(1): 21–28.

Chen, C., Cai, W., Long, M., Zhou, B., Wu, Y., Wu, D. & Feng, Y. 2010. Synthesis of visible-light responsive graphene oxide/TiO_2 composites with p/n heterojunction. *ACS Nano*, 4(11): 6425–6432.

Chen, M., Jiang, J., Zhou, X. & & Diao, G. 2008. Preparation of akaganeite nanorods and their transformation to sphere shape hematite. *Journal of Nanoscience and Nanotechnology*, 8(8): 3942–3948.

Chong, M.N., Cho, Y.J., Poh, P.E. & Jin, B. 2015. Evaluation of Titanium dioxide photocatalytic technology for the treatment of reactive Black 5 dye in synthetic and real greywater effluents. *Journal of Cleaner Production*, 89(0): 196–202.

Chong, M.N., Jin, B., Chow, C.W.K. & Saint, C. 2010. Recent developments in photocatalytic water treatment technology: a review. *Water Research*, 44(10): 2997–3027.

Chong, M.N., Lei, S., Jin, B., Saint, C. & Chow, C.W.K. 2009. Optimisation of an annular photoreactor process for degradation of Congo Red using a newly synthesized titania impregnated kaolinite nano-photocatalyst. *Separation and Purification Technology*, 67(3): 355–363.

Chowdhury, M., Fester, V. & Kale, G. 2014. Growth kinetics evaluation of hydrothermally synthesized β-FeOOH nanorods. *Journal of Crystal Growth*, 387: 57–65.

Chowdhury, M.R. 2014. Solvent dependent growth of one-dimensional crystalline β-FeOOH nanorods. Unpublished DTech: Chemical Engineering thesis, Cape Peninsula University of Technology, Cape Town, South Africa.

Cong, Y., Li, Z., Zhang, Y., Wang, Q. & Xu, Q. 2012. Synthesis of α-Fe_2O_3/TiO_2 nanotube arrays for photoelectro-Fenton degradation of phenol. *Chemical Engineering Journal*, 191: 356–363.

Da Dalt, S., Alves, A.K. & Bergmann, C.P. 2013. Photocatalytic degradation of methyl orange dye in water solutions in the presence of MWCNT/TiO_2 composites. *Materials Research Bulletin*, 48(5): 1845–1850.

Daneshvar, N., Rabbani, M., Modirshahla, N. & Behnajady, M.A. 2004. Critical effect of hydrogen peroxide concentration in photochemical oxidative degradation of C.I. Acid Red 27 (AR27). *Chemosphere*, 56(10): 895–900.

Daneshvar, N., Rabbani, M., Modirshahla, N. & Behnajady, M.A. 2005. Photooxidative degradation of Acid Red 27 in a tubular continuous-flow photoreactor: influence of operational parameters and mineralization products. *Journal of Hazardous Materials*, 118(1–3): 155–160.

Daneshvar, N., Salari, D. & Khataee, A. 2004. Photocatalytic degradation of azo dye acid red 14 in water on ZnO as an alternative catalyst to TiO_2. *Journal of Photochemistry and Photobiology A: Chemistry*, 162(2–3): 317–322.

Deng, F., Li, Y., Luo, X., Yang, L. & Tu, X. 2012. Preparation of conductive polypyrrole/TiO_2 nanocomposite via surface molecular imprinting technique and its photocatalytic activity under simulated solar light irradiation. *Colloids and Surfaces A: Physicochemical and Engineering Aspects*, 395: 183–189.

Di Paola, A., García-López, E., Marcì, G. & Palmisano, L. 2012. A survey of photocatalytic materials for environmental remediation. *Journal of Hazardous Materials*, 211–212: 3–29.

Dolat, D., Mozia, S., Wróbel, R.J., Moszyński, D., Ohtani, B., Guskos, N. & Morawski, A.W. 2015. Nitrogen-doped, metal-modified rutile titanium dioxide as photocatalysts for water remediation. *Applied Catalysis B: Environmental*, 162: 310–318.

Ellouze, E., Tahri, N. & Amar, R.B. 2012. Enhancement of textile wastewater treatment process using nanofiltration. *Desalination*, 286: 16–23.

Faria, M.C.S., Rosemberg, R.S., Bomfeti, C.A., Monteiro, D.S., Barbosa, F., Oliveira, L.C.A., Rodriguez, M., Pereira, M.C. & Rodrigues, J.L. 2014. Arsenic removal from contaminated water by ultrafine δ-FeOOH adsorbents. *Chemical Engineering Journal*, 237: 47–54.

Fernández-Ibáñez, P., Polo-López, M.I., Malato, S., Wadhwa, S., Hamilton, J.W.J., Dunlop, P.S.M., D'Sa, R., Magee, E., O'Shea, K., Dionysiou, D.D. & Byrne, J.A. 2015. Solar

photocatalytic disinfection of water using titanium dioxide graphene composites. *Chemical Engineering Journal*, 261: 36–44.

Folli, A., Pade, C., Hansen, T.B., De Marco, T. & Macphee, D.E. 2012. TiO_2 photocatalysis in cementitious systems: insights into self-cleaning and depollution chemistry. *Cement and Concrete Research*, 42(3): 539–548.

Fresno, F., Portela, R., Suárez, S. & Coronado, J.M. 2014. Photocatalytic materials: recent achievements and near future trends. *Journal of Materials Chemistry A*, 2(9): 2863–2884.

Fujishima, A., Rao, T.N. & Tryk, D.A. 2000. Titanium dioxide photocatalysis. *Journal of Photochemistry and Photobiology C: Photochemistry Reviews*, 1(1): 1–21.

Fujishima, A., Zhang, X. & Tryk, D. 2008. TiO_2 photocatalysis and related surface phenomena. *Surface Science Reports*, 63(12): 515–582.

Gaya, U.I. & Abdullah, A.H. 2008. Heterogeneous photocatalytic degradation of organic contaminants over titanium dioxide: A review of fundamentals, progress and problems. *Journal of Photochemistry and Photobiology C: Photochemistry Reviews*, 9(1): 1–12.

Ghorai, T.K., Chakraborty, M. & Pramanik, P. 2011. Photocatalytic performance of nano-photocatalyst from TiO_2 and Fe_2O_3 by mechanochemical synthesis. *Journal of Alloys and Compounds*, 509(32): 8158–8164.

Ghoreishian, S.M., Badii, K., Norouzi, M., Rashidi, A., Montazer, M., Sadeghi, M. & Vafaee, M. 2014. Decolorization and mineralization of an azo reactive dye using loaded nano-photocatalysts on spacer fabric: kinetic study and operational factors. *Journal of the Taiwan Institute of Chemical Engineers*, 45(5): 2436–2446.

González Sánchez, O.M., Araña, J., González Díaz, O., Herrera Melián, J.A., Doña Rodríguez, J.M. & Pérez Peña, J. 2014. Detoxification of the herbicide propanil by means of Fenton process and TiO_2-photocatalysis. *Journal of Photochemistry and Photobiology A: Chemistry*, 291: 34–43.

Grätzel, M. 2003. Dye-sensitized solar cells. *Journal of Photochemistry and Photobiology C: Photochemistry Reviews*, 4(2): 145–153.

Gupta, K.S.V., Zhang, J., Marotta, G., Reddy, M.A., Singh, S.P., Islam, A., Han, L., De Angelis, F., Chandrasekharam, M. & Pastore, M. 2015. Effect of the anchoring group in the performance of carbazole-phenothiazine dyads for dye-sensitized solar cells. *Dyes and Pigments*, 113: 536–545.

Gupta, S.M. & Triphati, M. 2011. A review of TiO_2 nanoparticles. *Chinese Science Bulletin*, 56(16): 1639–1657.

Han, F., Kambala, V.S.R., Srinivasan, M., Rajarathnam, D. & Naidu, R. 2009. Tailored titanium dioxide photocatalysts for the degradation of organic dyes in wastewater treatment: a review. *Applied Catalysis A: General*, 359(1–2): 25–40.

Henderson, M.A. 2011. A surface science perspective on photocatalysis. *Surface Science Reports*, 66: 185–297.

He, Z., Que, W., Chen, J., Yin, X., He, Y. & Ren, J. 2012. Photocatalytic degradation of methyl orange over nitrogen–fluorine codoped TiO_2 nanobelts prepared by solvothermal synthesis. *ACS Applied Materials & Interfaces*, 4(12): 6816–6826.

Hoffmann, M.R., Martin, S.T., Choi, W. & Bahnemann, D.W. 1995. Environmental applications of semiconductor photocatalysis. *Chemical Reviews*, 95(1): 69–96.

Huang, T., Lin, X., Xing, J., Wang, W., Shan, Z. & Huang, F. 2007. Photocatalytic activities of hetero-junction semiconductors $WO_3/SrNb_2O_6$. *Materials Science and Engineering: B*, 141(1–2): 49–54.

Joshi, M.M., Labhsetwar, N.K., Mangrulkar, P.A., Tijare, S.N., Kamble, S.P. & Rayalu, S.S. 2009. Visible light induced photoreduction of methyl orange by N-doped mesoporous titania. *Applied Catalysis A: General*, 357(1): 26–33.

Kaixi, S., Jiahong, Z., Jianchun, B. & Yuying, F. 2008. Photocatalytic activity of (copper, nitrogen)-codoped titanium dioxide nanoparticles. *The American Ceram Society*, 91(4): 1369–1371.

Khairy, M. & Zakaria, W. 2014. Effect of metal-doping of TiO_2 nanoparticles on their photocatalytic activities toward removal of organic dyes. *Egyptian Journal of Petroleum*, (0): 419–426.

Lazar, M.A., Varghese, S. & Nair, S.S. 2012. Photocatalytic water treatment by titanium dioxide: recent updates. *Catalysts*, 2(4): 572–601.

Lee, S.Y. & Park, S.J. 2013. TiO_2 photocatalyst for water treatment applications. *Journal of Industrial and Engineering Chemistry*, 19(6): 1761–1769.

Li, H. & Feng, B. 2016. Visible-light-driven composite La_2O_3/TiO_2 nanotube arrays: synthesis and improved photocatalytic activity. *Materials Science in Semiconductor Processing*, 43: 55–59.

Li, J., Sun, F., Gu, K., Wu, T., Zhai, W., Li, W. & Huang, S. 2011. Preparation of spindly CuO micro-particles for photodegradation of dye pollutants under a halogen tungsten lamp. *Applied Catalysis A: General*, 406(1-2): 51–58

Li, J., Xu, J., Dai, W.L., Li, H. & Fan, K. 2009. Direct hydro-alcohol thermal synthesis of special core–shell structured Fe-doped titania microspheres with extended visible light response and enhanced photoactivity. *Applied Catalysis B: Environmental*, 85(3–4): 162–170.

Li, X., Zhao, W. & Zhao, J. 2002. Visible light-sensitized semiconductor photocatalytic degradation of 2, 4-dichlorophenol. *Science in China Series B: Chemistry*, 45(4): 421–425.

Linsebigler, A.L., Lu, G. & Yates, Jr, J.T. 1995. Photocatalysis on TiO_2 surfaces: principles, mechanisms, and selected results. *Chemical Reviews*, 95(3): 735–758.

Liu, C., Wang, L., Tang, Y., Luo, S., Liu, Y., Zhang, S., Zeng, Y. & Xu, Y. 2015. Vertical single or few-layer MoS_2 nanosheets rooting into TiO_2 nanofibers for highly efficient photocatalytic hydrogen evolution. *Applied Catalysis B: Environmental*, 164: 1–9.

Liu, S., Zhu, J., Guo, X., Ge, J. & Wu, H. 2015. Preparation of α-Fe_2O_3–TiO_2/fly ash cenospheres photocatalyst and its mechanism of photocatalytic degradation. *Colloids and Surfaces A: Physicochemical and Engineering Aspects*, 484: 434–440.

Li, W.X. 2013. Photocatalysis of oxide semiconductors. *Journal of the Australian Ceramic Society Volume*, 49(2): 41–46.

Li, X., Lin, H., Chen, X., Niu, H., Liu, J., Zhang, T. & Qu, F. 2016. Dendritic α-Fe_2O_3/TiO_2 nanocomposites with improved visible light photocatalytic activity. *Phys. Chem. Chem. Phys.*, 18(13): 9176–9185.

Li, X., Zhao, W. & Zhao, J. 2002. Visible light-sensitized semiconductor photocatalytic degradation of 2, 4-dichlorophenol. *Science in China Series B: Chemistry*, 45(4): 421–425.

Lou, Z., Li, F., Deng, J., Wang, L. & Zhang, T. 2013. Branch-like hierarchical heterostructure (α-Fe_2O_3/TiO_2): A novel sensing material for trimethylamine gas sensor. *ACS Applied Materials & Interfaces,* 5(23): 12310–12316.

Low, W. & Boonamnuayvitaya, V. 2013. Enhancing the photocatalytic activity of TiO_2 co-doping of graphene–Fe^{3+} ions for formaldehyde removal. *Journal of Environmental Management*, 127: 142–149.

Mahadik, M.A., Shinde, S.S., Pathan, H.M., Rajpure, K.Y. & Bhosale, C.H. 2014. Oxidative degradation of industrial wastewater using spray deposited TiO_2/Au: Fe_2O_3 bilayered thin films. *Journal of Photochemistry and Photobiology B: Biology*, 141: 315–324.

Mahmoodi, N.M., Arami, M., Limaee, N.Y. & Tabrizi, N.S. 2006. Kinetics of heterogeneous photocatalytic degradation of reactive dyes in an immobilized TiO_2 photocatalytic reactor. *Journal of Colloid and Interface Science*, 295(1): 159–164.

Radovic, M.D., Mitrović, J.Z., Bojić, D.V., Antonijević, M.D., Kostić, M.M., Baošić, R.M., & Bojić, A.L. 2014. Effects of system parameters and inorganic salts on the photodecolourisation of textile dye Reactive Blue 19 by UV/H_2O_2 process.

Musić, S., Krehula, S. & Popović, S. 2004. Effect of HCl additions on forced hydrolysis of $FeCl_3$ solutions. *Materials Letters*, 58(21): 2640–2645.

Ohtani, B. 2010. Photocatalysis A to Z—What we know and what we do not know in a scientific sense. *Journal of Photochemistry and Photobiology C: Photochemistry Reviews*, 11(4): 157–178.

Ortega-Liebana, M.C., Hueso, J.L., Larrea, A., Sebastian, V. & Santamaria, J. 2015. Feroxyhyte nanoflakes coupled to up-converting carbon nanodots: a highly active, magnetically recoverable, Fenton-like photocatalyst in the visible-NIR range. *Chem. Commun.*, 51(93): 16625–16628

Pal, B., Sharon, M. & Nogami, G. 1999. Preparation and characterization of TiO_2/Fe_2O_3 binary mixed oxides and its photocatalytic properties. *Materials Chemistry and Physics*, 59(3): 254–261.

Pekakis, P.A., Xekoukoulotakis, N.P. & Mantzavinos, D. 2006. Treatment of textile dyehouse wastewater by TiO_2 photocatalysis. *Water Research*, 40(6): 1276–1286.

Pouran, R., Raman, A.A.A. & Daud, W.M.A.W. 2014. Review on the application of modified iron oxides as heterogeneous catalysts in Fenton reactions. *Journal of Cleaner Production*, 64: 24–35.

Prieto, O., Fermoso, J., Nuñez, Y., Del Valle, J.L. & Irusta, R. 2005. Decolouration of textile dyes in wastewaters by photocatalysis with TiO_2. *Solar Energy*, 79(4): 376–383.

Qu, X., Alvarez, P.J.J. & Li, Q. 2013. Applications of nanotechnology in water and wastewater treatment. *Water Research*, 47(12): 3931–3946.

Radović, M.D. Mitrović, J.Z., Bojić, D.V., Antonijević, M.D., Kostić, M.M. Baošić, R.M. &. Bojić, A.L. 2014. Effects of system parameters and inorganic salts on the photodecolourisation of textile dye Reactive Blue 19 by UV/H_2O_2 process. *Water SA*, 40(3): 571–577.

Ramimoghadam, D., Bagheri, S. & Hamid, S.B.A. 2014. Progress in electrochemical synthesis of magnetic iron oxide nanoparticles. *Journal of Magnetism and Magnetic Materials*, 368: 207–229.

Rawal, S.B., Bera, S., Lee, D., Jang, D.J. & Lee, W.I. 2013. Design of visible-light photocatalysts by coupling of narrow bandgap semiconductors and TiO_2: effect of their relative energy band positions on the photocatalytic efficiency. *Catalysis Science & Technology*, 3(7): 1822–1830.

Rawal, S.B., Chakraborty, A.K. & Lee, W.I. 2009. Heterojunction of FeOOH and TiO_2 for the formation of visible light photocatalyst. *Bulletin of the Korean Chemical Society*, 30(11): 2613–2616.

Rawal, S.B., Sung, S.D. & Lee, W.I. 2012. Novel Ag_3PO_4/TiO_2 composites for efficient decomposition of gaseous 2-propanol under visible-light irradiation. *Catalysis Communications*, 17: 131–135.

Ribeiro, A.R., Nunes, O.C., Pereira, M.F.R. & Silva, A.M.T. 2015. An overview on the advanced oxidation processes applied for the treatment of water pollutants defined in the recently launched Directive 2013/39/EU. *Environment International*, 75: 33–51.

Saien, J., Asgari, M., Soleymani, A.R. & Taghavinia, N. 2009. Photocatalytic decomposition of direct red 16 and kinetics analysis in a conic body packed bed reactor with nanostructure titania coated Raschig rings. *Chemical Engineering Journal*, 151(1–3): 295–301.

Schäffer, J. 2012. Immobilization of TiO_2 via different routes for photocatalytic reactions in a PDMS based microreactor. Unpublished BSc thesis, University of Twente, Enschede, the Netherlands.

Schneider, J., Matsuoka, M., Takeuchi, M., Zhang, J., Horiuchi, Y., Anpo, M. & Bahnemann, D.W. 2014. Understanding TiO_2 photocatalysis: mechanisms and materials. *Chemical Reviews*, 114(19): 9919–9986.

Shao, H.F., Qian, X.F., Yin, J. & Zhu, Z.-K. 2005. Controlled morphology synthesis of β-FeOOH and the phase transition to Fe_2O_3. *Journal of Solid State Chemistry*, 178(10): 3130–3136.

Sharma, S., Ruparelia, J.P. & Patel, M.L. 2011. A general review on advanced oxidation processes for wastewater treatment. Paper presented at the International Conference on Current Trends In Technology, Nuicone – 2011, Ahmedabad, Gujarat, 8–10 December. http://nuicone.org/site/common/proceedings/Chemical/poster/CH_33.pdf [25 May 2015].

Shi, X.F., Li, N., Zhao, K., Cui, G.W., Zhao, Y.Q., Ma, M.Y., Xu, K.H., Li, P., Dong, Y.B. & Tang, B. 2013. A dye-sensitized FeOOH–CNT photocatalyst with three electron transfer channels regulated by hydrogen bonding. *Applied Catalysis B: Environmental*, 136–137: 334–340.

Shifu, C., Xiaoling, Y. & Wei, L. 2009. Preparation and Photocatalytic activity evaluation of composite photocatalyst Fe-TiO_2/TiO_2. *ECS Transactions*, 21(1): 3–22.

Singh, S., Mahalingam, H. & Singh, P.K. 2013. Polymer-supported titanium dioxide photocatalysts for environmental remediation: a review. *Applied Catalysis A: General*, 462–463: 178–195.

Song, J., Wang, X., Bu, Y., Wang, X., Zhang, J., Huang, J., Ma, R. & Zhao, J. 2016. Photocatalytic enhancement of floating photocatalyst: Layer-by-layer hybrid carbonized chitosan and Fe-N- codoped TiO_2 on fly ash cenospheres. *Applied SurfaceScience*. http://www.sciencedirect.com/science/article/pii/S0169433216307619 [In press - corrected proof].

Song, K. Zhou, J., Bao, J. & Feng, Y. 2008. Photocatalytic activity of (copper, nitrogen)-codoped titanium dioxide nanoparticles. *The American Ceramics Society*, 91(4): 1369–1371.

Song, K.Y., Park, M.K., Kwon, Y.T., Lee, H.W., Chung, W.J. & Lee, W.I. 2001. Preparation of transparent particulate MoO_3 /TiO_2 and WO_3 /TiO_2 films and their photocatalytic properties. *Chemistry of Materials*, 13(7): 2349–2355.

Sood, S., Umar, A., Mehta, S.K. & Kansal, S.K. 2015. Highly effective Fe-doped TiO_2 nanoparticles photocatalysts for visible-light driven photocatalytic degradation of toxic organic compounds. *Journal of Colloid and Interface Science*, 450: 213–223.

Strauss, M., Pastorello, M., Sigoli, F.A., De Souza e Silva, J.M. & Mazali, I.O. 2014. Singular effect of crystallite size on the charge carrier generation and photocatalytic activity of nano-TiO_2. *Applied Surface Science*, 319: 151–157.

Su, E.C., Huang, B.S. & Wey, M.Y. 2016. Enhanced optical and electronic properties of a solar light-responsive photocatalyst for efficient hydrogen evolution by $SrTiO_3$/TiO_2 nanotube combination. *Solar Energy*, 134: 52–63.

Tang, J. & Ye, J. 2005. Photocatalytic and photophysical properties of visible-light-driven photocatalyst $ZnBi_{12}O_{20}$. *Chemical Physics Letters*, 410(1–3): 104–107.

Tan, L.L., Ong, W.J., Chai, S.P. & Mohamed, A.R. 2015. Noble metal modified reduced graphene oxide/TiO_2 ternary nanostructures for efficient visible-light-driven photoreduction of carbon dioxide into methane. *Applied Catalysis B: Environmental*, 166–167: 251–259.

Tong, T., Zhang, J., Tian, B., Chen, F. & He, D. 2008. Preparation of Fe^{3+}-doped TiO_2 catalysts by controlled hydrolysis of titanium alkoxide and study on their photocatalytic activity for methyl orange degradation. *Journal of Hazardous Materials*, 155(3): 572–579.

Uzunova-Bujnova, M., Todorovska, R., Dimitrov, D. & Todorovsky, D. 2008. Lanthanide-doped titanium dioxide layers as photocatalysts. *Applied Surface Science*, 254(22): 7296–7302.

Wang, D., Li, Y., Li Puma, G., Wang, C., Wang, P., Zhang, W. & Wang, Q. 2015a. Dye-sensitized photoelectrochemical cell on plasmonic Ag/AgCl @ chiral TiO_2 nanofibers for treatment of urban wastewater effluents, with simultaneous production of hydrogen and electricity. *Applied Catalysis B: Environmental*, 168–169: 25–32.

Wang, D., Li, Y., Li Puma, G., Wang, C., Wang, P., Zhang, W. & Wang, Q. 2015b. Mechanism and experimental study on the photocatalytic performance of Ag/AgCl @ chiral TiO_2 nanofibers photocatalyst: the impact of wastewater components. *Journal of Hazardous Materials*, 285: 277–284.

Wang, J., Zhao, G., Zhang, Z., Zhang, X., Zhang, G., Ma, T., Jiang, Y., Zhang, P. & Li, Y. 2007. Investigation on degradation of azo fuchsine using visible light in the presence of heat-treated anatase TiO_2 powder. *Dyes and Pigments*, 75(2): 335–343.

Wang, S. & Zhou, S. 2011. Photodegradation of methyl orange by photocatalyst of CNTs/P-TiO_2 under UV and visible-light irradiation. *Journal of Hazardous Materials*, 185(1): 77–85.

Wang, X., Wang, K., Feng, K., Chen, F., Yu, H. & Yu, J. 2014. Greatly enhanced photocatalytic activity of $TiO_{2-x}N_x$ by a simple surface modification of Fe(III) cocatalyst. *Journal of Molecular Catalysis A: Chemical*, 391: 92–98.

Wei, C. & Nan, Z. 2011. Effects of experimental conditions on one-dimensional single-crystal nanostructure of β-FeOOH. *Materials Chemistry and Physics*, 127(1–2): 220–226.

Xiang, Q., Yu, J. & Wong, P.K. 2011. Quantitative characterization of hydroxyl radicals produced by various photocatalysts. *Journal of Colloid and Interface Science*, 357(1): 163–167.

Xiao, G., Zhang, X., Zhang, W., Zhang, S., Su, H. & Tan, T. 2015. Visible-light-mediated synergistic photocatalytic antimicrobial effects and mechanism of Ag-nanoparticles@chitosan–TiO_2 organic–inorganic composites for water disinfection. *Applied Catalysis B: Environmental*, 170–171: 255–262.

Xia, Y. & Yin, L. 2013. Core–shell structured α-Fe_2O_3@TiO_2 nanocomposites with improved photocatalytic activity in the visible light region. *Physical Chemistry Chemical Physics*, 15(42): 18627.

Xu, Y. & Schoonen, M.A.A. 2000. The absolute energy positions of conduction and valence bands of selected semiconducting minerals. *American Mineralogist*, 85(3–4): 543–556.

Xu, Z., Liang, J. & Zhou, L. 2013. Photo-Fenton-like degradation of azo dye methyl orange using synthetic ammonium and hydronium jarosite. *Journal of Alloys and Compounds*, 546: 112–118.

Xu, Z., Zhang, M., Wu, J., Liang J., Zhou, L. & Lu, B. 2013. Visible light degradation of azo dye methyl orange using TiO_2/β-FeOOH as heterogeneous photo-Fenton-like catalyst. *Water Science & Technology*, 68(10): 2178–2185.

Yu, L., Wei, C., Yan, Q. & Xu, Z.J. 2015. Controlled synthesis of high-performance β-FeOOH anodes for lithium-ion batteries and their size effects. *Nano Energy*, 13: 397–404.

Zaleska, A. 2008. Doped-TiO_2: a review. *Recent Patents on Engineering*, 2(3): 157–164.

Zhang, M., Xu, Z., Liang, J., Zhou, L. & Zhang, C. 2015. Potential application of novel TiO_2/β-FeOOH composites for photocatalytic reduction of Cr(VI) with an analysis of statistical approach. *International Journal of Environmental Science and Technology*, 12(5): 1669–1676.

Zhang, X., Xie, Y., Chen, H., Guo, J., Meng, A. & Li, C. 2014. One-dimensional mesoporous Fe_2O_3@TiO_2 core–shell nanocomposites: rational design, synthesis and application as high-performance photocatalyst in visible and UV light region. *Applied Surface Science*, 317: 43–48.

Zhang, Y., Cheng, K., Lv, F., Huang, H., Fei, B., He, Y., Ye, Z. & Shen, B. 2014. Photocatalytic treatment of 2,4,6-trinitotoluene in red water by multi-doped TiO_2 with enhanced visible light photocatalytic activity. *Colloids and Surfaces A: Physicochemical and Engineering Aspects*, 452: 103–108.

APPENDICES

Appendix A.

Table A.1: The measured absorbances for different MO concentrations correlated to make a calibration curve

Concentration (mg/L)	Absorption (Abs)
0	0
1	0.042
2.5	0.072
5	0.28
10	0.744
20	1.267
30	2.083
40	2.823

Table A.2: Experimental conditions for photocatalytic performance of 5%β-FeOOH/TiO_2 compared to TiO_2 (Anatase), P25, Peroxide and β-FeOOH photocatalysts

Photocatalyst	MO (mg)	Catalyst (g)	Peroxide(mL)	Light(W)	pH
Blank	80	0	0	300	4.5
Simulated solar light	80	0	3	300	4.5
β-FeOOH	80	0,01	3	300	4.5
TiO_2 (Anatase)	80	0,01	3	300	4.5
Peroxide	80	0	3	300	4.5
Degusa P25	80	0,01	3	300	4.5
10% β-FeOOH/TiO_2	80	0,01	3	300	4.5
2% β-FeOOH/TiO_2	80	0,01	3	300	4.5
5% β-FeOOH/TiO_2	80	0,01	3	300	4.5

Table A.3: Raw data and real concentration calculation for photocatalytic performance of 5%β-FeOOH/TiO_2 compared to TiO_2 (Anatase), P25, Peroxide and β-FeOOH photocatalysts

Method	Time(min)	Conc (mg/L)	C_t/C_0	ln C_t/C_0	μ
1. Blank	0	80	1	0	0
	30	80	1	0	0
	60	80	1	0	0
2. Simulated solar light	0	73,87245	1	0	0
	30	72,88028	0,986569	0,013522	1,343089
	60	72,21862	0,977612	0,022642	2,238776
3. TiO_2 (Anatase)	0	86,6923	1	0	0
	30	67,4242	0,777742	0,251361	22,22585
	60	48,8671	0,563684	0,573261	43,63156
4. 10% β-FeOOH/TiO_2	0	74,631	1	0	0
	30	41,95	0,562099	0,576078	43,79011
	60	17,0143	0,227979	1,478502	77,2021
5. 5% β-FeOOH/TiO_2	0	63,5137	1	0	0
	30	22,7023	0,357439	1,028789	64,25606
	60	1,9411	0,030562	3,488001	96,94381
6. 2% β-FeOOH/TiO_2	0	72,4012	1	0	0
	30	32,8696	0,453992	0,789675	54,60075
	60	10,7575	0,148582	1,90662	85,14182
7. Peroxide	0	75,5296	1	0	0
	30	60,883	0,806081	0,215571	19,39187
	60	52,2799	0,692178	0,367913	30,78224
8. β-FeOOH	0	75,1741	1	0	0
	30	73,04821	0,97172	0,028687	0,02828
	60	69,68518	0,926984	0,075819	0,073016
9. TiO_2 P25	0	94.0987	1	0	0
	15	82.3454	0,87234	0,136576	12,76596
	30	75.3546	0,797872	0,225807	20,21277
	45	62.7642	0,659574	0,41616	34,04255
	60	58.1462	0,617021	0,482852	38,29787

Table A.4: Raw data and real concentration calculation for the effect of the hydrogen peroxide load on the degradation of MO without photocatalyst performance of 5%β-FeOOH/TiO_2

5mL (of 30% H_2O_2)/L				
Time (min)	**Concentration (mg/L)**	**C_t/C_o**	**ln (C_t/C_o)**	**μ**
0	79.8667	1	0	0
15	68	0.851419	0.160851	14.85813
30	59.8165	0.748954	0.289077	25.10458
45	53	0.663606	0.410067	33.63943
60	47.3029	0.592273	0.523787	40.77269
90	39.7	0.497078	0.699008	50.29217
0 mL (of 30% H_2O_2)/L				
Time	**Concentration (mg/L)**	**C_t/C_o**	**ln (C_t/C_o)**	**μ**
0	80	1	0	0
15	79	0.9875	0.012579	1.25
30	80	1	0	0
45	79	0.9875	0.012579	1.25
60	79	0.9875	0.012579	1.25
90	80	1	0	0
3 mL (of 30% H_2O_2)/L				
Time	**Concentration (mg/L)**	**C_t/C_o**	**ln (C_t/C_o)**	**μ**
0	80	1	0	0
15	70	0.875	0.133531	12.5
30	61	0.7625	0.271153	23.75
45	55	0.6875	0.374693	31.25
60	52	0.65	0.430783	35
90	43	0.5375	0.620827	46.25
1 mL (of 30% H_2O_2)/L MO				
Time	**Concentration (mg/L)**	**C_t/C_o**	**ln (C_t/C_o)**	**μ**
0	80	1	0	0
15	78	0.975	0.025318	2.5
30	75.103	0.938788	0.063166	6.12125
45	73	0.9125	0.091567	8.75
60	70	0.875	0.133531	12.5
90	66.64	0.833	0.182722	16.7
0.5 mL (of 30% H_2O_2)/L MO				
Time	**Concentration (mg/L)**	**C_t/C_o**	**ln (C_t/C_o)**	**μ**
0	80	1	0	0
15	78	0.975	0.025318	2.5
30	78	0.975	0.025318	2.5

45	77	0.9625	0.038221	3.75
60	77	0.9625	0.038221	3.75
90	76	0.95	0.051293	5

Table A.5: Raw data and real concentration calculation for the effect of the hydrogen peroxide load on the degradation of MO with 5%β-FeOOH/TiO_2 photocatalyst

0 mL Peroxide + 5% beta-FeOOH + Light				
Time	**Concentration (mg /L)**	**C_t/C_o**	**ln(C_t/C_o)**	**μ**
0	80	1	0	0
15	78	0.975	0.025318	2.5
30	75	0.9375	0.064539	6.25
45	72	0.9	0.105361	10
60	70	0.875	0.133531	12.5
90	65	0.8125	0.207639	18.75
0.5 mL Peroxide + 5% beta-FeOOH + Light				
Time	**Concentration (mg/L)**	**C_t/C_o**	**ln(C_t/C_o)**	**μ**
0	80	1	0	0
15	70	0.875	0.133531	12.5
30	59	0.7375	0.304489	26.25
45	45	0.5625	0.575364	43.75
60	35	0.4375	0.826679	56.25
90	10	0.125	2.079442	87.5
1 mL Peroxide + 5% beta-FeOOH + Light				
Time	**Concentration (mg/L)**	**C_t/C_o**	**ln(C_t/C_o)**	**μ**
0	74.26402	1	0	0
15	61.45	0.827453	0.189403	17.25468
30	51	0.686739	0.375801	31.3261
45	40	0.538619	0.618747	46.13812
60	30	0.403964	0.906429	59.60359
90	8	0.107724	2.228185	89.22762
3 mL Peroxide + 5% beta-FeOOH + Light				
Time	**Concentration**	**C_t/C_o**	**μ**	**ln C_t/C_o**
0	68	1	0	0
15	50	0.735294	26.47059	0.307485
30	36	0.529412	47.05882	0.635989
45	20	0.294118	70.58824	1.223775
60	1	0.014706	98.52941	4.219508
5 mL Peroxide + 5% beta-FeOOH + Light				
Time	**(mg/L)**	**C_t/C_o**	**ln (C_t/C_o)**	**μ**
0	75	1	0	0
15	47	0.626667	0.467341	37.33333

30	32	0.426667	0.851752	57.33333
45	14.35	0.191333	1.653738	80.86667
60	0.7	0.009333	4.674163	99.06667

Table A.6: Contribution of H_2O_2 on the degradation of MO

Peroxide + Catalyst				**Peroxide + Light**			
Volume peroxide (mL)	**K**	**Intercept**	**R^2**	**peroxide (mL)**	**K**	**intercept**	**R^2**
5	0.039	-0.1955	0.96	5	0.0068	0.094	0.99
3	0.03	-0.3022	0.95	3	0.0058	0.091	0.99
1	0.016	-0.0347	0.99	1	0.002	0.0069	0.98
0.5	0.014	-0.104	0.98	0.5	0.0004	0.0123	0.99

Table A.7: Raw data and real concentration calculation for the effect of the initial dye concentration on the photocatalytic performance of 5%β-FeOOH/TiO_2

200 mg/L				
Time	**Concentration**	**C_t/C_0**	**$\ln(C_t/C_0)$**	**μ**
0	190	1	0	0
15	145	0.763158	0.27029	23.68421
30	117	0.615789	0.48485	38.42105
45	97	0.510526	0.672313	48.94737
60	70	0.368421	0.998529	63.15789
75	47	0.247368	1.396876	75.26316
90	23	0.121053	2.11153	87.89474
105	1.78	0.009368	4.670411	99.06316
150 mg/L				
Time	**Concentration**	**C_t/C_0**	**$\ln(C_t/C_0)$**	**μ**
0	141.802	1	0	0
15	103	0.726365	0.319703	27.3635
30	62	0.437229	0.827297	56.27706

45	48.42	0.341462	1.074519	65.85379
60	23	0.162198	1.818937	83.7802
75	8	0.056417	2.87499	94.35833
90	1	0.007052	4.954432	99.29479

80 mg/L				
Time	**Concentration**	**C_t/C_0**	**$\ln(C_t/C_0)$**	**μ**
0	65	1	0	0
15	12.79	0.196769	1.625724	80.32308
30	1.71924	0.02645	3.632505	97.35502
45	0.6	0.009231	4.685213	99.07692

50 mg/L				
Time	**Concentration**	**C_t/C_0**	**$\ln(C_t/C_0)$**	**μ**
0	34	1	0	0
5	18	0.529412	0.635989	47.05882
10	10.40911	0.30615	1.183679	69.38497
15	4.53	0.133235	2.015639	86.67647
20	1.773	0.052147	2.953687	94.78529
30	1	0.029412	3.526361	97.05882
45	1	0.029412	3.526361	97.05882

25 mg/L				
Time	**Concentration**	**C_t/C_0**	**$\ln(C_t/C_0)$**	**μ**
0	25	1	0	0
5	18	0.72	0.328504	28
10	10.40911	0.416364	0.876194	58.36356
15	6.7	0.268	1.316768	73.2
20	3	0.12	2.120264	88

Table A.8: The raw data and real concentration calculation on the effect of light intensity

150 W				
Time	**concentration**	**C_t/C_0**	**ln C_t/C_0**	μ
0	76	1	0	0

15	60	0.789474	0.236389	21.05263
30	43	0.565789	0.569533	43.42105
45	20	0.263158	1.335001	73.68421
250 W				
Time	**concentration**	**C_t/C_0**	**ln C_t/C_0**	**μ**
0	73.81	1	0	0
15	40	0.541932	0.612615	45.8068
30	25	0.338707	1.082618	66.12925
45	5.37	0.072754	2.620666	92.72456
250 W (p25)				
time	**Concentration**	**C_t/C_0**	**ln C_t/C_0**	**μ**
0	94	1	0	0
15	82	0.87234	0.136576	12.76596
30	75	0.797872	0.225807	20.21277
45	62	0.659574	0.41616	34.04255
60	58	0.617021	0.482852	38.29787
90	37	0.393617	0.932377	60.6383
300 W				
Time	**Concentration**	**C_t/C_0**	**ln C_t/C_0**	**μ**
0	65	1	0	0
15	12.79	0.196769	1.625724	80.32308
30	1.71924	0.02645	3.632505	97.35502
45	0.6	0.009231	4.685213	99.07692

Table A.9: The raw data and real concentration calculation on the effect of the pH of the solution

pH 3				
Time	**Concentration**	**C_t/C_0**	**ln(C_t/C_0)**	**μ**
0	27	1	0	0
10	5.75	0.212963	1.546637	78.7037

15	4	0.148148	1.909543	85.18519
25	0.38	0.014074	4.263421	98.59259
30	0.38	0.014074	4.263421	98.59259
pH 4.5				
Time	**Concentration**	**C_t/C_0**	**$\ln(C_t/C_0)$**	**μ**
0	65	1	0	0
10	30	0.461538	0.77319	53.84615
15	12.79	0.196769	1.625724	80.32308
30	1.71924	0.02645	3.632505	97.35502
pH = 7.52				
Time	**Concentration**	**C_t/C_0**	**$\ln (C_t/C_0)$**	**μ**
0	56.73076	1	0	0
10	40	0.705085	0.349437	29.49151
15	36.93652	0.651085	0.429116	34.89155
30	25	0.440678	0.819441	55.9322
45	12.44257	0.219327	1.517193	78.06733
60	1.609718	0.028375	3.562258	97.16253

Table A.10: The raw data and real concentration calculation on the effect of the pH of catalyst load

0.005 g/ 100 mL				
Time	**Concentration**	**C_t/C_0**	**$\ln(C_t/C_0)$**	**μ**
0	74	1	0	0
15	50	0.675676	0.392042	32.43243
30	35	0.472973	0.748717	52.7027
45	15	0.202703	1.596015	79.72973

60	1.22	0.016486	4.105214	
0.01 g/ 100 mL				
Time	**Concentration**	**C_t/C_0**	**$\ln(C_t/C_0)$**	**μ**
0	74	1	0	0
15	45	0.608108	0.497403	39.18919
30	30	0.405405	0.902868	59.45946
45	14.35	0.193919	1.640315	80.60811
60	0.7	0.009459	4.66074	99.05405
0.02 g/ 100 mL				
Time	**Concentration**	**C_t/C_0**	**$\ln(C_t/C_0)$**	**μ**
0	65	1	0	0
15	12.79	0.196769	1.625724	80.32308
30	1.71924	0.02645	3.632505	97.35502
45	0.6	0.009231	4.685213	99.07692

Table A.11: The raw data and real concentration calculation for the degradation of commercial metal-complex dyes

Yellow				
Time[min]	**Conc**	**C_t/C_0**	**$\ln(C_t/C_0)$**	**μ**
0	28.5	1	0	0
5	13	0.45614	0.784955	54.38596
10	8	0.280702	1.270463	71.92982
15	5	0.175439	1.740466	82.45614
20	1	0.035088	3.349904	96.49123
Red				
Time[min]	**Conc**	**C_t/C_0**	**$\ln (C_t/C_0)$**	**μ**
0	80	1	0	0
5	44.5	0.55625	0.586537	44.375
10	23.5	0.29375	1.225026	70.625
15	13.5	0.16875	1.779337	83.125
20	3.4	0.0425	3.158251	95.75
Grey				
Time	**Concentration**	**C_t/C_0**	**$\ln(C_t/C_0)$**	**μ**

0	47	1	0	0
5	34	0.723404	0.323787	27.65957
10	28	0.595745	0.517943	40.42553
15	19	0.404255	0.905709	59.57447
20	8	0.170213	1.770706	82.97872
25	2	0.042553	3.157	95.74468

Table A.12: The raw data and real concentration calculation for the degradation of real wastewater effluent

Yellow						
Time[min]	**C1**	**v1**	**c2**	**C_t/C_0**	**ln C_t/C_0**	**μ**
0	5.5	5	27.5	1	0	0
30	1.3	5	6.5	0.236364	1.442384	76.36364
60	1.5	5	7.5	0.272727	1.299283	72.72727
90	5.6	1	5.6	0.203636	1.591419	79.63636
120	2.6	1	2.6	0.094545	2.358675	90.54545
Red						
Time[min]	**c1**	**v2**	**C2**	**C_t/C_0**	**ln C_t/C_0**	**μ**
0	2.8	5	14	1	0	0
30	0.7	5	3.5	0.25	1.386294	75
60	0.6	5	3	0.214286	1.540445	78.57143
90	2.9	1	2.9	0.207143	1.574347	79.28571
120	1.2	1	1.2	0.085714	2.456736	91.42857
Grey						
Time[min]	**C1**	**v1**	**c2**	**C_t/C_0**	**ln C_t/C_0**	**μ**
0	3.1	5	15.5	1	0	0
30	0.9	5	4.5	0.290323	1.236763	70.96774
60	0.9	5	4.5	0.290323	1.236763	70.96774
90	2.7	1	2.7	0.174194	1.747588	82.58065
120	1.7	1	1.7	0.109677	2.210212	89.03226

Table A.13: The raw data and real concentration calculation on the effect of recycling 5%β-FeOOH/TiO_2 on the degradation of MO

Fist recycle				
Time	**Concentration**	**C_t/C_0**	**$\ln(C_t/C_0)$**	**μ**
0	65.41207	1	0	0
15	12.79096	0.195544	1.631968	80.44557
30	1.71924	0.026283	3.638824	97.37168
45	0.60863	0.009305	4.677252	99.06954
Second recycle				
Time	**Concentration**	**C_t/C_0**	**$\ln(C_t/C_0)$**	**μ**
0	71.94616	1	0	0
15	42.26902	0.587509	0.531864	41.2491
30	12.64165	0.17571	1.738921	82.42901
45	1.09922	0.015278	4.181317	98.47216
Third recycle				
Time	**Concentration**	**C_t/C_0**	**$\ln(C_t/C_0)$**	**μ**
0	76.83073	1	0	0
15	37.96036	0.494078	0.705062	50.59222
30	9.68389	0.126042	2.071141	87.39581
45	1.565636	0.020378	3.893313	97.96223
Fourth recycle				
Time	**Concentration**	**C_t/C_0**	**$\ln(C_t/C_0)$**	**μ**
0	78.658	1	0	0
15	65.33386	0.830607	0.185599	16.93933
30	43.71235	0.555727	0.587479	44.42733
45	24.15274	0.30706	1.180712	69.29398

Appendix B:

Table B.1: The raw data and standard deviation calculation on the validation of 5%β-FeOOH/TiO_2 on the degradation of MO

N=4								
	Concentration (mg/L)				C_t/C_0			
Time	Run 1	Run 2	Run 3	Run 4	RUN 1	RUN 2	RUN 3	RUN 4
0	65.0918	50.9652	50.8106	70.9767	1	1	1	1
15	37.5655	32.7076	32.6856	46.2353	0.6417	0.577116	0.64328	0.65141
30	21.4143	14.4730	18.7709	26.8317	0.2839	0.328986	0.36942	0.37803
45	8.48201	6.38875	6.62311	12.6348	0.1253	0.130308	0.13034	0.17801
60	1.57959	1.25818	2.11903	2.39736	0.0246	0.024267	0.04170	0.03377

μ	xi-μ				Standard deviation calculation			
Average	RUN 1	RUN 2	RUN 3	RUN 4	Σ(xi-μ)^2	(1/N)Σ(xi-μ)^2	sqrt((1/N)Σ(xi-μ)^2)	
1	0	0	0	0	0	0	0	0
0.62839	0.00017	0.00262	0.00022	0.00053	1.27E-05	4.22E-06	0.00205	0.20552
0.34010	0.00315	0.00012	0.00085	0.00143	3.1E-05	1.03E-05	0.00321	0.32170
0.14100	0.00024	0.00011	0.00011	0.00137	3.4E-06	1.13E-06	0.00106	0.10638
0.03110	4.12E-05	4.68E-05	0.00011	7.12E-06	4.3E-08	1.43E-08	0.00012	0.01197

Table B.2: The % standard error calculation for the kinetics of different runs of the degradation of MO

RUN	Reaction rate	Average rate	% standard error
1	0.0602	0.05692	0.018901
2	0.0595	0.05692	0.011694
3	0.053	0.05692	0.026996
4	0.0538	0.05692	0.017102
INITIAL	0.0581	0.05692	0.002446

Table B.3: Experiment details for the degradation of (80 mg/L) Acid Black using (800 mg/L) of 5% β-FeOOH/TiO_2 Catalyst load with H_2O_2 concentration of 50 mL/L at ph 4.5

RUN 1					
Time (min)	**Absorbance (abs)**	**Concentration (mg/L)**	**Ct/Co**	**ln(Ct/Co)**	**μ**
0	1.01	57.19698	1	0	0
15	0.4	22.6173	0.39542822	0.927786	60.4572
30	0.21	11.84658	0.207118977	1.57446188	79.2881
45	0.125	7.0281	0.122875369	2.0965847	87.7125
60	0.087	4.873956	0.08521352	2.46259517	91.4786
RUN 2					
Time (min)	**Absorbance (abs)**	**Concentration (mg/L)**	**Ct/Co**	**ln(Ct/Co)**	μ
0	1.08	61.16514	1	0	0
15	0.185	10.42938	0.170511831	1.7689506	82.9488
30	0.1	5.6109	0.091733625	2.38886628	90.8266
45	0.08	4.47714	0.073197576	2.61459297	92.6802
60	0.052	2.889876	0.047247108	3.05236382	95.2753
RUN 3					
Time (min)	**Absorbance (abs)**	**Concentration (mg/L)**	**Ct/Co**	**ln(Ct/Co)**	μ
0	0.655	37.07274	1	0	0
15	0.23	12.98034	0.35013166	1.04944602	64.9868
30	0.115	6.46122	0.174284933	1.74706377	82.5715
45	0.065	3.62682	0.097829834	2.3245257	90.217
60	0.037	2.039556	0.055014979	2.90014979	94.4985

Table B.4: The kinetics of different runs for the degradation of Acid black wastewater

Kinetics				
Time	**Run 1**	**Run 2**	**Run 3**	**AVERAGE**
0	0.5749	0.1892	0.1935	0.3192
15	1.2694	0.8972	0.8025	0.9897
30	1.9639	1.6052	1.4115	1.6602
45	2.6584	2.3132	2.0205	2.3307
60	3.3529	3.0212	2.6295	3.0012

Table B.5: The % standard error calculation for the kinetics of different runs of the degradation of Acid black wastewater

(X1 - μ)^2	(X2 - μ)^2	(X3 - μ)^2	Σ(xi-μ)^2	(1/N)Σ(xi-μ)^2	sqrt((1/N)Σ(xi-μ)^2)
0	0	0	0	0	0
0.103003472	0.270632	0.039713	0.413349	0.137783	0.371191
0.108242381	0.235615	0.024461	0.368319	0.122773	0.35039
0.061826701	0.072554	0.000429	0.13481	0.044937	0.211982
0.117265901	0.061171	0.009047	0.187483	0.062494	0.249989

Appendix C.

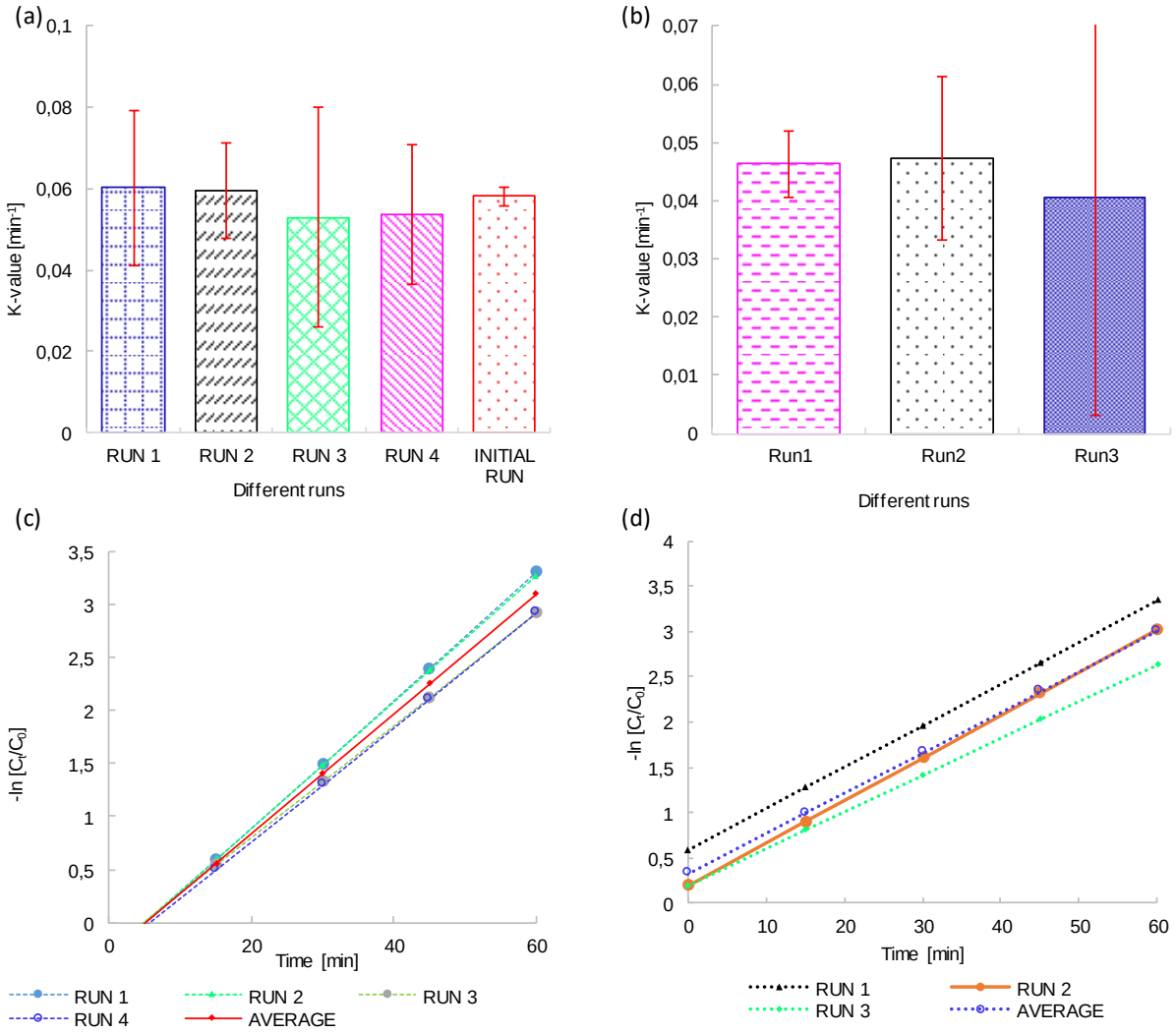

Figure C.1: (a) The % error bars calculated for the kinetics of the repeatability of MO and (b) for the repeatability of Acid black. (c) First order reaction rate for MO and (d) First order reaction rate for Acid black